THE ROLE OF THE CYTOSKELETON IN 3D CANCER CELL MIGRATION

by

Anjil Giri

A dissertation submitted to the Johns Hopkins University in conformity with the requirements for the degree of Doctor of Philosophy of Chemical and Biomolecular Engineering

Baltimore, Maryland

March 2014

ABSTRACT

Arp2/3 is a protein complex that nucleates actin filament assembly in the lamellipodium in adherent cells crawling on planar two-dimensional (2D) substrates. However, in patho-physiological situations, cell migration typically occurs within a three-dimensional (3D) environment and little is known about the role of Arp2/3 and associated proteins in 3D cell migration. Using time resolved live-cell imaging and a fibrosarcoma cell line, HT1080, commonly used to study cell migration, we find that the Arp2/3 complex and associated proteins N-WASP, WAVE1, Cortactin, and Cdc42 regulate 3D cell migration. This regulation is caused by formation of multi-generation dendritic protrusions, which mediate traction forces on the surrounding matrix and effective cell migration. The primary protrusions emanating directly from the cell body and prolonging the nucleus form independent of Arp2/3 and dependent on focal adhesion proteins FAK, talin, and p130Cas. The Arp2/3 complex, N-WASP, WAVE1, Cortactin, and Cdc42 regulate the secondary protrusions branching off from the primary protrusions. In 3D matrices, fibrosarcoma cells as well as migrating breast, pancreatic, and prostate cancer cells do not display lamellipodial structures. This study characterizes the unique topology of protrusions made by cells in a 3D matrix and show that these dendritic protrusions play a critical role in 3D cell motility and matrix deformation. The relative contribution of these proteins to 3D migration is significantly different from their role in 2D migration.

Microtubules have long been targeted to control tumor growth and, more recently, metastatic disease, for which a critical step is the local invasion of tumor cells into the 3D collagen-rich stromal matrix. To migrate in collagen matrices human fibrosarcoma and breast cancer cells exploit the dynamic formation of highly branched protrusions, which are

composed of a microtubule-filled core surrounded by actin filaments that is largely absent in the same cells flattened on 2D substrates. Microtubule plus-end tracking protein EB1 and microtubule-associated motor protein dynein critically modulate 3D cell migration, not by regulating vesicular trafficking, but by regulating both speed and persistence through regulation of protrusion branching itself regulated by differential assembly dynamics of microtubules in the protrusions. These proteins do not regulate conventional 2D migration. An important consequence of the prominent role of microtubules in 3D migration is that the treatment of fibrosarcomas by commonly used cancer drug paclitaxel, which stabilizes microtubules, is dramatically more effective in 3D than in 2D, uniformly and completely blocking 3D cell migration. This work reveals the central role that microtubule dynamics plays in cell migration in more pathologically relevant 3D collagen matrices and suggests that cancer drugs targeting microtubule dynamics to mitigate migration should be further tested in 3D microenvironments.

Cell migration through three-dimensional (3D) extra-cellular matrices is critical to the normal development of tissues and organs and in disease processes, yet adequate analytical tools to characterize 3D migration are lacking. We quantified the migration patterns of individual fibrosarcoma cells on 2D substrates and in 3D collagen matrices and found that 3D migration does not follow a random walk. Both 2D and 3D migration feature a non-Gaussian, exponential mean cell velocity distribution, which we show is primarily a result of cell-to-cell variations. Unlike in the 2D case, 3D cell migration is anisotropic: velocity profiles display different speed and self-correlation processes in different directions, rendering the classical persistent random walk (PRW) model of cell migration inadequate. By incorporating cell heterogeneity and local anisotropy to the PRW model, 3D cell motility is predicted over a wide range of matrix densities, which identifies density-independent

emerging migratory properties. This analysis also reveals the unexpected robust relation between cell speed and persistence of migration over a wide range of matrix densities.

Advisor: Dr. Denis Wirtz

Readers: Dr. Marc Ostermeier, Dr. Sharon Gerecht, Dr. Sean X. Sun, Dr. Moumita Das, Dr. Kalina Hristova, and Dr. Zachary Gagnon

ACKNOWLEDGMENTS

There are many people I have been fortunate enough to learn from during my Ph.D. and I would like to take this opportunity to express my sincere gratitude to them.

First, I should thank my advisor Dr. Denis Wirtz. I first met Denis as a first year Ph.D. student at Hopkins. After hearing him explain what his lab does during our first meeting, it didn't take me long to know his passion towards his research and science in general. I made up my mind that very moment that Denis is the kind of person I would be happy working with. After all, it is a lot more fun working with a person who really cares about what he does. After I joined the lab, I was challenged to come up with new ideas, focus on why and how the experiment we do adds to our understanding of cell biology and disease and not just how to do the experiments. Our numerous discussions on my research helped me dig deeper into our findings. I would also like to thank Denis for providing a lab environment conducive to learning and for the financial freedom he provided to test out new devices, reagents etc., which I often didn't think about as much but were critical to the success of many experiments.

Next, I would like to thank Dr. Saumendra Bajpai, who was my first mentor in the Wirtz lab. I initially asked him countless questions on how to operate lab instruments and he was (almost ☺) always ready to help. We also had numerous discussions on research ideas, which were important in designing initial but crucial experiments.

I am grateful to my GBO and thesis committee, which consisted of Dr. Marc Ostermeier, Dr. Sharon Gerecht, Dr. Sean X. Sun, and Dr. Moumita Das for providing me important suggestions regarding my thesis. I also thank Dr. Konstantinos Konstantopoulos and Dr. Gregory D. Longmore for providing me with ample guidance on my research

projects, particularly on the work related to the cell cytoskeleton. My sincere respect also goes to my undergraduate research advisors, Dr. Kurt Gustin and Dr. Rodney Hill, who introduced me to cell and molecular biology and this was the foundation I built on during my graduate studies.

I am thankful to all members of the Wirtz lab. In particular, I would like to thank Dr. Wei Chiang Chen, Allison Chambliss, Angela Jimenez, and double Dr. Zev Binder, who were also my classmates. They were always available whenever I needed help and I have enjoyed the time in and outside the lab with them. Next, a million thanks to the three undergraduates who worked with me: Nick Trenton, Hasini Jayatilaka, and Alexa Oxer. They spent many hours growing cells, experimenting with them, and analyzing data (and many more hours on failed experiments). I will be forever thankful for their help in my research projects. Dr. Shyam Khatau, Dr. Christopher Hale, Dr. Terrence Dobrowsky, Dr. Matt Keuss, and Dr. Stephanie Fraley were excellent resources to learn science from and I can't thank them enough for the training they have provided me. I would like to thank Dr. Dong-Hwee Kim, who has been a good friend and has also provided me with suggestions regarding lab work and life in general. Many thanks go to Jude Phillip, Ivie Aifuwa, Jake Sarnecki, Angela San, and Sarita Koride for being great friends and also for helping with things in the lab. I have genuinely enjoyed being around them. I would also like to thank Jenna Graham, Tânia Perestrelo, and Leonor Guedes da Silva. I am very much indebted to our postdocs Dr. Meng Horng Lee, Dr. Pei-Hsun Wu, Dr. Lijuan He, Dr. Yu-Tai Chang, Dr. Lijuan Hale, and Dr. Daniele Gilkes who have provided critical comments and suggestions about my work. I am particularly thankful to Dr. Wu who I worked with on the 3D cell migration model and Dr. Gilkes who trained me on lentiviral transductions during my first year. I shouldn't forget to thank the many undergraduates who work in the Wirtz

lab; they keep the lab breathing. They are also an intelligent bunch of people to work with. It has been a great learning experience working with friends from around Hopkins, who include Shivendra Pandey, Clay Wright, Osman Yogurtcu, Wei-Chien Hung, Christian Pick, as well as other colleagues in the ChemBE department.

Life outside of graduate school would not be fun without friends I met on a regular basis. I would like to thank Ravi, Safal, Aurora, Anish, and all my friends in the Baltimore-D.C. area for all the good times we shared together.

Most important of all, I would like to thank my family and my girlfriend, Anu for all the understanding and support I have received. I am indebted to my parents who let me travel so far away from home and pursue what I wanted without questioning my choices. My sisters kept me up to date with the things going on back home and were never tired of asking me how my work is going and helped me cheer up when things were not optimal. I do not have enough words to that my girlfriend, Anu for her untiring support. She has been my best friend, always found time to listen to me and importantly been very understanding. Thank you for everything.

To Mom, Dad, Alina, Alisha, and Anu

TABLE OF CONTENTS

LIST OF FIGURES

LIST OF TABLES

CHAPTER 1

Introduction

Cancer is a collection of diseases in which the cell proliferation checkpoints are disrupted and cells divide uncontrollably to form a mass called tumor, which often has highly invasive properties. There are more than 200 different cancers identified to date and the complexity because of the vast numbers of genetic mutations, heterogeneity of cell type, and epigenetic factors involved have rendered cancer a difficult problem to tackle. Irrespective of the cancer type, all cancers are now generally believed to have acquired ten characteristics: sustaining proliferative signaling, evading growth suppressors, avoiding immune destruction, enabling replicative immortality, tumor-promoting inflammation, activating invasion and metastasis, inducing angiogenesis, genomic instability and mutation, resisting cell death, and deregulating cellular energetics (Hanahan and Weinberg 2011, 2000). Cancer is the second leading cause of deaths in the United States after heart disease (Centers for Disease Control and Prevention 2010) and metastasis is responsible for about 90% of cancer-related deaths (Chaffer and Weinberg 2011). Cancer metastasis is a complex process, in which cancerous cells first establish a tumor, invade the surrounding tissue and enter the vasculature, get transported via blood to distant sites, extravasate from the vasculature, and establish a new tumor at the secondary site (Chaffer and Weinberg 2011, Wirtz, Konstantopoulos, and Searson 2011b).

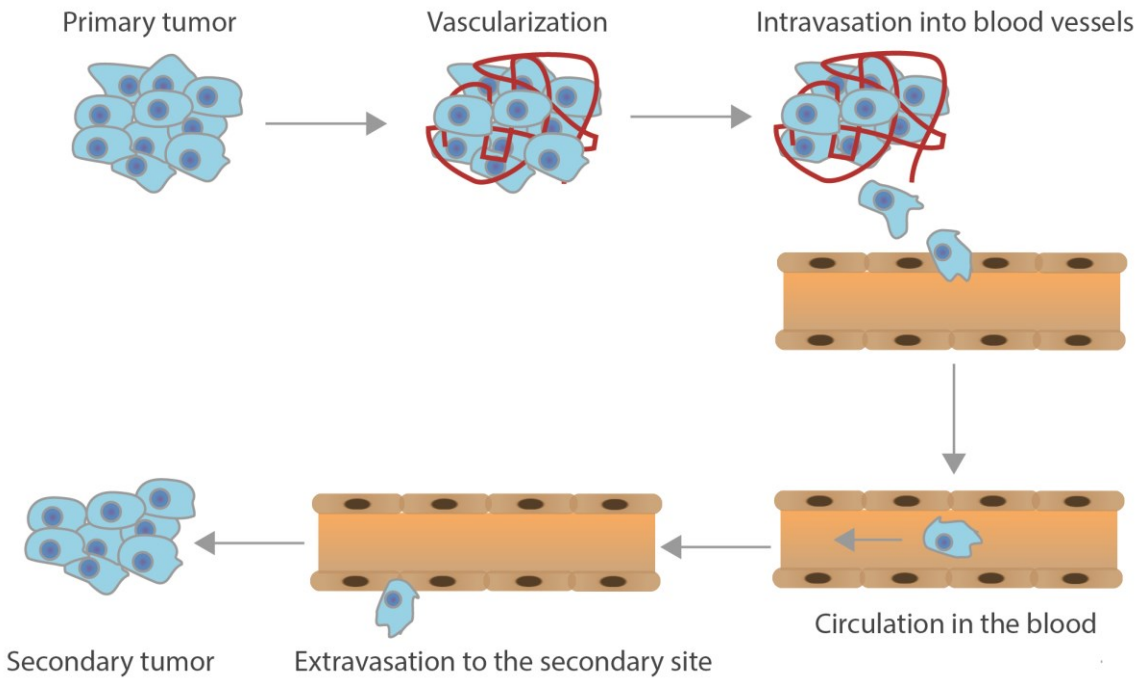

Figure 1-1. The cancer metastasis process

Vascularization of the tumor provides nutrients for the rapidly growing cancer cells. Cells break loose from the primary tumor, transverse the extracellular matrix, and enter the vasculature. Cells circulate in the blood and some cells eventually extravasate into the extracellular matrix at a distant site to start a secondary tumor.

Prognosis in cancer is generally measured in terms of survival rates, which compares the survival of cancer patients with that of people without cancer who are of the same age, sex, and race (American Cancer Society 2014). The survival rates for most cancers are impressive if tumors are diagnosed when they are still localized to the primary site i.e. the cancer has not metastasized (American Cancer Society 2014). One of the important steps governing metastasis is cell migration through the extracellular matrix before cells enter the vasculature and after cancer cells leave the vasculature. Successfully stopping or even slowing down cancer cell migration has the potential of restricting the tumors to the primary site, from where they can be resected using current surgical methodologies.

1.1 Actin and microtubule cytoskeleton in cell migration

Filamentous actin (F-actin) plays a role in diverse cellular functions, which include endocytosis, cell division, muscle contraction, and cell migration (Goley and Welch 2006, Higgs and Pollard 2001, Korn, Carlier, and Pantaloni 1987). F-actin is polymer of numerous globular actin (G-actin) monomers; only F-actin is known to have biological function (Korn, Carlier, and Pantaloni 1987).

Cells migrating on 2D substrates possess a highly dynamic dense network of actin towards the front of the cell called lamellipodium. Rapid polymerization of actin in the lamellipodium is responsible for generating forces important for cell migration. Polymerization of actin is aided by actin nucleating factors: actin-related protein-2/3 (Arp2/3), formins, and spire (Korn, Carlier, and Pantaloni 1987). The functions of these nucleating factors have been extensively studied in cells cultured on 2D substrates, however, a detailed understanding of what roles these proteins play in cells growing in 3D matrix is lacking. Here I have focused on studying the role of the nucleating factor Arp2/3, and its

activators N-WASp, WAVE1, cdc42, and Cortactin, in 3D cell migration.

Microtubules (MTs) are another important component of the cell cytoskeleton. MTs are hollow cylinders composed of α-tubulin and β-tubulin dimers. In addition to providing mechanical strength and structure to the cell, MTs play a role in various cellular functions, which include vesicle trafficking, cell division, and also cell migration (Etienne‐Manneville 2004, Kaverina and Straube 2011). Here we have systematically designed experiments to first study if microtubule integrity and dynamics matter for 3D cell migration inside collagen I matrix. Then cell lines depleted of microtubule tip binding protein, EB1 and cytoplasmic dynein subunits, light intermediate chain 2 (LIC2) and Heavy chain 1 (HC1) were created to study if and how these individual proteins play roles in 3D cell migration.

1.2 Random walk model to describe cell migration

Since the development of microscopes, numerous cellular phenomena have been observed and analyzed in great depth. Cell migration is one such phenomenon that has been investigated in detail. Many cell migration models have been developed to characterize cell migration patterns observed on flat 2D substrates. One such model that has been extensively used is the persistence random walk model, in which the mean square displacements of cells are fitted to obtain the speed and persistence of cell migration (Dunn 1983, Tranquillo, Lauffenburger, and Zigmond 1988a, Tranquillo and Lauffenburger 1987a, Stokes, Lauffenburger, and Williams 1991a, Stokes and Lauffenburger 1991a, Fooksman et al. 2010, Vroomans et al. 2012). However, this and other current models are not able to accurately describe the cell migration in 3D matrices. We have developed and rigorously tested a cell migration model that accurately describes cell migration inside 3D matrices.

1.3. Thesis Overview

Over the past three or four decades, much of cancer research has been focused on studying cancer cells on flat cell culture dishes. However, under physiological conditions, many of the cancers develop, progress, and metastasize in a complex 3D microenvironment. Cells migrating on 2D substrates are exposed to a uniform environment of nutrient (cell media) and substrate stiffness (cell culture plate), however, cells migrating in 3D matrices may be exposed to locally changing matrix density, pore size, differential concentration of nutrients, and different fiber arrangement. In addition, cancer cells migrating through the extracellular matrix (ECM) produce matrix metalloproteases (MMPs) that cleave ECM proteins. In the following work, we aim to highlight the importance of studying cell migration and other cellular processes (potentially) in a more physically relevant condition. In Chapter 2, we have characterized the role of actin and actin-associated proteins in 3D cell migration. We show that cells inside 3D matrix attained a spindle shaped morphology and grew highly branched protrusions that correlated with the speed of cell migration. In Chapter 3, the role of another major cytoskeletal component, microtubule, in cell migration is explored. We used pharmacokinetic drugs to stabilize and depolymerize the microtubule cytoskeleton; the drugs were more efficient at stopping cell migration in 3D matrix. The role of some key microtubule interacting proteins were also studied. In Chapter 4, we continue our theme of understanding 3D migration and develop a cell migration model that correctly characterizes cell migration in 3D matrices.

CHAPTER 2

The Arp2/3 complex mediates multi-generation dendritic protrusions for efficient three-dimensional cancer cell migration

2.1 Introduction

The Arp2/3 complex is the major actin-nucleating factor that induces the formation of the intracellular dendritic filament network that shapes the lamellipodial protrusive leading edge of motile cells on conventional 2D substrates (Pollard and Borisy 2003a). The Arp2/3 complex is known to have very little biochemical activity when present on its own but its activity is greatly increased in presence of nucleation promoting factors like WASP, WAVE, and Cortactin, and Rho GTPases Cdc42 and Rac1 (Goley and Welch 2006). Cdc42 binds to the GTPase binding domain of the WASP family protein N-WASP (Derry, Ochs, and Francke 1994, Miki, Miura, and Takenawa 1996). This relieves N-WASP from its auto-inhibited confirmation and activates the Arp2/3 complex (Kim et al. 2000). Rac activates the Arp2/3 complex by signaling through another WASP-related protein WAVE (Pollard and Borisy 2003a).

Although the role of the Arp2/3 complex in chemotaxis is somewhat controversial, two recent reports have shown that the Arp2/3 complex mediates the formation of lamellipodium and random-walk cell motility on flat substrates (Suraneni et al. 2012, Wu et al. 2012). However, during development and in the context of disease including cancer and inflammation, cells typically migrate in a 3D microenvironment (Wirtz, Konstantopoulos,

and Searson 2011a, Konstantopoulos, Wu, and Wirtz 2013). Whether and how the Arp2/3 complex regulates protrusion activity and still plays a role in cell motility in the more physiological case of a 3D matrix has not been determined.

In 3D matrices, mesenchymal cells often display dendritic protrusions (Grinnell et al. 2003, Rhee et al. 2007, Li et al. 2010, Friedl and Wolf 2009); however, detailed structural and functional characterization of these protrusions is still lacking. Moreover, to our knowledge, no known specific regulators of protrusions of cells in matrix have been identified. Here we classify cell protrusions based on their time-dependent spatial location in the cell. Our results show that while the protrusions emerging directly from the cell body and prolonging the nucleus (which we call mother protrusions) are specifically regulated by focal adhesion proteins FAK, talin, and p130Cas, the formation of dendritic protrusions (daughter protrusions) that stem from mother protrusions are regulated by the Arp2/3 complex and associated proteins N-WASP, WAVE1, Cortactin, Cdc42, and VASP. The rate of generation (not the length) of daughter protrusions – and associated degree of branching from the mother protrusions - predicts cell speed in 3D matrices. These multi-generation dendritic protrusions are structurally and functionally distinct from well-characterized invadopodia that stem from the basal surface of cancer cells placed on the surface of soft gels, promote local invasion, but do not seem to mediate cell migration.

2.2 Materials & Methods

2.2.1 Cell culture

Human fibrosarcoma HT1080 cells (ATCC) were cultured in Dulbecco's modified Eagle's medium (DMEM, Mediatech) supplemented with 10% (v/v) fetal bovine serum (FBS, Hyclone Laboratories), and 0.005% (w/v) gentamicin (Quality Biological) (Sigma). Human breast carcinoma MDA-MB-231 cells (ATCC) were cultured in DMEM (Mediatech)

supplemented with 10% FBS (Hyclone). Human prostate cancer E006AA cells (a generous gift from Prof. John Isaacs, Johns Hopkins School of Medicine) were cultured in RPMI (Roswell Park Memorial Institute) 1640 media supplemented with 10% FBS (Hyclone) and 100 U penicillin/100 μg streptomycin per milliliter of media (Sigma). Human pancreatic adenocarcinoma SW1990 cells (ATCC) were cultured in RPMI (Roswell Park Memorial Institute) 1640 medium supplemented with 10% FBS (Hyclone) and 100 U penicillin/100 μg streptomycin per milliliter of media (Sigma). HT1080 cells transfected with shRNAs (see below) were grown in medium containing 1 μg/ml puromycin. The cells were maintained at 37°C and 5% CO_2 in a humidified incubator during cell culture and during live-cell microscopy.

2.2.2 Depletion of proteins with shRNAs

The lentivirus vector was generated by co-transfecting the shRNA construct with two other packaging plasmids, pMD.G VSV-G and pCMVΔR8.91 (encoding Gag, Pol, Tat, and Rev) using Lipofectamine 2000 (Invitrogen). Briefly, 293T cells at around 80% confluence were transfected with a mixture of 6 μg of lentiviral shRNA construct, 8 μg of pCMVΔR8.91, and 1 μg of pMD.G VSV-G. The conditioned medium containing the lentivirus was harvested 48 h post transfection and filtered through a 0.4 μm filter (Millipore) to remove cell debris.

For transduction, HT1080 cells were grown to 50-60% confluence in a 6 cm cell culture dish. 2 ml of medium containing lentivirus was mixed with 1 ml of fresh medium containing protamine sulfate (final concentration 10 μg/ml) and added to HT1080 cells. After 8 h incubation, the medium containing the viruses was replaced with fresh medium containing 1 μg/ml puromycin for selection. shRNA constructs targeting various genes were purchased from Sigma Aldrich. Five different shRNA sequences targeting different

regions were chosen. After lentiviral-mediated transduction, western blots were performed and only shRNAs showing more than 85% knockdown were used for subsequent studies. They include:

Arp2/3	*sh36499*	GCTGGCATGTTGAAGCGAAATC,
Arp2/3	*sh36501*	CTACCACATCAAGTGCTCTAAC;
N-WASP	*sh123061*	GCACAACTTAAAGACAGAGAAC,
N-WASP	*sh123062*	CAGGAAACAAAGCAGCTCTTTC;
Cortactin	*sh40273*	CGGCAAATACGGTATCGACAAC;
Cdc42	*sh299931*	CCTGATATCCTACACAACAAAC;
Cdc42	*sh299932*	CAGATGTATTTCTAGTCTGTTC;
WAVE1	*sh122995*	CGCCGTATTGCTGTTGAATATC;
WAVE1	*sh122998*	GCTAAGCATGAACGCATTGAAC

A scrambled shRNA sequence was used as a control, CCTAAGGTTAAGTCGCCCTCGC (Addgene plasmid 1864). Western blots were performed as described previously. The blots were incubated overnight at 4˚C with the following antibodies: rabbit anti-human p34 (1:1000 in 5% milk; Millipore), rabbit anti-human N-WASP (1:1000 in 5% milk; Cell Signaling Technology), rabbit anti-human Cortactin (1:1000 in 5% milk; Cell Signaling Technology), rabbit anti-human Cdc42 (1:1000 in 5% milk; Cell Signaling Technology), and goat anti-β-actin (1:2500 in 5% milk, Santa Cruz). Depletion of talin, p130Cas, VASP, and FAK was conducted as previously described in ref. (Fraley et al. 2010c).

2.2.3 Immunofluorescence microscopy

To visualize the subcellular localization of Arp2/3 and associated proteins, cells were plated on collagen I coated glass bottom 35-mm glass bottom cell culture dishes. The next

day, cells were fixed with 4% paraformaldehyde for 10 minutes, permeabilized with 0.1% Triton X-100 for 10 minutes, blocked with 10% goat serum for 1 h at room temperature, and stained for nuclear DNA, Arp2/3 (p34, 1 μg/ml, Millipore), Wave1 (1 μg/ml, Cell Signaling Technology), N-WASP (1 μg/ml), Cell Signaling Technology), Cortactin (1 μg/ml), Cell Signaling Technology), and Cdc42 (1 μg/ml, Cell Signaling Technology).

Fluorescent micrographs of cells on 2D substrates were collected using a Cascade 1K CCD camera (Roper Scientific) mounted on a Nikon TE2000 microscope with a 60X oil immersion lens. For immunofluorescence in 3D, cells were embedded in 3D collagen as mentioned below (3D collagen I matrix). After 24 h, cells were fixed with 4% formaldehyde for 30 min and permeabilized with extraction buffer consisting of 0.1% Triton-X 100 (v/v) for 30 min. Cells were then incubated with primary antibody (same antibodies as mentioned above, anti-phospho-myosin heavy chain 2A (ser 1943, Millipore), anti-alpha-tubulin (Abcam), 5 μg/ml final concentration) overnight at 4°C and washed 5 times with PBS for 30 min each. Next, the cells were incubated with appropriate secondary antibodies, phalloidin, and DAPI for 2 h at room temperature after which they were washed extensively with PBS (5X for 30 min each). Cells completely embedded inside collagen gels were then imaged at least 150 μm away from the bottom on a Nikon A1 confocal microscope using a 60X water-immersion lens.

2.2.4 Lamellipodium quantification

Lamellipodia of cells growing in 2D substrates were quantified as described previously (Chan et al. 2005, Yang et al. 2007). Briefly, cells were stained for F-actin and fluorescent and phase contrast images were taken randomly for at least 100 cells per condition. Cell boundaries were traced using NIS-Elements image analysis software. Lamellipodia were identified by dense networks of F-actin fluorescence on the front edge of

the cell's perimeter. The ratio of lamellipodia was calculated by dividing the length of the lamellipodia by the total circumference of the cell.

2.2.5 3D collagen I matrix

HT1080 cells were embedded in 2mg/ml collagen I gel as described previously (Fraley et al. 2010b). Briefly, 18,000 cells suspended in 1:1 (v/v) ratio of cell culture media and reconstitution buffer (mention formula here) were mixed with appropriate volume of soluble rat-tail collagen I (BD Biosciences) to obtain a final collagen I concentration of 2 mg/ml. A calculated amount of 1M NaOH was added quickly and the final solution was mixed well to bring the pH to ~7. The cells suspension was added to a 24-well coverslip-bottom cell-culture dish and immediately transferred to an incubator maintained at 37°C to allow polymerization. This density was chosen so as to minimize cell collisions. Fresh medium was added 5 h before imaging.

2.2.6 Protrusion activity and topology of matrix-embedded cells

Phase-contrast images of matrix-embedded cells were recorded 2 min apart for 16.5 h using a Cascade 1K CCD camera (Roper Scientific) mounted on a Nikon TE2000 microscope with a 10X objective lens. For the characterization of protrusion topology, the movies were used to count the total number of mother protrusions, and the number of first-, second-, and third-generation protrusions generated by the cell (e.g. Fig. 2, K-N). The protrusions emanating directly from the cell body, even when split, were termed mother protrusions; protrusions originating from the mother protrusions were termed first-generation, and so on. Because many mother protrusions showed multi-generation protrusions, they were termed dendritic. The degrees of branching are defined as the ratios of the number of first-generation to the number of mother protrusions (Inset, Fig. 2D), the number of second-generation protrusions to the number of first-generation protrusions

(Inset, Fig. 2E), etc. The rate of formation of a protrusion (of any generation) is the number of protrusions that were born, grew, and died for a duration of 90 min. Mitotic cells were not included in the measurements.

2.2.7 Mean-square displacements (MSD) of cells in 2D and 3D

HT1080 cells were embedded in collagen I matrix and low magnification movies were collected as both described above (under Protrusion topology). Single cells were tracked using Metamorph imaging software. A custom MATLAB program calculated the mean square displacement for each cell using the x- and y-coordinates obtained from tracking data using the following equation: $MSD = <[x(t + \Delta t)-x(t)]2 + [y(t + \Delta t)-y(t)]2 >$. We note that this is the 2D projection of essentially 3D cellular movements in the matrix, i.e. we presumed that the movements of the cells were isotropic. To test this assumption, we verified that $<[x(t + \Delta t)-x(t)]2 > \approx < [y(t + \Delta t)-y(t)]2 >$, i.e. we assume that if the mean squared displacements of the cell along arbitrarily chosen x and y axis are equal, then the cell's mean squared displacements in the direction orthogonal z to the (x , y) plane is also equal to those in the x and y directions. Mitotic cells were not included in the measurements.

2.2.8 Imaging and analysis of 3D matrix traction

Cells were embedded in collagen matrix and plated in a 4-chambered dish (MatTek Inc. CA). Cells were then incubated for 24 h in a humidified incubator maintained at 37˚C. 500µl of fresh medium was added to each well 5 h before imaging. Using 488 nm laser for illumination and choosing a set of filters designed to collect reflected light, a reflection-confocal image of the cell and its immediate surrounding gel was captured at an interval of 2 minutes for 2 hours, in a CO_2 and temperature controlled environment using a Nikon A1 Confocal microscope with a 60X water lens. In order to ensure that the three-dimensional

behavior of pulling by the cell is incorporated in the analysis, up to 40 z-planes were imaged at every time point. Moreover, in order to mitigate the possibility of the glass-bottom affecting the local properties of the cell, it was ensured that the imaged cell was at least 150 □ m above the glass-bottom.

Images at each time point were projected along z-direction using the maximum-intensity module on Nikon Elements image-processing software. Subsequently, each sequence of images were exported as tiff files and read into a MATPIV© based code to determine the instantaneous, whole-field deformation map of the imaged gel. A signal-to-noise ratio of 4 was used to eliminate false vectors and interrogation areas were picked to be 16 pixels × 16 pixels, with a targeted overlap of 75% between these areas. Having obtained the instantaneous deformation of the gel between every two successive frames, imaginary circular-regions around the cell were picked to represent beads of diameter 10 pixels. Up to 14 such "computational" beads were placed and their trajectories tracked using the information about whole-field instantaneous deformation of the gel. The mean peak-deformation and the mean net-deformation of the imaginary beads were calculated for cells moving in one direction over the course of one 2 h movie.

2.2.9 Correlation analysis

To access correlation between various motility parameters (MSDs, protrusion topology in 2D and 3D), 11 data points were generated (one data point from each shRNA treatment, one data point from control cells, and one data point from Arp2/3 inhibitor treatment). Each data point represents the average of the particular parameter considered.

2.2.10 Statistics

The mean values ± sem were calculated and plotted using GraphPad Prism software (GraphPad Software). One-way ANOVA test was performed to determine statistical

significance, which is indicated in the graphs using a Michelin grade scale ***$p<0.001$, **$p<0.01$, and *$p<0.05$.

2.3 Results

2.3.1 Transformed cells form multiple-generation dendritic protrusions in 3D matrix

Wild type HT0180 cells, a human fibrosarcoma cell line commonly used to study cell migration (Wolf et al. 2003, Wolf et al. 2007b, Zhou et al. 2008, Sabeh, Shimizu-Hirota, and Weiss 2009), were placed on flat collagen I-coated substrates. These cells formed a wide lamellipodium at their leading edge (Fig. 2, A-E) and, as expected, the Arp2/3 complex and associated proteins, Arp2/3 activator N-WASP and WAVE1 (Rohatgi, Ho, and Kirschner 2000, Rohatgi et al. 1999, Machesky and Insall 1998, Kim et al. 2000, Shakir et al. 2008), N-WASP regulator Cortactin (Wu and Parsons 1993, Weaver et al. 2003, Weaver et al. 2002, Weaver et al. 2001), and N-WASP upstream effector Cdc42 (Rohatgi, Ho, and Kirschner 2000, Rohatgi et al. 1999), localized in their lamellipodium (Fig. 2-1, A-E). In contrast and as observed previously by Yu and Machesky (Yu and Machesky 2012), immunofluorescence microscopy of these cells in 3D collagen I matrices showed Arp2/3, N-WASP, and Cortactin localized to discrete puncta inside the protrusions and also in the cell body (white arrowheads, Fig. 2-6, A-I).

Next, we systematically assessed whether these proteins regulated lamellipodium formation in cells on collagen-I-coated flat substrates. These experiments were conducted to determine whether cells that were shRNA-depleted of these proteins displayed a motility phenotype on 2D substrates and in turn, and assess whether the role of Arp2/3 complex and binding partners in 3D motility could be simply extrapolated from the 2D case. All results presented in the paper were verified using at least two different shRNA constructs (Fig. 2-5, A-E); results obtained with different shRNA constructs were pooled as they were

highly consistent. We found that shRNA-induced depletion of the major subunit p34 of the Arp2/3 complex (a positive control,(Suraneni et al. 2012, Wu et al. 2012)) as well as N-WASP significantly and consistently diminished the formation of the lamellipodium at the leading edge of cells moving on 2D substrates (Fig. 2-1, H-K) and as assessed by live-cell microscopy, reduced 2D cell speed (Fig. 2-1, L and M). A simple assessment of cell speed consists of measuring mean squared displacements (MSD) of cells at different time scales, which here ranged between 2 min (the time between movie frames) and 16.5 h (the total duration of the movie). Short time-scale cell speed (e.g. evaluated at 16 min) and long time-scale cell speed (e.g. evaluated at 1 h) were both regulated by the Arp2/3 complex and associated proteins N-WASP, WAVE1, Cdc42, and Cortactin (Fig. 2-1, L and M). We note that the drastic reduction of lamellipodium formation by depletion of p34 and N-WASP (Fig. 2-1 K), reduced, but did not completely prevent, cell migration on 2D substrates (Fig. 2-1, L and M). For the cases examined here, correlation between 2D motility and lamellipodium formation was strong: cell showing little lamellipodium moved slowly, while cells showing extensive lamellipodium moved rapidly on 2D substrates (Fig. 2-1, H-K and Fig. 2-1, L and M).

Using the same cells as used in the above 2D studies, we determined whether the Arp2/3 complex and associated proteins still played a role in 3D cell migration for well-dispersed cells embedded in a matrix at least 400 μm away from the bottom substratum to avoid edge effects (Fraley et al. 2011). The depletion of the Arp2/3 complex or associated proteins induced a robust phenotype of reduced 3D cell speed (Fig. 2-1, N and O). Since shRNA-based depletion of p34 may not be complete, we examined the migration of matrix-

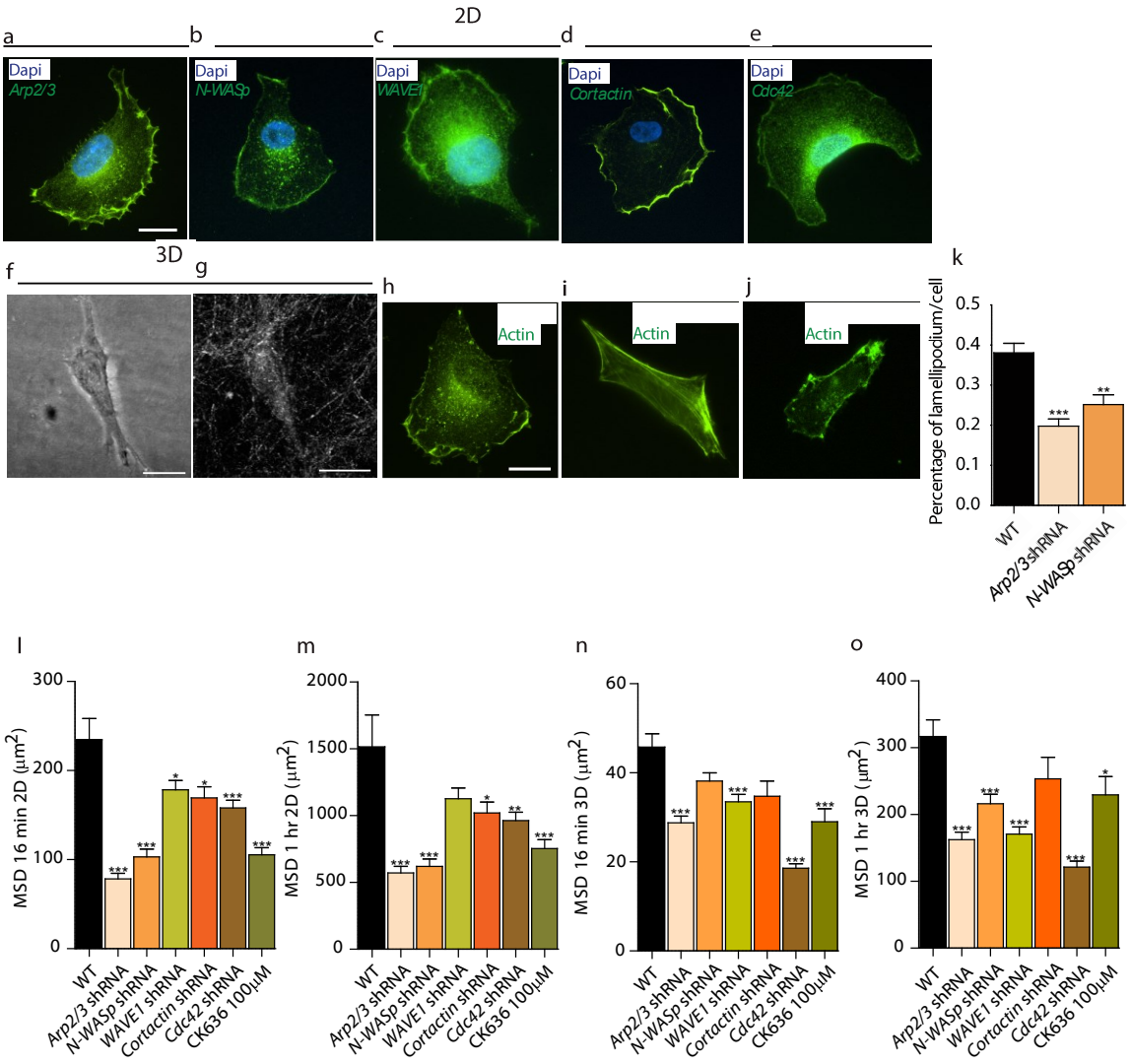

Figure 2-1. Organization and role of Arp2/3 complex and associated molecules in cells

A-E. The Arp2/3 complex (A), N-WASP (B), WAVE1 (C), Cortactin (D), and Cdc42 (E) are localized primarily at the leading edge (lamellipodium) of motile cells placed on 2D collagen I-coated substrates. Human fibrosarcoma cells (HT1080) were stained with DAPI (nuclear DNA) and using antibodies against these proteins; images were obtained by immunofluorescence microscopy. **F and G**. Cells form no apparent wide lamellipodium when embedded in a 3D collagen I matrix; rather they form long pseudopodial protrusions that stem directly from the cell body, and branch off into the matrix. Images of the HT1080 cell and its surrounding collagen I matrix were obtained by confocal phase contrast microscopy (F) and confocal reflection microscopy (G), respectively. **H-K**. Compared to control cells transfected with non-targeting shRNA (H), shRNA-induced depletion of the p34 subunit of the Arp2/3 complex (I) or N-WASP (J) induces the reduction of lamellipodium

Figure 2-1 (continued)

formation, as measured by the ratio of the length of lamellipodium marked by actin stain (phalloidin) and that of the cell periphery (method described in ref. (Chan et al. 2005)) (K). For each condition, N=3 and a total of 100 cells were probed. ***: $p<0.001$, **: $p<0.01$. **L-O**. Regulation of 3D and 2D cell speed (measured as mean squared displacements at considered time lags; see Methods) by the Arp2/3 complex, N-WASP, WAVE1, Cortactin, and Cdc42, as well as inhibition following cell treatment by 100 μM of the Arp2/3-complex-specific inhibitor CK636. MSDs were evaluated at time lags of 16 min (L and N), and 1 h (M and O).

embedded cells treated with specific Arp2/3 inhibitor CK636: these treated cells also showed greatly decreased cell speed, to an extent similar to that caused by shRNA depletion of p34 demonstrating a highly consistent phenotype of reduced 3D migration (Fig. 2-1, N and O).

We asked whether regulation of cell speed by the Arp2/3 complex and associated proteins on 2D substrates was predictive of their regulatory role in 3D cell migration. On 2D collagen I-coated substrates, Arp2/3/N-WASP/WAVE1/Cortactin/Cdc42 regulated cell migration as in the 3D case: the presence of these proteins enhanced cell speed (Fig. 2-1, L and M). However, close examination of the data showed that the extent of correlation between 2D and 3D motility parameters (MSDs) was limited (Pearson correlation coefficient << 1; Fig. 2-5, F and G), suggesting a distinct mode of action for the Arp2/3 complex and associated proteins in 3D motility.

To determine the mechanism of Arp2/3-based regulation of 3D cell migration, protrusion morphology and dynamics of matrix-embedded cells were quantitatively assessed. However, unlike cells on collagen-coated surfaces, the same cells fully embedded inside a 3D collagen I matrix displayed no clear lamellipodia-like structure, as assessed by high-magnification microscopy (Fig. 2-1 F and Fig. 2-5, J-L). Rather, cells showed a highly stretched body composed of an average of 1-2 major pseudopodial protrusions that stemmed from the cell body, prolonging the nucleus. The average thickness of these major protrusions was ~5 μm, which is ~10 times thicker than filopodial protrusions observed in cells on substrates (Fig. 2-1 F; Fig. 2-5, J-L; Table 1). Another important feature that sets apart pseudopodial protrusions from filopodia is the presence of microtubule inside these protrusions whereas filopodia contain only filamentous actin (Fig. 2-6, M-O).

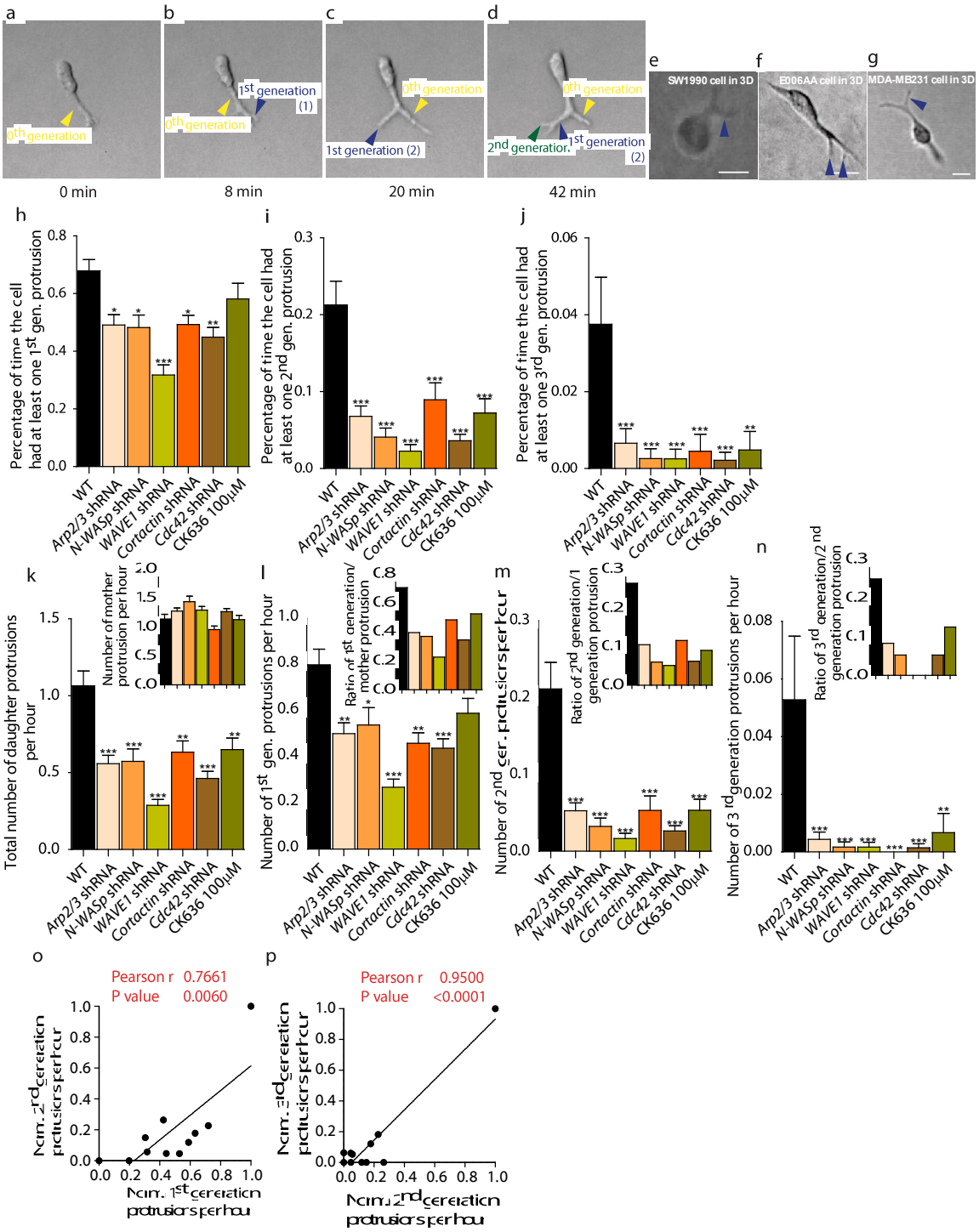

Figure 2-2. Cells in matrix form multi-generation dendritic pseudopodial protrusions.

A-D. Dynamic formation of multi-generation, dendritic pseudopodial protrusions by a matrix-embedded cell. Arrows show the formation of a mother protrusion (yellow arrow; protrusions that stem directly from the cell body), as well as first- (blue) and second-generation (green) daughter protrusions, which stem from a mother

Figure 2-2 (continued)

protrusion. Times are indicated in the panels. **E-G.** Human pancreatic carcinomas (SW1910, E), human prostate carcinomas (E006AA, F), and human epithelial breast carcinomas (MDA-MB-231, G) also form daughter protrusions emanating from mother protrusions when embedded in a 3D collagen I matrix. Scale bar for all micrographs, 20 □ m. **H-J**. Average fraction of time spent by matrix-embedded cells displaying at least one first-generation protrusion stemming from a mother protrusion (H), at least one second-generation protrusion (I), and at least one third-generation protrusion (J), and associated regulation by the Arp2/3 complex, N-WASP, WAVE1, Cortactin, and Cdc42, as well as inhibition following cell treatment by 100 □ M of the Arp2/3-complex-specific inhibitor CK636. **K**. Total number of daughter protrusions and mother protrusions (*Inset*) generated per hour per cell (rates of formation). **L-N**. Number of first-generation protrusions (L), second-generation protrusions (M), and third-generation protrusions (N) generated per hour per cell. *Insets*: number of first-generation protrusions per mother protrusion (Inset, L), number of second-generation protrusions per first-generation protrusion (Inset, M), and number of third-generation protrusions per second-generation protrusion (Inset, N). **O and P**. Correlations between the rates of formation of first- and second-generation protrusions (O) and rates of formation of second- and third-generation protrusions (P). For all panels, cells were monitored for 16.5 h. ***: $p<0.001$, **: $p<0.01$, and *: $p<0.05$. For each condition, N = 3 and at least 60 cells were probed.

Matrix-embedded cells developed one or two zeroth-generation mother protrusions, defined as the protrusions that extend directly from the nuclear area. Zeroth-generation protrusions branched into first-generation protrusions, which typically branched themselves further into second-generation protrusions (Fig. 2-2, A-D). These second-generation protrusions rarely branched themselves further into third-generation daughter protrusions. From here on, zeroth-generation mother protrusions will be referred as mother protrusions and all the first-, second- and third-generation protrusions will be collectively referred as daughter protrusions. We note that we made sure to use time-lapse movies as opposed to still pictures to identify and quantify protrusions. That way, we could follow the birth, growth, and retraction of all protrusions, helping delineating mother from daughter protrusions. The fractions of time spent by WT cells in a matrix showing first- and second-generation were ~70%, ~22%, respectively (Fig. 2-2, H and I), i.e. dendritic branching from mother protrusions was a common occurrence in HT1080 cells in 3D matrix.

Importantly, dendritic protrusions were not unique to HT1080 cells and were also readily observed in human pancreatic carcinomas (SW1910, Fig. 2-2 E), human prostate carcinomas (E006AA, Fig. 2-2 F), and invasive human breast carcinomas (MDA-MB-231, Fig. 2-2 G), when these cells were fully embedded inside a 3D matrix. These cells formed a wide lamellipodium when migrating on 2D substrates, but again showed no clear lamellipodial structures in 3D matrices (Fig. 2-1 F and Fig. 2-5, J-L).

2.3.2 The Arp2/3 complex and associated proteins mediate dendritic protrusion activity

Given the role of the Arp2/3 complex in nucleating dendritic actin assembly *in vitro*, we asked whether the Arp2/3 complex regulated the dendritic protrusive activity and topology of protrusions in cells in matrix. We found that the fractions of time during which p34-depleted cells displayed at least one first-, one second-generation, and one third-

generation pseudopodial protrusions were reduced by 40%, 75%, and 87%, respectively, compared to control cells (Fig. 2-2, H-J). The formation of daughter protrusions, but not mother protrusions, was drastically reduced (Inset, Fig. 2-2 K). The rate of formation of an n^{th}-generation protrusion is defined here as the number of protrusions generated per hour. Moreover, the degrees of branching, i.e. the numbers of first-generation daughter protrusions per mother protrusion (Inset, Fig. 2-2 L), second-generation protrusions per first-generation protrusion (Inset, Fig. 2-2 M), and third-generation protrusions per second-generation protrusion (Inset, Fig. 2-2 N), were all significantly reduced.

This significant reduction of daughter branches and degree of branching from mother protrusions were confirmed by treating cells with the Arp2/3 complex inhibitor CK636. Cells treated with Arp2/3 inhibitor CK636 showed greatly decreased dendritic protrusive branching, to an extent similar to that caused by shRNA depletion of p34 (Fig. 2-2, H-N). Importantly, while the Arp2/3 complex mediated protrusive branching off from mother protrusions (Fig. 2-2 K), it did not mediate the formation of mother protrusions (Inset, Fig. 2-2 K), which suggested distinct mechanisms for the formation of mother *vs.* daughter protrusions. These results show that a variety of human cancer cells in matrices, but not on flat substrates, feature highly dendritic protrusions with rates of formation of daughter protrusions and degree of branching tightly regulated by the Arp2/3 complex.

Biochemical data indicate that F-actin nucleating ability of the Arp2/3 complex is greatly enhanced by N-WASP, WAVE1, Cortactin and Cdc42 through direct or indirect binding interactions (Kowalski et al. 2005, Tapon and Hall 1997, Uruno et al. 2001, Shakir et al. 2008). Here we found that the degree of protrusive branching was reduced in N-WASP-depleted cells to similar extents as in p34-depleted cells (Fig. 2-2, H-N). The fraction of time during which N-WASP-depleted cells displayed at least one first-generation, one second-

generation, or one third-generation pseudopodial protrusions were reduced by 33%, 85% and 98%, respectively, compared to control cells (Fig. 2-2, H-J), similarly to the Arp2/3 complex. We observed a much larger effect in WAVE1-depleted cells and the fractions of time during which the WAVE1-depleted cells displayed at least one first-generation, one second-generation, or one third-generation were reduced by 54%, 89% and 94%, respectively compared to control cells (Fig. 2-2, H-J). The degree of protrusive branching from mother protrusions was decreased in Cdc42 and Cortactin-depleted cells to similar extents as in p34-depleted cells and N-WASP-depleted cells (Fig. 2-2, K-N). We also found that changes in the rates of formation of first-generation protrusions modulated by Arp2/3/N-WASP/WAVE1/Cortactin/Cdc42 correlated strongly with changes in the rates of formation of second-generation protrusions by the same molecules (Fig. 2-2, O and P), which suggests that the same molecular mechanisms support the formation of first- and second-generation protrusions.

Finally, similar to the Arp2/3 complex, N-WASP, WAVE1, Cortactin, and Cdc42 did not play an important role in the formation of mother protrusions (Inset, Fig. 2-2 K), further suggesting distinct mechanisms for the formation of mother and daughter protrusions. These results suggest that perturbations of the Arp2/3 complex through its activators N-WASP and WAVE1, or through the N-WASP regulator Cortactin and effector Cdc42, or through direct depletion, had the similar effect of specifically reducing protrusive dendritic branches.

2.3.3 Mother and daughter protrusions are differentially regulated

Since mother and daughter protrusions were differentially regulated, we asked whether one could identify molecules that specifically regulated mother protrusions, not daughter protrusions. A phenotypic screen revealed that scaffolding protein p130Cas and

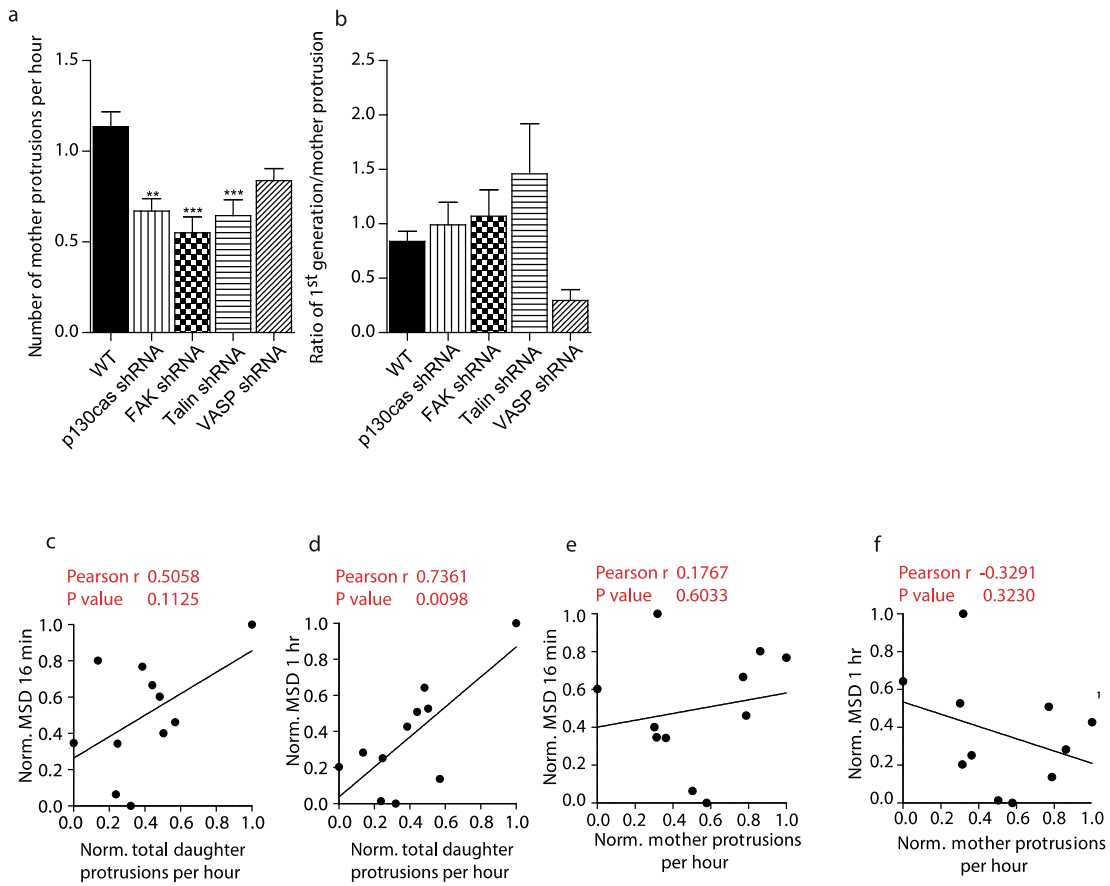

Figure 2-3. Daughter protrusions – not mother protrusions – regulate 3D cell speed through the Arp2/3/N-WASP/Cortactin/Cdc42 module.

A and B. Total number of mother protrusions produced per hour (A) and degree of branching from mother protrusions (the number of 1st generation protrusions per mother protrusion) (B) in FAK-, talin-, p130Cas-, and VASP-depleted cells. For all panels, cells were monitored for 16.5 h. ***: $p<0.001$, **: $p<0.01$, and *: $p<0.05$. For each condition, N = 3 and at least 60 cells were probed for protrusion analysis. **C-F**. Assessment of correlation between 3D cell speeds evaluated at time lags of 16 min (C and E) and 1 h (D and F) and the rates of formation of daughter protrusions (C and D) and mother protrusions (E and F).

focal adhesion proteins, talin and focal adhesion kinase (FAK) regulated the formation of mother protrusions, but not the degree of branching from mother protrusions in matrix-embedded cells (Fig. 2-3, A and B). Although not statistically significant, focal adhesion/lamellipodium protein VASP seemed to regulate both daughter and mother protrusions (Fig. 2-3, A and B). Together these results suggest that mother and daughter protrusions are molecularly distinct and differentially regulated. Moreover, through a highly consistent and robust phenotype, these results further demonstrate the specificity of the role of the Arp2/3 complex in mediating the formation of dendritic daughter protrusions in 3D matrix.

What is the functional importance of dendritic daughter protrusions? Pearson assessment of the extent of correlation between 3D cell speed and the rate of generation of all (mother + daughter) protrusions together or separately revealed that while the number of mother protrusions was not predictive of cell speed, 3D cell speed strongly correlated with the number of daughter protrusive branches. These results suggest the rate of formation of daughter protrusions (Fig. 2-3, C and D) - not the rate of formation of mother protrusions (Fig. 2-3, E and F) - regulates cell migration in 3D matrix at both short and long time scales. Since the rates of formation of first- and second-generation protrusions correlate with each other (Fig. 2-2, O and P), this correlation with cell speed held for the rate of formation of first-generation protrusions and the rate of formation of second-generation protrusions.

Next we asked whether the length of mother protrusions and/or daughter protrusions correlated with cell speed. We found that the length of daughter protrusions was not correlated with cell speed (Fig. 2-5 H). Similarly, the length of mother protrusions did not correlate with cell speed (Fig. 2-5 I). Together these results suggest that the number of dendritic protrusions predict cell speed in 3D matrices, which was not a result predictable

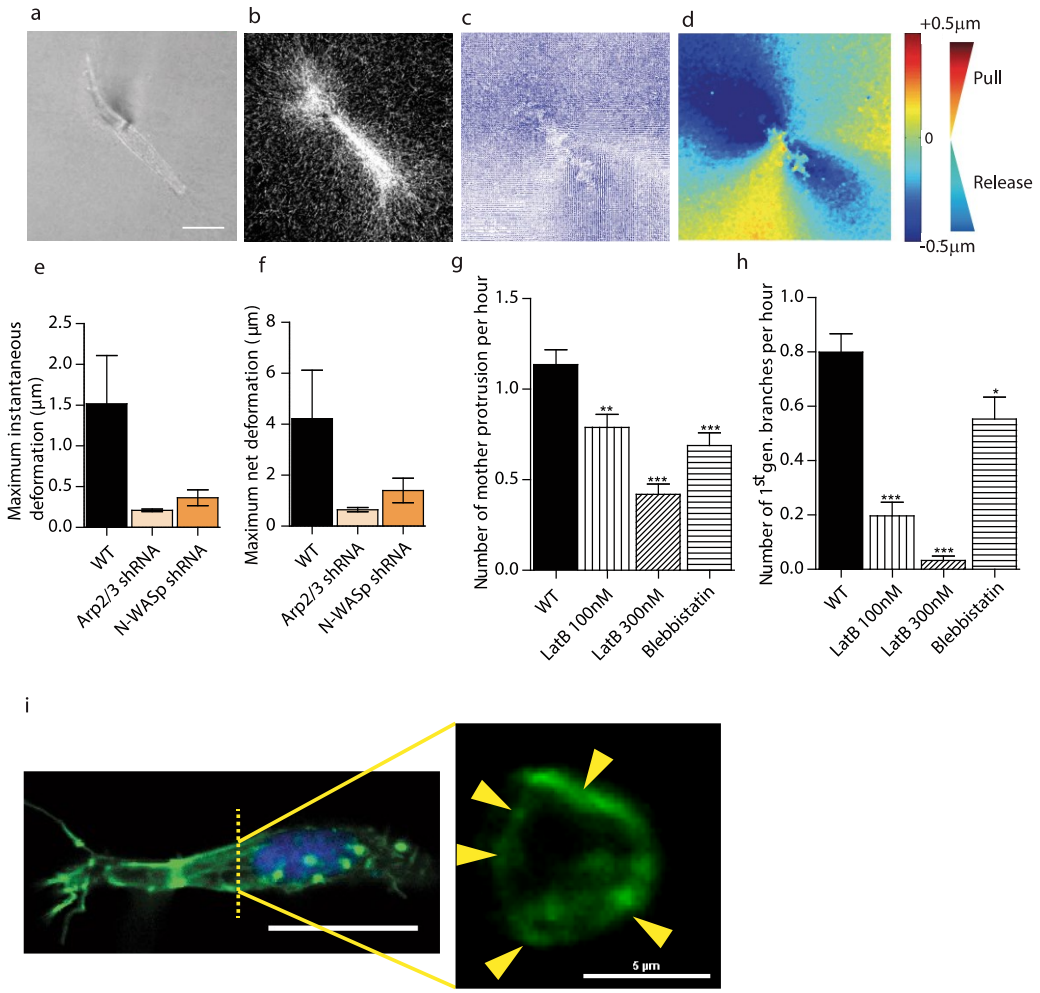

Figure 2-4. Arp2/3 and N-WASP mediate local matrix traction during 3D cell migration and actin architecture of cells.

A-D. Particle (PIV) method used to map the time-dependent deformation field of the matrix generated by individual cells in a 3D matrix. Phase contrast (A) and reflection confocal micrograph (B) are simultaneously recorded every 2 min for 2 h to generate instantaneous strain fields of the matrix (C) and determine regions of matrix traction (red; matrix movement towards the cell) and matrix release from the cell (blue; movement away from the cell) (D). **E and F**. Average instantaneous deformation (E) and maximum deformation (F) of the matrix of fiduciary points located at ~10□ m distance from the cell. **G and H**. Rate of formation of mother protrusions (G) and daughter protrusions (H) for control cells and cells treated with actin depolymerizing drug latrunculin B and myosin II inhibitor blebbistatin. **I**. Architecture of the actin filament network in matrix-embedded cells evaluated by confocal microscopy. Maximum confocal projection (left panel) shows the

elongated morphology and side protrusions in cells in matrix. Cross sections of the same cell (right panel) reveal that the actin network in protrusions is constituted of cortical bundles. Arrows indicate distinct longitudinal actin filament bundles positioned at the periphery of cell protrusions.

from the conventional 2D case because cellular protrusions have fundamentally different topology in 3D matrices (Figs. 1-1 and 1-2 and Table 1).

2.3.4 The Arp2/3 complex and associated proteins regulate matrix traction

To further determine how the Arp2/3 complex modulated 3D cell migration, we asked whether changes in dendritic branching from mother protrusions by the Arp2/3 complex and associated proteins was accompanied by a differential ability of cells to apply traction forces on their surrounding matrix. Using time-resolved reflection confocal microscopy, the movements of collagen fibers in the vicinity of migrating cells were monitored (Fig. 2-4, A-D). A customized particle image velocimetry (PIV) software allows us to track time-dependent local matrix deformation with high spatial resolution (Fig. 2-4C). Cells pulled on their surrounding matrix and then asymmetrically released the matrix for net movements (Fig. 2-4D). We found that the extent of deformation of the matrix was reduced upon p34 depletion and N-WASP depletion (Fig. 2-4, E and F).

Treatment of matrix-embedded cells with F-actin depolymerizing drug latrunculin B and to a lesser extent with myosin II inhibitor blebbistatin reduced the formation of both mother and daughter protrusions (Fig. 2-4, G and H). This suggests that actin filament assembly and acto-myosin contractility are required for the generation of mother and daughter protrusions. Immunofluorescence microscopy showed phospho-myosin IIa co-localized with actin fibers: regions with higher actin content featured higher content in phosphorylated myosin (Fig. 2-6, J-L, white arrow heads). Due to inherent technical difficulties, the actin filament structure of matrix-embedded cells could not be assessed by electron microscopy; however, high-resolution confocal microscopy of actin organizations revealed that actin filaments in both mother and daughter protrusions were concentrated at the cortex of the protrusions (Fig. 2-4 I). In order to avoid any edge effects, we imaged cells

at least 150 μm from the bottom of the dish. Confocal cross sections revealed the presence of thick filament bundles that followed the length of mother and daughter protrusions and were confined to and spatially dispersed along their cortex (Fig. 2-4 I). The average width of these cortical bundles of F-actin was ~1μm. Actin distribution in these protrusions is different from that of a conventional filopodia in the 2D case, which typically contain a single core bundle of actin filaments (Vignjevic et al. 2003). In the 3D case, protrusions contain multiple bundles of actin filaments and they are located at the cell cortex (Khatau et al. 2012).

2.4 Discussion

The Arp2/3 complex and its activators play important roles in cell migration on 2D substrates (Suraneni et al. 2012, Wu et al. 2012), but their roles in 3D migration have not been elucidated. The major finding of this paper is that the branched protrusions – in particular terminal daughter protrusions – displayed by cells in 3D matrices are specifically regulated by the Arp2/3 complex and its activators and are determinants of cell migration and matrix traction. Of course, this result does not mean that mother protrusions are not required for 3D motility, since they are required for the formation of the daughter protrusions. Rather, our data suggests that as soon a minimum number of mother protrusions is generated (seemingly ~1.2 per hour; Inset, Fig. 2-2 K), then cell speed is set by the Arp2/3/N-WASP/WAVE1/Cortactin/Cdc42-regulated degree of branching from these mother protrusions. Hence, the Arp2/3 complex regulates 3D cell motility by modulating the ability of cells in matrix to form dendritic protrusions.

It is important to note that although the depletion of Arp2/3/N-WASP/WAVE1/Cortactin/Cdc42 reduced cell speed in both 2D and 3D, the levels of effect were significantly different. This does not mean that these proteins regulate cell

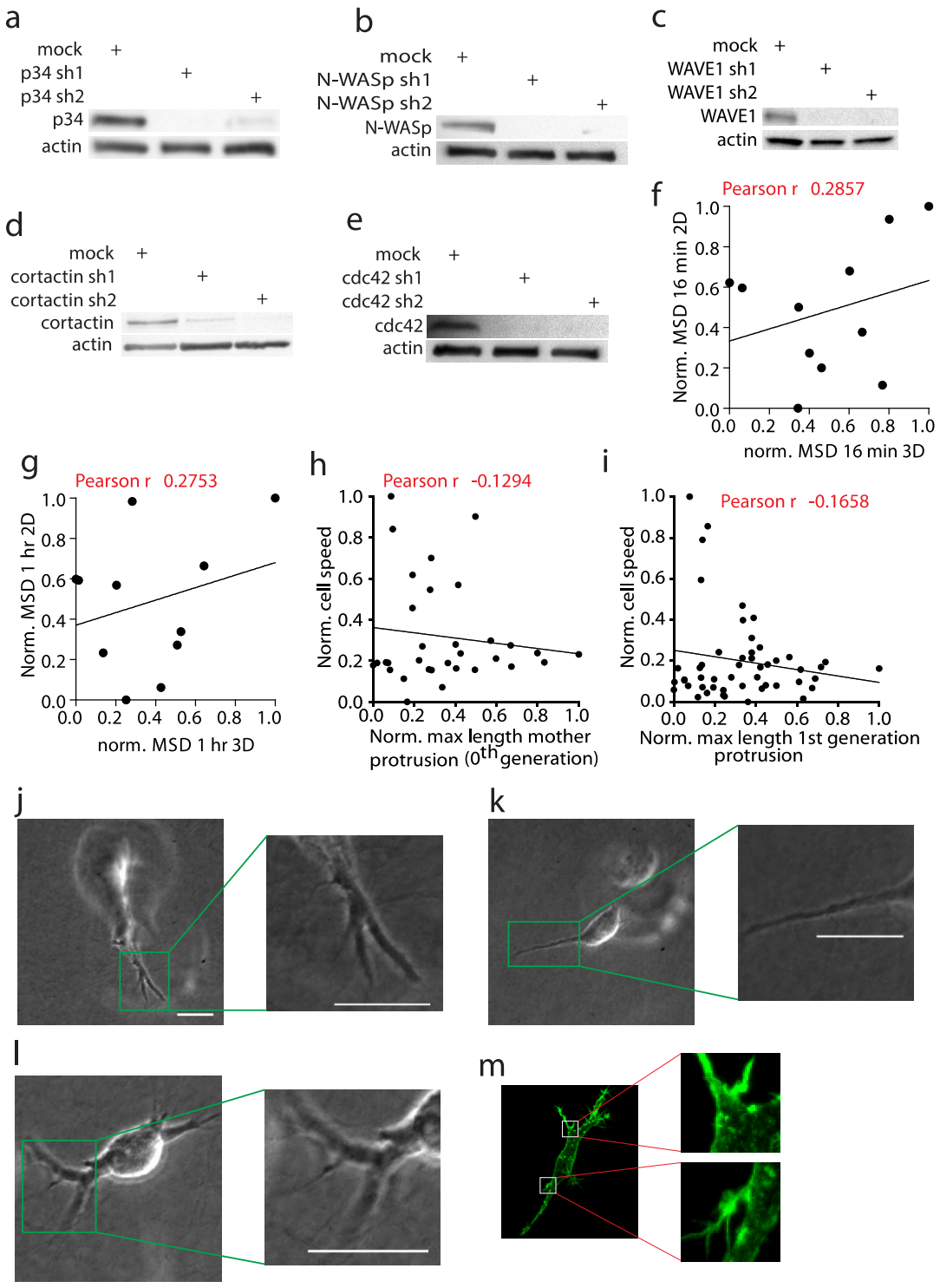

Figure 2-5. Correlations between 2D and 3D and no clear lamellipodia observed in cells in 3D matrix. **A-E.** Western blots of control cells and cell depleted of p34, N-WASP, WAVE1, Cortactin, and Cdc42 for two different constructs**. F and G.** Pearson-based assessment of correlation between 2D and 3D MSDs at time lags of 16 min and 1 h. **H and I.** Assessment of correlation between 3D cell speed and mother protrusions (H) and

Figure 1-5 (continued)

first-generation protrusions (I). **J-L.** Cells embedded inside 3D collagen matrices showed branched protrusions, which are topologically different from lamellipodial protrusions. Images were collected at least 150 μm from the bottom of the collagen gel at 60X magnification. **M.** Immunostaining for actin using phalloidin to show mother protrusions give rise to daughter protrusions (*Inset, top and bottom*).

migration the same way: this is why we conducted a rigorous comparison that showed a poor global correlation between 2D and 3D migration speed, i.e. the relative roles of these proteins in 2D and 3D migration are significantly different when all these proteins are assessed together, as opposed to one at a time.

Another important observation is that cells in 3D showed no clear lamellipodium (Fig. 2-5, J-L), a prominent process for cell on 2D surfaces. While, we observed no wide lamellipodium, it is still possible that the tips of side branches show small lamellipodium-like protrusions. However, such a structure would have to be smaller than a couple of microns. Moreover, terminal dendritic protrusions move along collagen fibers, which in the present conditions are only <120 nm in diameter (Raub et al. 2007, Christiansen, Huang, and Silver 2000), which would not be able to support the formation of flat lamellipodial structures, unlike cells on 2D substrates.

We note that the multi-generation dendritic protrusions described in this paper are structurally and functionally distinct from well-characterized finger-like structures formed by adjoining endothelial cells in 3D matrix and invadopodia formed at the basal surface of cells placed on the surface of soft gels (Table 1). This phenomenon, also known as cell sprouting, is well described in endothelial cells (Jakobsson et al. 2010). The protrusions we describe here are part of the same cell. These dendritic protrusions are also distinct from invadopodia, which are actin and actin-related protein-rich membrane extensions that some invasive tumor cells grow from the ventral surface in contact with the extracellular matrix (Buccione, Orth, and McNiven 2004, Buccione, Caldieri, and Ayala 2009, Clark et al. 2007, Weaver 2008, Murphy and Courtneidge 2011). Invadopodia have an average width of 0.5-2 μm and a length of ~2 μm and, most importantly, are not branched (Murphy and Courtneidge 2011). Although Arp2/3 and N-WASP are associated with invadopodia

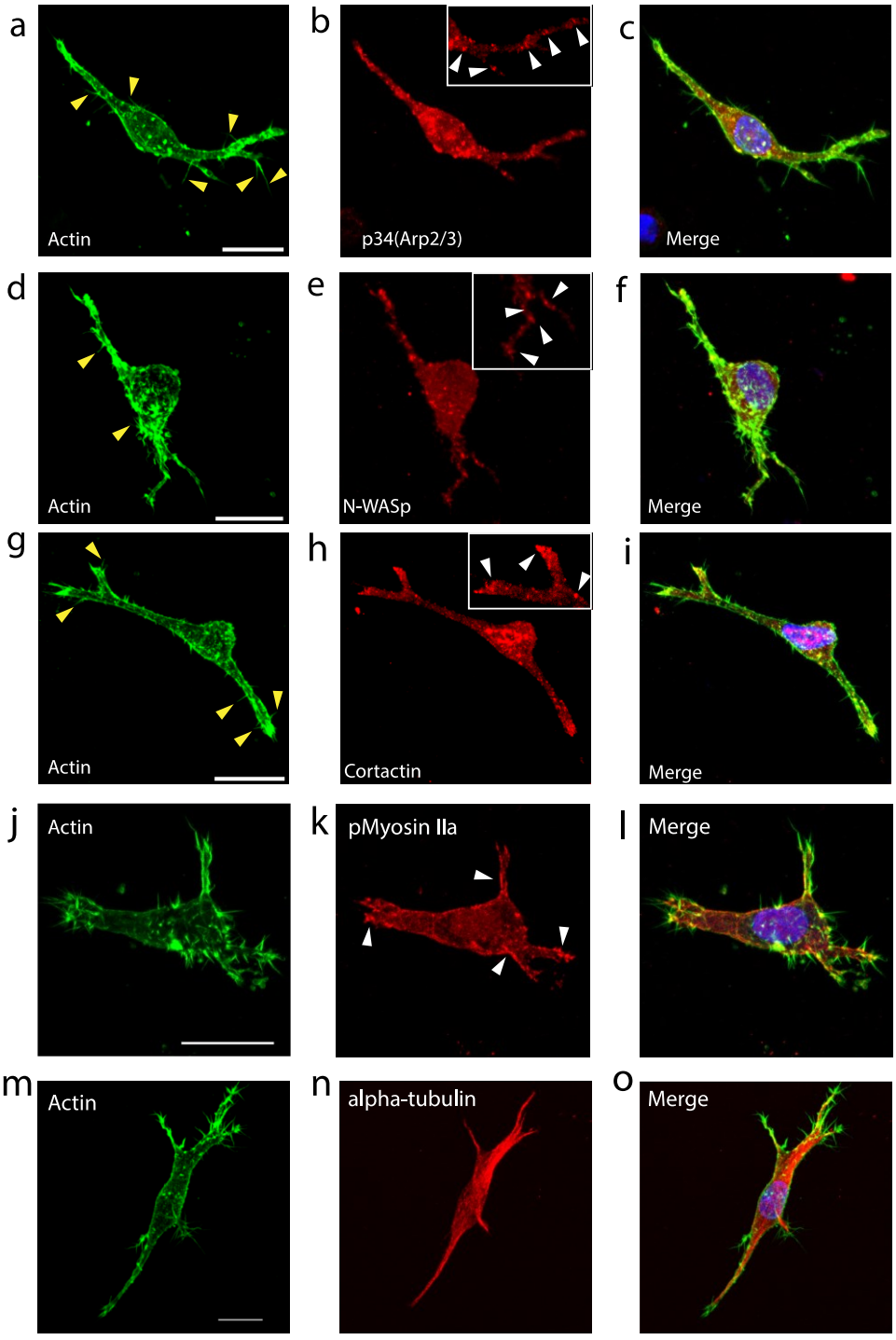

Figure 2-6. Localization of Actin, Arp2/3, N-WASp, Cortactin, pMyosin IIa, and microtubule in cells in 3D matrix.

A-I. Subcellular localization of the Arp2/3 complex, N-WASP, and Cortactin in cells embedded inside 3D collagen I matrix as assessed by immunofluorescence microscopy. Yellow arrowheads point to filopodia-like

Figure 2-6 (continued)

protrusions consisting of only actin, white arrowheads point to puncta of Arp2/3, N-WASP, and Cortactin. **J-O. C**ells stained with phalloidin (Actin) and antibodies for phospho-myosin IIa and alpha-tubulin.

(Weaver 2008), invadopodial structures differ from 3D pseudopodial protrusions in length (2 □ m *vs.* ~10-60 □ m), topology (linear *vs.* dendritic), function (invasion *vs.* migration), location in the cell (basal *vs.* all around the cell surface), and protein content (F-actin and associated proteins *vs.* F-actin, associated proteins and microtubule) (Table 1).

Recent work suggests cells in 3D matrices undergo two modes of migration: amoeboid (integrin- and MMP-independent gliding migration) and mesenchymal (integrin- and MMP-dependent migration) (Wolf et al. 2003, Sabeh, Shimizu-Hirota, and Weiss 2009, Huttenlocher and Horwitz 2011). However, for cancer cell migration in gels made of acid-extracted collagen I, as used here, MT1-MMP inhibition or silencing blocks invasive activity of HT1080 cells in 3D collagen I matrix and we do not observe amoeboid migration (Sabeh, Shimizu-Hirota, and Weiss 2009, Bloom et al. 2008).

The presence of cortical actin filament bundles in both mother and daughter protrusions suggests that these actin bundles in the mother protrusions branch off into actin bundles in daughter protrusions, unlike core bundles in filopodia for cells on 2D substrates (Table 1, Fig. 2-5 M). Therefore, the actin-based mechanism of formation of daughter protrusions from mother protrusions in cells in 3D matrix is distinct from the actin-based mechanism of formation of filopodia from lamellipodium in cells on 2D substrates, which stem from the mixed orthogonal network/bundles of the lamellipodium (Vignjevic et al. 2003).

In sum, this study reveals that highly branched protrusions in cells in matrix, which are specifically regulated by the Arp2/3 complex and associated proteins, play a critical role in 3D cell motility (Table 1).

Type of protrusions	Width (□m)	Length (□m)	Number per cell at any time	Topology	F-actin organization	Arp2/3	N-WASP	Regulatory role in cell motility
2D case								
Lamellipodium	20-50	10	~1	Thin and wide	Dendritic orthogonal meshwork + bundles	Yes	Yes	Yes
Filopodium	<1	~1	~10	Cylindrical; no dendrites	Single core bundle	No	No	Yes
Invadopodia	0.5-2	>2	10-50	Short and thin	Actin associated proteins surround actin core	Yes	Yes	No
3D case								
Mother protrusion	2.5-10	10-60	~1	Cylindrical	Multiple cortical bundles	Yes	Yes	No
First-generation daughter protrusion	2-5	10	~0.5	Cylindrical; dendrites	Multiple cortical bundles	Yes	Yes	Yes

Table 2-1. Morphological and functional differences between protrusions formed by cells in the 2D and 3D cases.

Differences in length and lateral dimensions, topology, F-actin organization, and regulatory roles played by lamellipodia-specific proteins Arp2/3 and N-WASP between pseudopodial protrusions formed by cells in 3D matrix and lamellipodial/filipodial/invapodial protrusions formed by the same cells on 2D substrates. Results compare WT HT1080 cells on collagen I-coated substrates and these cells inside a collagen I matrix.

CHAPTER 3

EB1 and cytoplasmic dynein mediate protrusion dynamics for efficient three-dimensional cell migration

3.1 Introduction

Cell migration is critical in a myriad of physiological and pathological phenomena, including embryonic development and tissue/organ morphogenesis, immunological responses, and cancer metastasis (Ridley et al. 2003, Raftopoulou and Hall 2004, Machesky and Way 1998). Rapid assembly and reorganization of cytoskeletal proteins F-actin and microtubule are the driving factors that generate the necessary forces for cell migration and maintain cell polarity, respectively, at least for migration on 2D substrates (Vladar, Antic, and Axelrod 2009, Ridley et al. 2003, Giri et al. 2013). Thanks to powerful high-magnification microscopes and highly quantitative functional biophysical assays, much of what we know about human cell migration – for instance, the role of the lamellipodium, the nucleus, focal adhesion proteins, myosin-based contractility – has stemmed from careful cell-migration studies on flat substrates. However, post-EMT sarcoma cancer cells and fibrosarcoma cells (used extensively in cell migration studies) rapidly encounter a 3D environment constituted of ECM molecules, in particular type I collagen (Frantz, Stewart, and Weaver 2010, Hall et al. 1985). For cells fully embedded in a 3D matrix, current versions of a wide range of microscopes such as total internal reflection microscopy (TIRM), super-resolution

microscopy (STORM, PALM), electron microscope and biophysical tools such as the cell stretcher and AFM are completely unsuitable for 3D migration studies.

Recent studies have highlighted how key proteins and organelles that play a critical role in conventional 2D migration, do not necessarily play a significant role in 3D migration, and *vice versa*. For instance the Arp2/3 complex-based module for dendritic assembly of F-actin and associated regulatory/activator proteins N-Wasp, Cdc42, WAVE1, and cortactin have remarkably different effects on cell migration in 2D and 3D migration (Giri et al. 2013). Similarly focal adhesion proteins vinculin, talin, zyxin, FAK, and p130Cas have roles in 3D migration not necessarily predicted by the 2D case (Giri et al. 2013, Fraley et al. 2012, Fraley et al. 2010b). Actin filaments in cells in 3D matrix exploit the nucleus, typically positioned in the middle of cell, as mechanical support protrusions to power cell migration in 3D matrix. Cells in 3D matrix form no clear lamellipodium or filopodia commonly observed in mesenchymal migratory cells on substrate; rather they form highly dendritic protrusions. Hence extrapolating the role of proteins and organelles in 3D cell migration from the 2D case is not fruitful (Giri et al. 2013, Fraley et al. 2010b). Part of the reason is that cells in 3D matrix are not exposed to a symmetric biochemical and compliant environment (culture medium on top and stiff ECM-coated underlying substratum), which artificially polarize cells apically, potentially masking functions of proteins.

The role of microtubules and associated regulatory and motor proteins in 3D migration is largely unknown. Studies with cells on 2D substrates suggest that microtubules are dynamic polymers, which cycle between phases of growth and catastrophe, and this dynamic structure is maintained by coordinated activity of a large number of proteins, including microtubule plus-end tip-tracking proteins (+TIPs), dynactin, and dynein. Dynamic microtubules are required for maintaining directed (polarized) cell migration on 2D

substrates (Kaverina and Straube 2011). Microtubule dynamics is regulated by several proteins, prominent among them are EB1 and dynein (LIC2 and HC1), which also regulate vesicular trafficking. Whether EB1 and dynein and associated functions (i.e. vesicular trafficking, microtubule dynamics) play any role in 3D cell migration is also unknown.

EB1 is a highly conserved 35-kD, microtubule tip-tracking protein, which is present in all eukaryotic organisms and all cell types (Tirnauer and Bierer 2000). EB1 directly binds to a structural motif on the growing end (plus-end) of microtubules and is known to stabilize and stimulate growth at the plus-end (Tirnauer and Bierer 2000, Rogers et al. 2002, Honnappa et al. 2009). EB1 also possesses a C-terminal homology domain, which controls the binding and activity of other MT-binding proteins including +TIPs, and hence, because of these regulatory functions, EB1 is speculated to be a master regulator of MT dynamics (Honnappa et al. 2009, Vaughan 2005). Cytoplasmic dynein is a minus-end directed motor protein, which mediate diverse cellular processes, such as intracellular transport of organelle, mRNA, and protein transport, centrosome assembly, and also help generate forces important for cell migration (Dujardin et al. 2003, Roberts et al. 2013). The cytoplasmic dynein is a large protein complex composed of two identical force generating heavy chains, dimerized intermediate chains and light intermediate chains interacting directly with the heavy chains, and three light chains interacting with the intermediate chains.

3.2 Materials & Methods

3.2.1 Cell culture

Human fibrosarcoma cells (HT1080) (ATCC, Manassas, VA) were grown in Dulbecco's modified Eagles Medium (Mediatech, Herndon, VA) supplemented with 10% fetal bovine serum (Hyclone Laboratories, Logan, UT) and 50 μg/ml gentamicin (Quality Biological, Gaithersburg, MD) as antibiotic. WI-38 cells were grown in Minimum Essential

Media (Mediatech, Herndon, VA) containing 10% fetal bovine serum (Hyclone Laboratories) and 100 U Penicillin/100 □ g streptomycin (Sigma-Aldrich, St. Louis, MO) per milliliter of media. For protein depletion, HT1080 cells were selected and maintained in medium containing 3 μg/ml puromycin. For culture and live-cell imaging, all cells were maintained in a humidified incubator at 37˚C and 5% carbon dioxide.

3.2.2 Depletion of EB1, LIC2, and HC1 proteins

shRNA constructs against target genes were co-transfected with the packaging plasmids pMD.G VSV-G and pCMVΔR8.91 using Lipofectamine 2000 (Life Technologies, Carlsbad, CA). Briefly, 293T cells were grown to ~90% confluency and a mixture of pMD.G VSV-G, pCMVΔR8.91, and shRNA construct in 1:8:6 ratio was added to the cells. 293T cells were then incubated with the mixture for 6 h and the transfection-mixture containing medium was replaced with fresh medium.

The lentivirus-containing medium was harvested twice at 24 h and 48 h post transfection and filtered through a 0.4□ m filter to remove cell debris. 2 ml of virus containing filtrate mixed with 1 ml of fresh medium and the polycationic peptide protamine sulfate (10□ g/ml final concentration) was added to ~60% confluent HT1080 cells and incubated for 8 hours. The medium containing the viral vectors was replaced with medium containing 3□ g/ml puromycin for selection. The medium was replaced every 3-4 days thereafter.

Five different shRNAs for each gene were tested and shRNAs showing at least 85% knockdown were used for subsequent studies. All the shRNAs used in this study were obtained from Sigma Aldrich. The shRNAs used for this study include:

EB1 sh62140 GCAGCAGGTCAACGTATTGAAC,

EB1 sh62142 GTTCAGTGGTTCAAGAAGTTTC,

LIC2 sh116993 CCTCGACTTGTTGTATAAGTAC,

LIC2 sh116996 GAAAGCCAGACTCTATGGTAAC,

HC1 sh116323 CCCGTGATTGATGCAGATAAAC,

HC1 sh116324 GCAGCCAATGACAAGCTGAAAC.

We used a scrambled shRNA sequence CCTAAGGTTAAGTCGCCCTCGC (Addgene plasmid 1864) as a control.

The level of protein depletion was confirmed by western blotting. The blots were incubated at 4˚C with the following antibodies: mouse anti-human EB1 (1:1000, Cell Signaling), rabbit anti-human LIC2 (1:1000, kindly provided by Richard Vallee, Columbia University, NY), rabbit anti-human HC1 (1:500, Proteintech, Chicago, IL). Beta-actin levels (1:2500, Santa Cruz Biotechnology, Dallas, TX) in the cell were used as controls.

3.2.3 Immunofluorescence microscopy

To visualize the localization of EB1 and LIC2 in 2D cultures, cells were plated on collagen I coated 35-mm glass bottom dishes. After 16 hours, the cells were fixed with 3% paraformaldehyde for 10 minutes, permeabilized with 0.01% Triton X-100 for 10 minutes, and blocked with 1% bovine serum albumin (BSA) for 1 h at room temperature. The cells were then stained for nuclear DNA (Hoechst 33342, 0.02 mg/ml), LIC2 (1:1000, kindly provided by Richard Vallee, Columbia University, NY), and EB1 (1:1000, Cell Signaling), and actin (Phalloidin, 1:40, Life technologies). Fluorescent images for cells on 2D substrates were collected using a Cascade 1K CCD camera (Roper Scientific) mounted on a TE2000 microscope with a 60X oil immersion lens.

For cells embedded in 3D collagen I matrices, the incubation times for fixation and permeabilization were doubled to 20 minutes. Cells were then blocked with 1% BSA for 2 h at room temperature. α-tubulin antibody (1:500, Abcam) antibody was then added to the

collagen I matrix and incubated at 4˚C overnight. The next day, the gel was washed 3X with PBS with 5 minute between washes and incubated with mouse anti-human α tubulin (1:200, Invitrogen), Phalloidin (1:40, Invitrogen), and Hoechst 33342 (0.02 μg/ml) for 2 hours. Lastly, the collagen I gel was washed 3X with PBS and stored in PBS at 4˚C. Imaging of matrix embedded cells was performed using Nikon A1 confocal microscope.

3.2.4 Embedding cells in 3D collagen I matrix and cell migration

As described previously, 2mg/ml type I collagen gels were used for this study (Fraley et al. 2010b). After trypsinization, 18,000 cells were mixed in 1:1 ratio of cell culture media and reconstitution buffer (0.2M 4-(2-hydroxyethyl)-1-piperazineethanesulfonic acid (HEPES) (Sigma-Aldrich, St. Louis, MO), 0.26M sodium bicarbonate ($NaHCO_3$) (Sigma-Aldrich, St. Louis, MO), and water as solvent) and appropriate amount of rat-tail collagen I (BD biosciences) was added to get final concentration of 2 mg/ml. Collagen I is solubilized in acetic acid, so the acid was quickly neutralized by adding a calculated amount of 1N NaOH. Next, 500μl of this final mixture was added per well of a 24 well dish and the dish was incubated in a humidified incubator maintained at 37˚C and 5% carbon dioxide. Fresh medium was added to the plate 2 hours later and the dish was put back in the incubator overnight.

24 hours later, images of cells were taken every two minutes for 16.5 hours using ORCA-AG 1K CCD camera (Hamamatsu Photonics) mounted on a Nikon TE 2000 microscope base. Single cells were tracked using template match algorithm in Metamorph imaging software. X- and Y- coordinates of cells obtained using Metamorph were processed using a MATLAB program to compute mean square displacements of cells using the following equation: $MSD = \langle [x(t + \Delta t)-x(t)]^2 + [y(t + \Delta t)-y(t)]^2 \rangle$.

3.2.5 Protrusion topology

Time-lapsed movies were used to systematically count the number of protrusions present in individual cells in 3D matrix. We characterized the protrusion into zeroth generation or mother protrusions, first-generation, and second-generation protrusions depending on their temporal location in the cell. Zeroth generation protrusions were the protrusions that started directly from the cell body (prolonging the nucleus) and they were the first to emerge from the cell. Protrusions stemming from the zeroth generation protrusions were termed first generation protrusions. Similarly, protrusions that stemmed from the first generation protrusions were termed second generation protrusions. Zeroth-generation, first-generation, and second-generation protrusions for all tested conditions were counted and contrasted to determine whether protrusion number correlated with cell migration.

3.2.6 Cell diffusivity and anisotropic index

As described in Chapter 4, we used APRW model to break down cell trajectory coordinates into primary and secondary direction of migration. Next, the persistent time and speed in the primary axis (P_p, S_p) and the secondary axis (P_s, S_s) were computed by fitting MSDs in the primary (MSD_p) and secondary axis (MSD_s), according to the equation,$MSD_p(\tau) = {S_p}^2{P_p}^2\left(e^{-\frac{\tau}{P_p}} + \frac{\tau}{P_p} - 1\right) + 2\sigma^2$ and

$MSD_s(\tau) = {S_s}^2{P_s}^2\left(e^{-\frac{\tau}{P_s}} + \frac{\tau}{P_s} - 1\right) + 2\sigma^2$, where τ represents time lag and σ^2 represents error in measurement of cell position. From these persistent time and speeds, we computed the diffusivity in the primary axis, $D_p = \frac{{S_p}^2 P_p}{4}$, and the secondary axis, $D_s = \frac{{S_s}^2 P_s}{4}$. Isotropic was calculated as the ratio of D_p over D_s.

3.2.7 Vesicle trafficking

VAMP3-EGFP (Addgene Plasmid 42310) and LAMP1-mCherry (Addgene Plasmid 45147) were transfected into HT1080 cells using Lipofectamine 2000 (Life technologies, Carlsbad, CA) according to product specifications. 6 h after transfection, transfection reagent containing media was replaced with fresh media. After 24 hours, cells were trypsinized and plated on glass bottom 24-well plates or embedded inside 3D collagen I gels as mentioned above. The next day (48 h post transfection), cells were imaged using a Nikon A1 confocal at 1 or 2 frames/s depending on the size of the scanned region. VAMP3-EGFP and LAMP1-mCherry dynamics were analyzed using the particle-tracking module in the u-track software package (Applegate et al. 2011, Jaqaman et al. 2008).

3.2.8 Statistics

Statistical analyses were performed using GraphPad Prism software. Mean ± SEM is shown unless otherwise stated. One-way ANOVA and t-test were performed wherever applicable to obtain statistical significance, which is shown in the graphs using Michelin grade scale ***$p<0.001$, **$p<0.01$, and *$p<0.05$.

3.3 Results

3.3.1 Microtubule dynamics, not microtubule stiffness, is required for cell translocation in a 3D matrix

Human fibrosarcoma cells (HT1080), a model system commonly used to study cell migration on 2D substrates and in 3D matrices (Wolf et al. 2003, Zhou et al. 2008, Wolf et al. 2007a, Sabeh, Shimizu-Hirota, and Weiss 2009) were either placed on 2D collagen I-coated substrates or fully embedded inside 3D collagen I matrices. We used collagen I as it is by far the most abundant extracellular-matrix protein in the stromal space near solid tumors (Kalluri and Zeisberg 2006, Shields et al. 2012) and in connective tissues where fibrosarcoma tumors develop and disperse (Asokan, Reddy, and Dhar 1993, Pluen et al. 2001, Netti et al. 2000). To determine whether microtubule integrity and dynamics could play a role in 3D cell

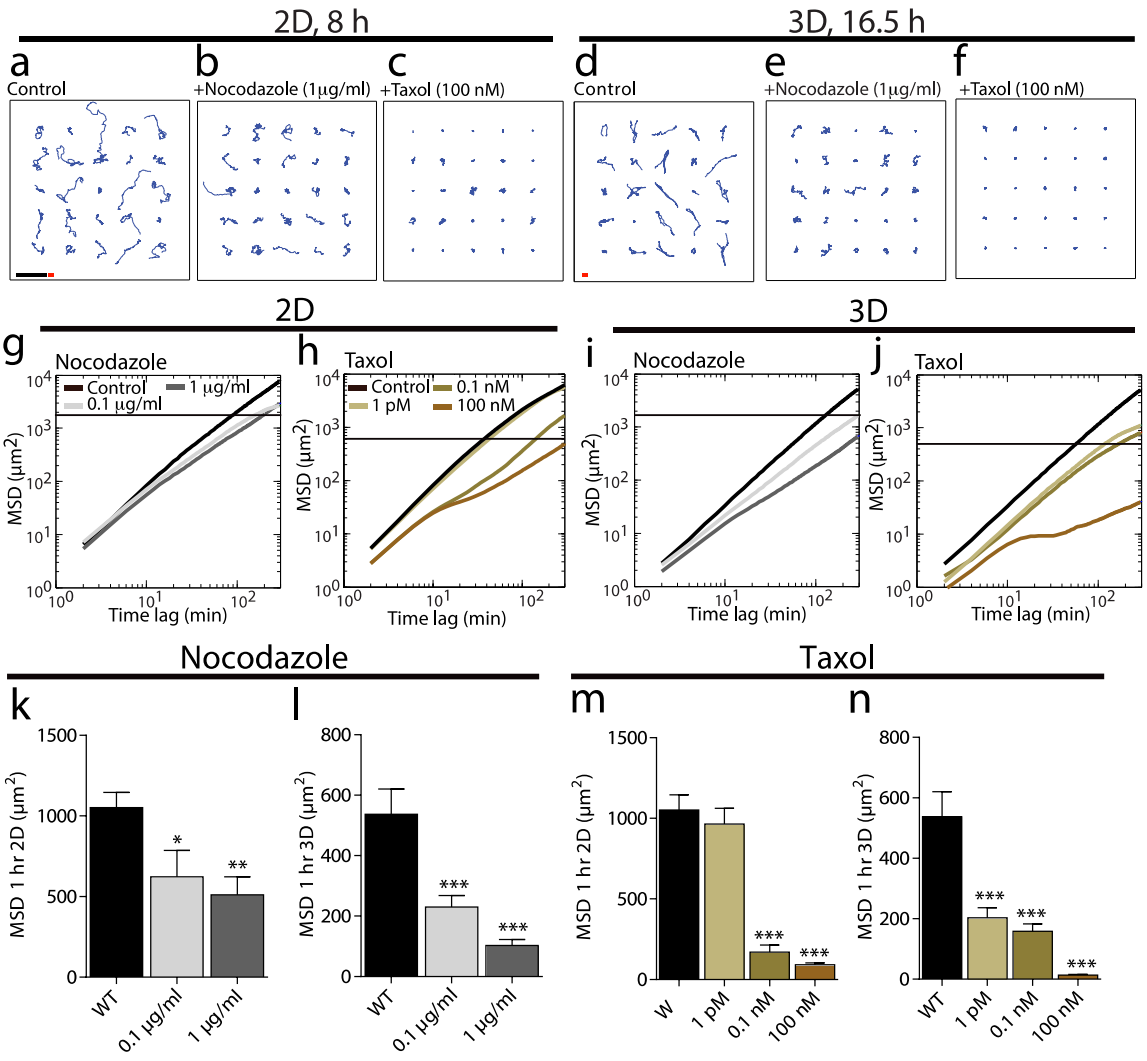

Figure 3-1. Microtubule dynamics mediates 3D cell migration.

A-F. Typical trajectories of 25 individual control HT-1080 cells and cells treated with microtubule-depolymerizing drug nocadozole and microtubule-stabilizing drug taxol, migrating on collagen I-coated 2D substrates and inside 3D collagen I matrices. Scale bar, 200 □ m. Red bars (bottom panels A and D) indicate the mean size of cells in 2D and 3D. **G and H.** Population-averaged mean squared displacements (MSDs) of control cells and cells treated with nocodazole (G) or taxol (H), migrating on 2D substrates. **I and J.** Population-averaged mean squared displacements (MSDs) of control cells and cells treated with nocodazole (I) or taxol (J), migrating inside 3D collagen I matrix. **K-N.** MSDs of nocodazole and taxol treated cells migrating on 2D substrates (K and M) and in 3D matrix (L and M) evaluated at time scales of 1 h. For all panels, ***:

Figure 3-1 (continued)

$p<0.001$, **: $p<0.01$, and *: $p<0.05$. For each condition, N = 3 biological repeats and at least 60 cells were probed.

migration, cells were first treated with microtubule-depolymerizing drug nocodazole and microtubule-stabilizing drug taxol.

Remarkably, despite a presumed reduced accessibility of the drugs to the cells in the matrix, we observed a much more significant attenuation of cell migration inside the matrix than for cells on 2D substrates when treated with the same concentration of nocodazole or taxol (Fig. 3-1, A-N). Trajectories of cells (x, y coordinates) were transformed into mean squared displacements (MSDs). On 2D substrates, the MSDs of nocodazole-treated cells at short time scales (e.g. evaluated at 4 min, Fig. 3-7, D) were comparable to that of control cells, while MSDs of taxol-treated cells were significantly lower compared to control cells (Fig. 3-7, F). On 2D substrates, MSDs at longer time scales (e.g. evaluated at 1h, Fig. 3-1, K and M) were reduced by 41% (0.1mg/ml) and 52% (1mg/ml) for nocodazole-treated cells and 8% (1pM), 84% (0.1nM), and 91% (100nM) for taxol-treated cells, compared to control cells. In 3D matrices, already at 4 min time-scale, the MSDs were reduced by 20% (0.1mg/ml) and 40% (4mg/ml) for nocodazole-treated cells and 56% (1pM), 57% (0.1nM), and 73% (100nM) for taxol-treated cells (Fig. 3-7, E and G). This strong effect of drug treatments of cells in 3D matrix was further enhanced at long time scales, i.e. by 57% (0.1mg/ml) and 81% (1mg/ml) for nocodazole-treated cells and 62% (1pM), 70% (0.1nM), and 97% (100nM) for taxol-treated cells (Fig. 3-1, L and N). A cell centroid can move over length scales smaller than the cell size, i.e. a cell may move without significant translocation. Therefore, we compared cell MSDs to the mean size of cells on 2D substrates and in 3D matrix (black horizontal lines in Fig. 3-1, G-J). We found that taxol treatment completely blocked cell migration in 3D matrix at 100 nM, i.e. there was no net cell translocation, even when evaluated at long time scales (Fig. 3-1H and Fig. 3-8 B). In contrast, taxol treatment reduced, but did not block, cell migration in 2D (Fig. 3-1G).

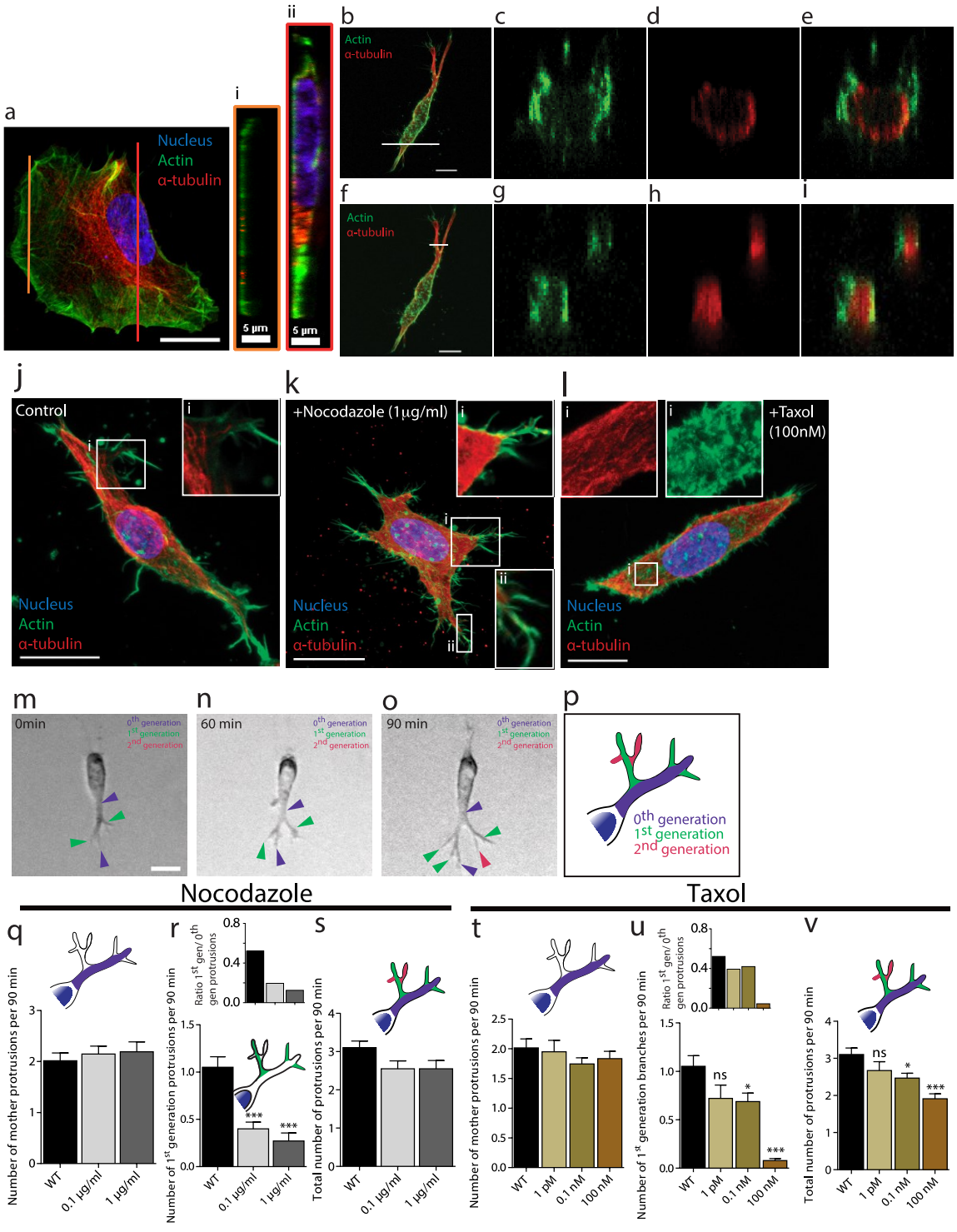

Figure 3-2. Microtubule dynamics promotes protrusion branching in 3D matrix.

A-I. Actin filament and microtubule organization in control HT1080 cells growing on 2D substrates (A) and inside 3D matrix (B-I). Cross-sections through the lamellipodium (Right panel 1i, Orange border) and the perinuclear cell body (Right panel 1ii, Red border). Cells were stained with DAPI (nuclear DNA) and

Figure 3-2 (continued)

antibodies against microtubule (red) and actin filament (green). J-L. Immunofluorescent images of control cells (J) and cells treated with nocodazole (K) and taxol (L) embedded in 3D collagen I matrices. *Insets:* daughter protrusions arising from the mother protrusions that prolong the nucleus are filled with microtubules in their lumen and F-actin at the periphery (Inset, J). Nocodazole treatment increases the number of filopodial-like protrusions (Inset, K), while taxol treatment gives rise to short, hairy actin protrusion throughout the cell (Inset, L). Cells were stained with DAPI (nuclear DNA) and antibodies against microtubule (red) and actin filament (green); images were obtained by immunofluorescence microscopy. Scale bar, 20 m. M-P. Active formation of pseudopodial protrusions by a cell embedded inside a 3D matrix (Purple arrowheads, 0^{th} generation or mother protrusions that stems directly from the cell body; Green arrowheads, 1^{st} generation protrusions that start from the 0^{th} generation protrusions; Magenta arrowheads, 2^{nd} generation protrusions that start from the 1^{st} generation protrusions). Schematic showing 0^{th}, 1^{st}, and 2^{nd} generation protrusions in a cell (P). Q-V. Total number of mother protrusions (0^{th}-generation protrusions) generated per 90 min per cell in nocodazole and taxol treated cells (Q and T). Number of first-generation protrusions generated per 90 min per cell (R and U). *Insets*: number of first-generation protrusions per mother protrusion (degree of branching) (Inset, R and U). Total number of protrusions generated per 90 min per cell (S and V). For panels, cells were monitored for 16.5 h. ***: $p<0.001$, **: $p<0.01$, and *: $p<0.05$. For each condition, N = 3 and at least 40 cells were probed for protrusion topology analysis.

Together these results demonstrate that microtubule dynamics play a critical role in controlling cell speed in the pathologically relevant case of a 3D matrix, significantly more so than in the conventional 2D case. Counter-intuitively, taxol treatment of fibrosarcoma cells is significantly more effective at blocking migration in 3D matrix than on 2D substrates.

3.3.2 Cells in 3D matrix form dendritic protrusions made of an inner ring of microtubules and outer ring of F-actin

To begin to determine why nocodazole and taxol treatments were more potent in 3D than in 2D environments, we assessed the morphology and the organization of microtubules and actin filaments for cells in 3D matrix and on substrates. Rather than a fan-shaped morphology with a wide lamellipodium and thin terminal filopodial protrusions at the leading edge of cells on 2D substrates (Fig. 3-2 A), cells embedded in 3D matrix displayed highly branched, dendritic protrusions (Fig. 3-2, B and J) (see also (Giri et al. 2013)). These branched protrusions contained both microtubules and actin (Fig. 3-2, B-I). Cross-sections through the perinuclear cell body and through protrusions far from the nucleus of cells in matrix both showed circumferential arrangement of F-actin and microtubule bundles, with actin filaments forming an outer ring and microtubules forming an inner ring or core (Fig. 3-2 B-I). Thick protrusions (e.g. Fig. 3-2, B-E) showed an inner lumen with little microtubule and actin stains in the center, and concentric rings of microtubules and F-actin. For thinner protrusions (e.g. 2-2, F-I), microtubules formed a core in the center of the protrusions with no lumen and an outer ring of F-actin. In contrast to the 3D case, the cross-section of lamellipodial protrusions in flattened cells on substrates typically showed no dense arrangement of microtubules in the lamellipodium (Fig. 3-2 A; profile i); rather higher microtubule density was observed in the perinuclear region in the direction of migration (Fig. 3-2 A; profile ii). Moreover, filopodia did not contain microtubules, as extensively

shown previously (Fig. 3-2 A). The high content of microtubules in protrusions of matrix-embedded cells (Fig. 3-2 B) compared to the low content in protrusions of cells on substrates (in the lamellipodium and filopodia; Fig. 3-2 A) is consistent with the much higher sensitivity of cells to microtubule drugs in the 3D case compared to the conventional 2D case (Fig. 3-1).

3.3.3 Microtubule dynamics mediates dendritic protrusions

Recent studies have shown a strong correlation between 3D cell migration speed and protrusion activity (defined here as the number of protrusions generated per unit time), not the length or lifetime of protrusions (Giri et al. 2013, Fraley et al. 2010b, Fraley et al. 2012). Therefore, we hypothesized and verified that pharmacological manipulation of microtubules using nocodazole and taxol would reduce protrusion activity since these treatments reduce cell speed in 3D matrices (Fig. 3-2, M-V).

Following the nomenclature introduced in (Giri et al. 2013), we refer as zeroth-generation protrusions or mother protrusions the pseudopodial protrusions directly prolonging the nucleus (Fig. 3-2, M-O, blue arrowheads). These zeroth-generation protrusions branched further into first-generation protrusions (Fig. 3-2, M-O, green arrowheads), which further branched into second-generation protrusions (Fig. 3-2, M-O, magenta arrowheads). The first-generation and second-generation protrusions are collectively referred to as daughter protrusions (green and magenta branches, Fig. 3-2 P; see Materials and Methods and (Giri et al. 2013) for more details about use of movies to determine the generation number of protrusions). We found that the formation of daughter protrusions was drastically reduced in both nocodazole- and taxol- treated cells (Fig. 3-2, R and U), while the number of mother protrusions was not significantly changed in these cells (Fig. 3-2, Q and T). In nocodazole-treated cells in 3D, the rates of formation of first-

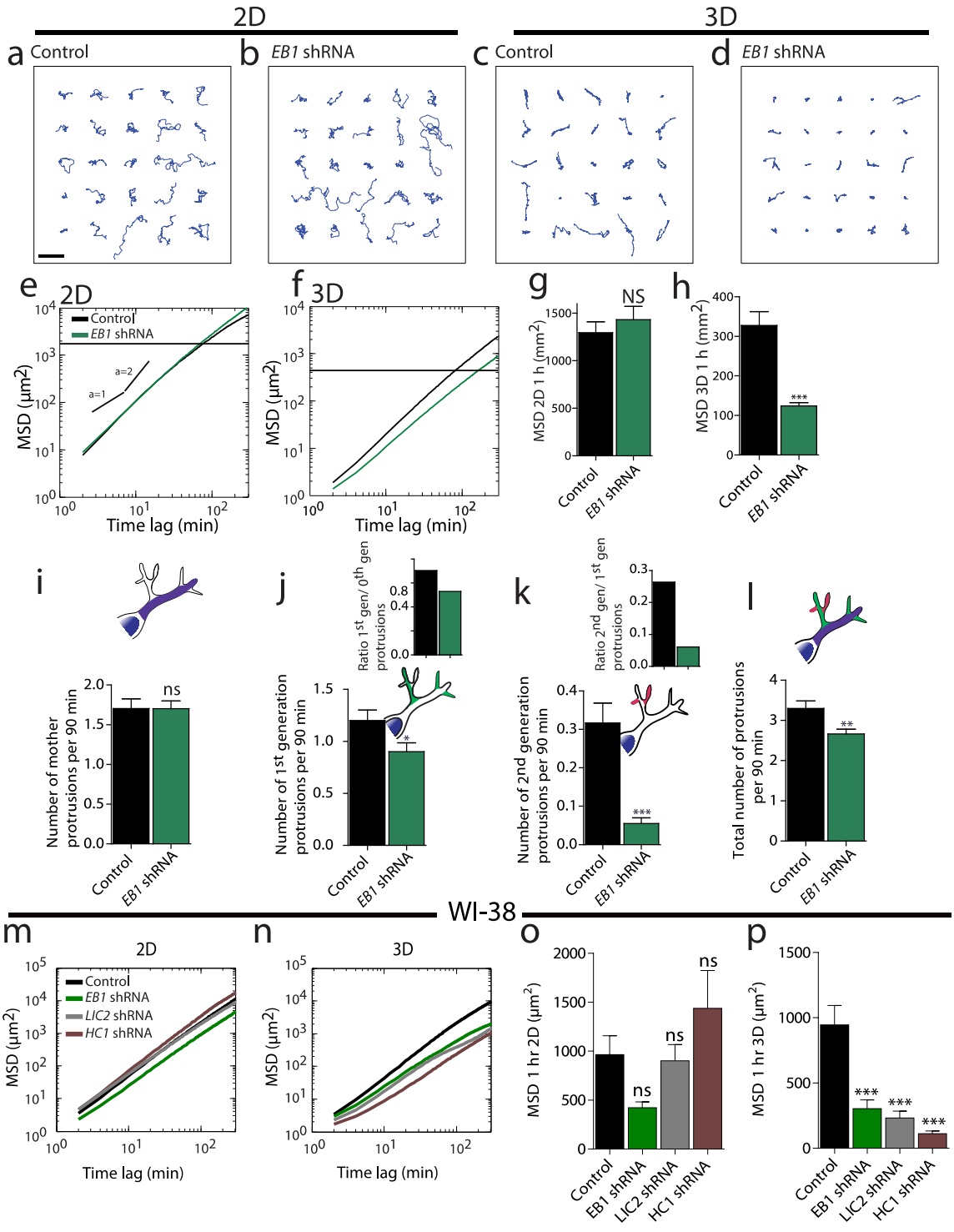

Figure 3-3. The distinct role of EB1 in 3D cell migration.

A-D. Typical trajectories of 25 individual control and EB1-depleted cells migrating on collagen I coated 2D substrates and inside 3D collagen I matrices. Scale bar, 200 □ m. **E and F.** shRNA-mediated depletion of EB1 has an inhibitory effect on cell migration in cells migrating in collagen I matrices (F) but no significant effect on

cell migration on substrates (E). **G-H.** Regulation of migration for cells on 2D substrates and embedded in 3D collagen I matrices by EB1. MSDs were evaluated at time scale of 1 h. **I.** Total number of mother protrusions (0^{th} generation protrusions) generated per 90 min per cell. **J and K.** Number of first-generation protrusions (J) and second-generation protrusions (K) generated per 90 min per cell. *Insets*: number of first-generation protrusions per mother protrusion (Inset, J), number of second-generation protrusions per first-generation protrusion (Inset, K). **L.** Total number of protrusions generated per 90 min per cell. For all panels, cells were monitored for 16.5 h. ***: $p<0.001$, **: $p<0.01$, and *: $p<0.05$. **M-N.** MSD plots for WI-38 cells depleted of EB1, LIC2, and HC1 moving on 2D substrates (M) and inside collagen I matrix (N). **O and P.** MSDs for WI-38 cells evaluated at a time scale of 1 h for cells on 2D substrates (O) and inside 3D matrix (P). For each condition, N = 3, at least 60 cells were probed for cell migration analysis, and at least 40 cells were probed for protrusion topology analysis.

generation protrusions decreased ~3-fold (0.1 μg/ml) and ~4-fold (1 μg/ml), while rates of formation of second-generation protrusions decreased 9-fold (0.1 μg/ml) and no second generation protrusions were detected at 1 μg/ml compared to control cells (Fig. 3-2 R and Fig. 3-8 A).

Similarly, in taxol-treated cells, the rates of formation of first-generation protrusions decreased ~1.5-fold (1 pM), ~1.5-fold (0.1 nM), and ~14-fold (100 nM), while rates of formation of second-generation protrusions decreased 1.36 fold (1 pM), 1.7-fold (0.1 nM), and no second-generation protrusion was detected at 100 nM compared to control cells (Fig. 3-2 U and Fig. 3-8 B). Accordingly, the degrees of protrusive branching off mother protrusions were drastically reduced in nocodazole- and taxol-treated cells (Insets, Fig. 3-2, R and U). We note that the treatment of cells with nocodazole and taxol increased somewhat the formation of short filopodia-like protrusions (Fig. 3-2, K and L), similar in length, thickness, and actin content as filopodia at the leading edge of cells on flat substrates, but distinct in morphology from microtubule-containing pseudopodial protrusions described above. Since these treatments abrogate cell motility in 3D, these small and thin protrusions do not seem to play a significant role in 3D migration.

Together our results suggest that microtubule dynamics promotes 3D cell migration by increasing the degree of branching of microtubule-filled protrusions presented by cells in 3D matrix, a type of protrusions that is completely absent from cells "flattened" by 2D substrates.

3.3.4 EB1 promotes 3D cell migration by mediating high protrusion activity and branching

Taxol treatment, which stabilizes microtubules, does not stabilize pseudopodial daughter protrusions, rather it eliminates them (Fig. 3-2). Hence, the above results suggest that microtubules do not play a structural role in 3D migration *per se*, but rather a regulatory role through its assembly/disassembly dynamics. To determine the mechanism by which microtubule dynamics induce effective cell migration in 3D matrix and modulate protrusion generation (Figs. 2-1 and 2-2), we asked whether disruption of microtubule dynamics by specific depletion of the major microtubule-tip binding protein EB1 (Fig. 3-7 A), which regulates microtubule stability at least for cells on 2D dishes (Tirnauer and Bierer 2000, Mimori-Kiyosue et al. 2005), would reduce 3D cell migration.

Visual inspection of trajectories of cells on substrates readily suggested that there was no qualitative difference in 2D migration between control cells (transfected with scrambled shRNA construct) and cells depleted of EB1 (Fig. 3-3, A and B). Indeed, the MSDs of EB1-depleted cells and control cells overlapped, both at short and long time scales (Fig. 3-3 E). The difference in MSD values between control and EB1-depleted cells on substrates were miniscule, both at both short (4 min) and long (1 h) time scales (Fig. 3-2, G). In contrast, EB1-depleted cells migrating inside 3D collagen I matrices had much tighter trajectories compared to control cells (Fig. 3-3, C, D, and F). In 3D matrices, MSDs at 4 min and 1 h were reduced by ~43% and ~62%, respectively, compared to control cells (Fig. 3-3H and Fig. 7 I). These results suggest that, while dispensable in 2D cell migration, the microtubule-tip binding protein EB1 is an integral component of 3D cell migration.

EB1 promotes 3D cell migration by mediating a high degree of protrusive branching of cells in 3D matrices (Fig. 3-3, I-L). Indeed, following EB1 depletion, the rates of formation of first- and second-generation protrusions decreased by ~31% and ~84% respectively, without affecting mother protrusions (Fig. 3-3, I- K). Accordingly, the degrees

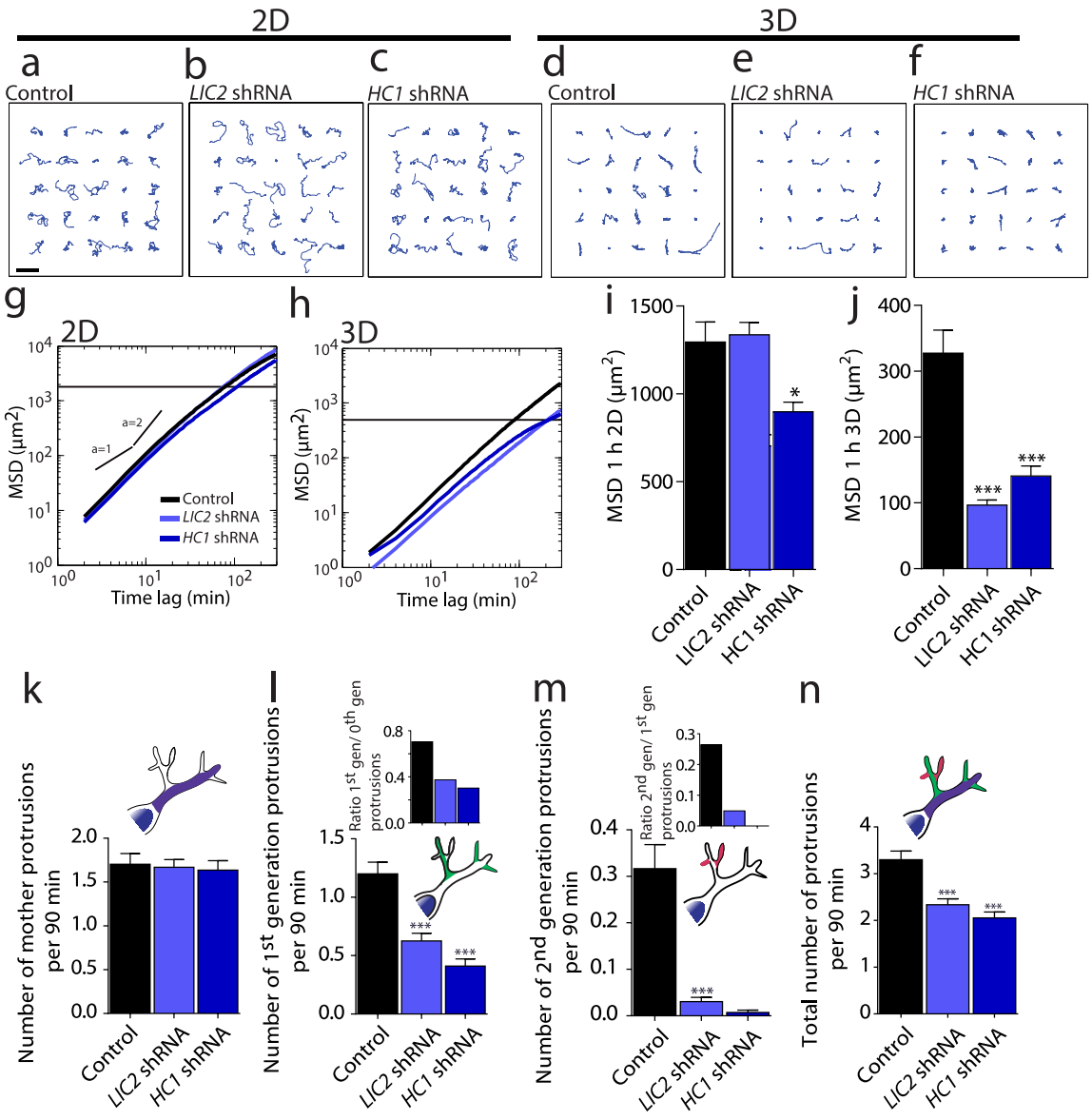

Figure 3-4. The distinct role of LIC2 and HC1 in 3D cell migration.

A-F. Typical trajectories of 25 individual control, LIC2-, and HC1-depleted cells migrating on collagen I coated 2D substrates and inside 3D collagen I matrices. Scale bar, 200 □ m. **G and H.** shRNA-mediated depletion of LIC2 has an inhibitory effect on cell migration in cells migrating in collagen I matrices (H) but no significant effect on cell migration on substrates (G). **I-J.** Regulation of migration for cells on 2D substrates (I) and in 3D collagen I matrices (J) by LIC2. MSDs were evaluated at time scale of 1 h (I and J). **K.** Total number of mother protrusions (0^{th} generation protrusions) generated per 90 min per cell. **L and M.** Number of first-generation protrusions (L) and second-generation protrusions (M) generated per 90 min per cell. *Insets*: number of first-

Figure 3-4 (continued)

generation protrusions per mother protrusion (Inset, L), number of second-generation protrusions per first-generation protrusion (Inset, M). **N.** Total number of protrusions generated per 90 min per cell. For all panels, cells were monitored for 16.5 h. ***: $p<0.001$, **: $p<0.01$, and *: $p<0.05$. For each condition, N = 3 and at least 60 cells were probed.

of protrusive branching off mother and first-generation protrusions were significantly reduced (Insets, Fig. 3-3, J and K).

In order to study if the effect of EB1 on 3D cell migration applied to other cell lines, we depleted EB1 in WI-38 cells, another widely used lung fibroblast cell line to study cell migration. Our results show that EB1 depletion did not significantly alter cell migration on 2D substrates (Fig. 3-3, M and O), but drastically reduced cell migration in 3D matrix (Fig. 3-3, N and P).

These results together suggest a new, 3D-specific role for EB1: EB1 is a major regulator of speed and persistence of 3D cell migration by promoting the formation of dendritic protrusions.

3.3.5 Cytoplasmic dynein (LIC2 and HC1) mediates 3D cell migration by promoting high protrusion activity and branching

EB1 plays a critical role in 3D cell migration, a role largely absent in 2D migration (at least for HT1080 and WI-38 cells); hence we asked if selective manipulation of other microtubule-binding proteins would have a similar selective effect in 3D cell migration. Protrusion generation, which is critical to 3D cell migration, could be modulated by microtubule-based mechanisms distinct from microtubule dynamics, such as vesicular trafficking. We studied the effect of the minus end-directed motor protein dynein. We created cell lines depleted of Light Intermediate Chain 2 (LIC2), a non-catalytic subunit of dynein, and Heavy Chain 1 (HC1), a catalytic subunit of dynein. Dynein is a motor protein involved in a variety of functions including membrane trafficking, MTOC positioning and cell division (Dujardin et al. 2003, Luxton and Gundersen 2011, Palmer, Hughes, and Stephens 2009), roles that have been determined *in vivo* or in 2D *in vitro* settings.

On 2D substrates, cells depleted of LIC2 (Fig. 7 B) migrated as rapidly as control cells (Fig. 3-4, A, B, G and I), while cells depleted of HC1 were slower than the control cells (Fig. 3-4, C, G, and I). However, when LIC2- and HC1-depleted cells were placed inside 3D collagen matrices, the trajectories of these cells were much tighter and their MSDs were much smaller compared to control cells (Fig. 3-4, D-F, H and J). To verify if cell migration was again mediated by changes in the number of daughter protrusions, we quantified the topology of the protrusions in LIC2- and HC1-depleted cells. LIC2- and HC1-depletion significantly reduced the number of daughter protrusions without changing the number of mother protrusions (Fig. 3-4, K-N). The rates of formation of first-generation protrusions for LIC2- and HC1-depleted cells decreased 2-fold and 3-fold, respectively (Fig. 3-4, N and O). The rates of formation of second-generation protrusions for LIC2- and HC1-depleted cells decreased 10-fold and 44-fold, respectively. Accordingly, the degree of branching of first-generation protrusions (off mother protrusions) and second-generation protrusions (off first-generation protrusions) was reduced in LIC2- and HC1-depleted cells compared to control cells (Insets, Fig. 3-4, L and M).

We verified the results of LIC2 and HC1 depletion using WI-38 cells. Depletion of LIC2 and HC1 domains of dynein had no effect on 2D cell migration (Fig. 3-3, M and O), while greatly reducing cell migration in 3D matrix (Fig. 3-3, N and P).

These results indicate that cytoplasmic dynein plays a much more significant role in 3D cell migration than in 2D migration by tightly regulating the degree of branching of 3D-specific dendritic protrusions.

3.3.6 EB1 and dynein mediate the directionality of cell migration inside 3D matrix

We have recently shown that cell migration in 3D matrix does not follow conventional random-walk statistics, but rather an anisotropic random walk (see Chapter 4).

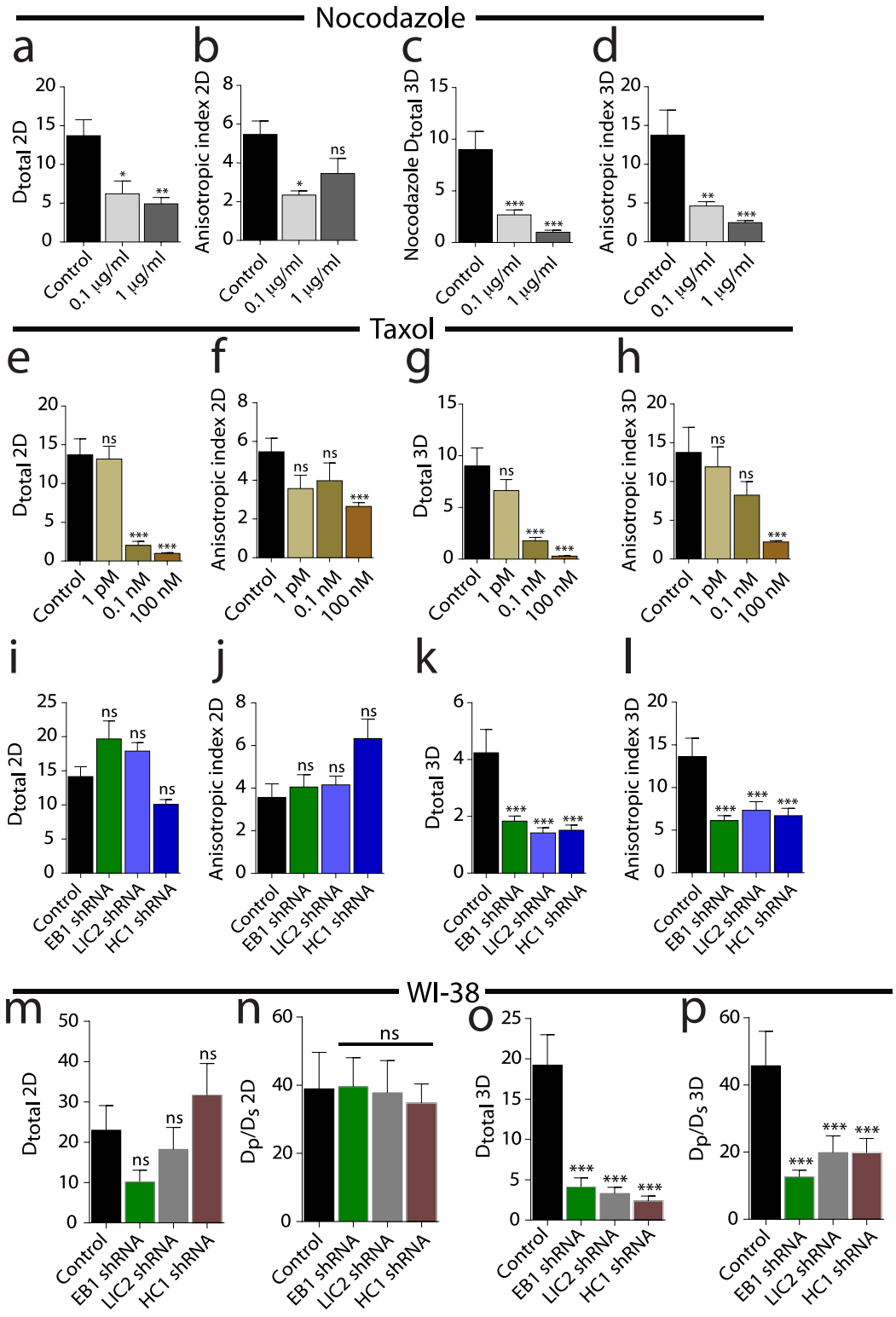

Figure 3-5. Cell migration in 3D matrix is anisotropic

A-D. Total diffusivity and anisotropic index for nocodazole treated cells on 2D (A and B) and in 3D matrix (C and D). **E-H.** Total diffusivity and anisotropic index for nocodazole treated cells on 2D (E and F) and in 3D matrix (G and H). **I-L.** Total diffusivity and anisotropic index for EB1, LIC2, and HC1 depleted cells on 2D (I and J) and in 3D matrix (K and L). **M-P.** Total diffusivity and anisotropic index for EB1, LIC2, and HC1 depleted WI-38 cells on 2D (M and N) and in 3D matrix (O and P).

In order to study if EB1 and dynein mediated not only the speed of migration, but also the directionality of cell migration, we fit experimental MSDs to the anisotropic persistent random walk (APRW) model introduced in Wu et al. This model decomposes cell velocities into primary and secondary directions of migration of individual cells and provides persistent time and speed along the primary axis (P_p, S_p) and the secondary axis (P_s, S_s) of migration. From these migratory descriptors, we computed the diffusivity along the primary axis (D_p) and secondary axis (D_s) as $D_p=S_p^2P_p/4$ and $D_s=S_s^2P_s/4$, respectively (Fig. 3-10, A-L); we also computed the anisotropic index, as the ratio of D_p over D_s, a quantity that measures directionality of migration.

On 2D substrates, nocodazole and taxol treatments caused a dose-dependent decrease in the total diffusivity ($D_{total}=D_p+D_s$) of cells in 3D matrix, which means that nocodazole- and taxol-treated cells migrated more slowly compared to control cells (Fig. 3-5, A and E). In 3D matrix, nocodazole and taxol treatment also caused a decrease in total diffusivity of the cells; however, the effects were much more pronounced compared to the 2D case (Fig. 3-5, C and G). On both 2D substrates and inside 3D matrix, the anisotropic index for nocodazole- and taxol-treated cells was smaller compared to the control cells, which implies that microtubules play a role in maintaining directional cell migration (Fig. 3-5, B, D, F, and H).

On 2D substrates, the total diffusivity of EB1-, LIC2-, and HC1-depleted cells were similar to that of control cells, while the diffusivity of these cells in 3D matrix were significantly smaller compared to control cells (Fig. 3-5, I and K). This result obtained from the APRW model fits is in agreement with the experimental MSD values (Fig. 3-3, G and H; Fig. 3-4, I and J). On 2D substrates, the anisotropic index for EB1-, LIC2-, and HC1-depleted cells were comparable to that of control cells, while for cells inside 3D matrices, the

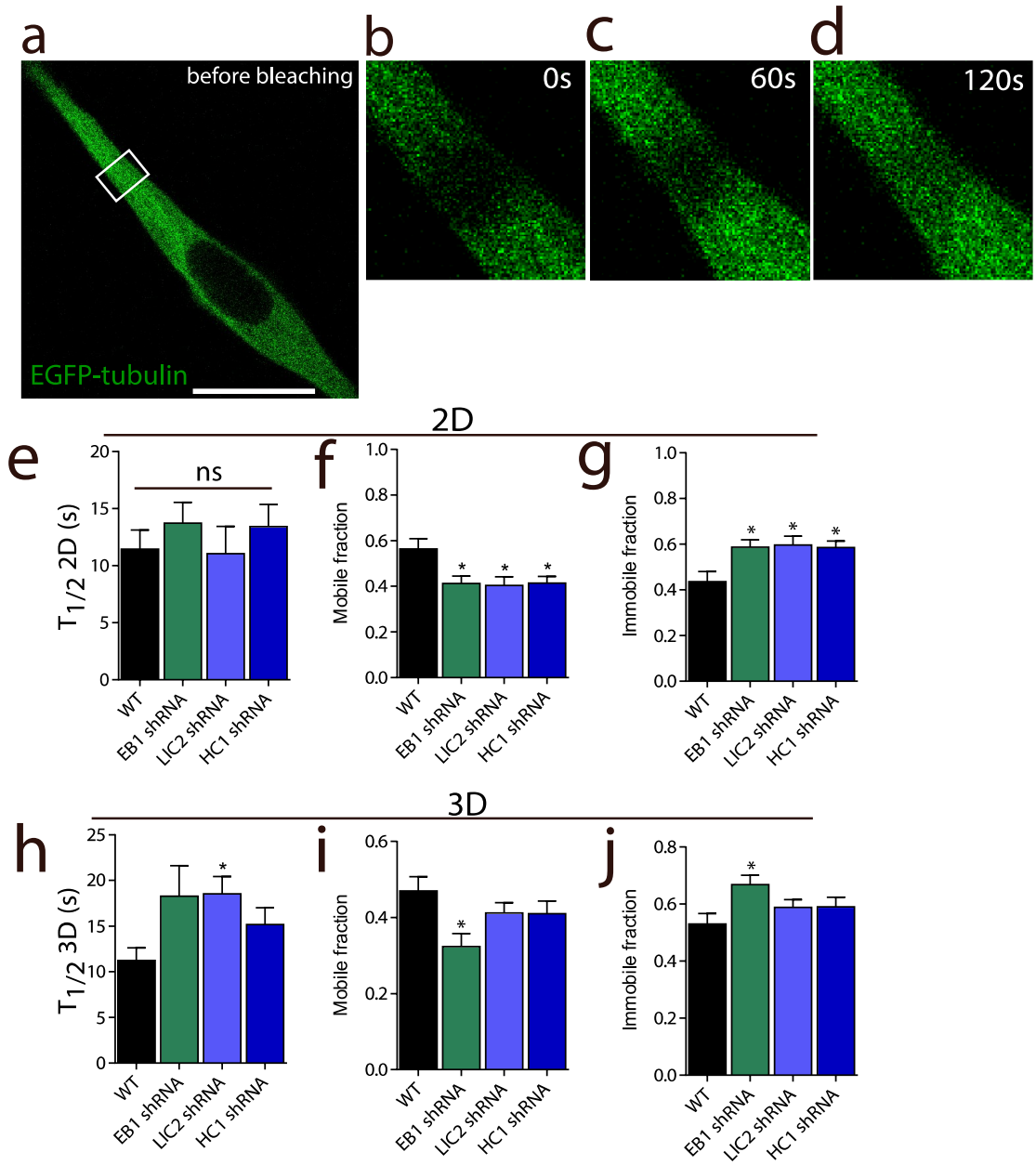

Figure 3-6. LIC2 and EB1 promote fast microtubule dynamics in pseudopodial protrusions of cells in 3D matrix.

A-D. FRAP images of cells embedded inside 3D collagen I matrices. Time of image acquisition is mentioned in the images. **E-J.** Half-life of fluorescence recovery, mobile fraction, and immobile fraction of □□ tubulin GFP for control, EB1-, LIC2- and HC1-depleted cells in 2D (E-G) and inside 3D matrix (H-J).

anisotropic index for EB1, LIC2, and HC1 depleted cells were reduced by 52%, 42%, and 47%, respectively.

Analysis of diffusivity and anisotropic index in WI-38 cells showed similar results. On 2D substrates, the total diffusivity and anisotropic index for EB1-, LIC2-, and HC1-depleted cells were not significantly different from control cells (Fig. 3-5, M and N). In 3D matrix, the D_{total} and anisotropic index for EB1-, LIC2-, and HC1-depleted cells were significantly reduced compared to control cells (Fig. 3-5, O and P).

3.3.7 EB1 and dynein promote 3D migration by inducing high microtubule dynamics in protrusions

Given the above results, we hypothesized that EB1 and, to a lesser extent, dynein regulated 3D migration by modulating microtubule dynamics. Microtubule dynamics was assessed by fluorescence recovery after bleaching (FRAP) of cells transfected with □-tubulin-EGFP (Tirnauer and Bierer 2000, Mimori-Kiyosue et al. 2005). FRAP analysis revealed that microtubule dynamics was much slower in matrix-embedded cells than in cells on substrates, as measured by a shorter halftime for recovery ($T_{1/2}$) and lower recovered fraction in control cells and cells depleted of LIC2 or EB1 (Fig. 3-9, A-J). While EB1 and dynein played a minor role in microtubule dynamics in HT1080 cells on 2D substrates (Fig. 3-9 E), EB1 and dynein promoted fast microtubule dynamics for cells in 3D matrix (Fig. 3-9 H).

Since microtubules and microtubule-associated proteins play a role in vesicular trafficking (at least for cells on 2D substrates) and such trafficking may modulate cell migration, we determined whether EB1 and dynein regulated vesicular trafficking along microtubules by transfecting live cells with VAMP3-EGFP and LAMP1-mcherry constructs (Gierke and Wittmann 2012). Using time-dependent confocal microscopy, we tracked the

speed of vesicles inside live cells and found that these proteins played no significant role in the trafficking of VAMP3 and LAMP1 tagged vesicles (Fig. 3-9, K-M).

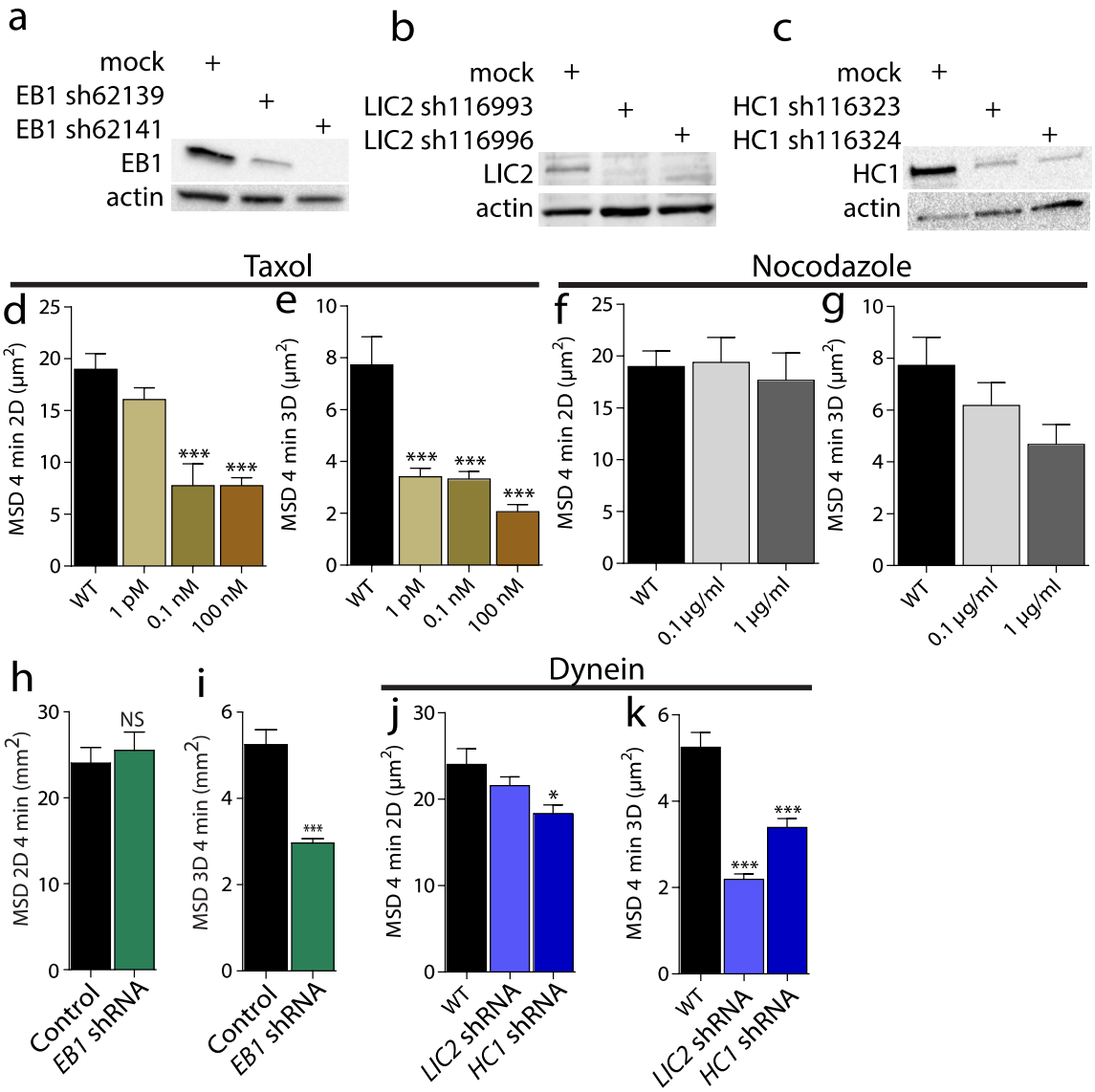

Figure 3-7. Western blots and mean square displacements of Taxol, Nocodazole, EB1-, LIC2-, and HC1-depleted cells

Western blots of control and cells depleted of EB1 (A), LIC2 (B), and HC1 (C). Two constructs were assessed per protein. **D and E.** Mean square displacements (MSDs) of taxol treated cells at a time lag of 4 min on 2D substrates (D) and in 3D matrix (E). **F and G.** MSDs of nocodazole treated cells at a time lag of 4 min on 2D substrates (F) and in 3D matrix (G). **H-K.** MSDs of EB1-, LIC2-, and HC1-depleted cells migrating on 2D (H and J) and in 3D matrix (I and K).

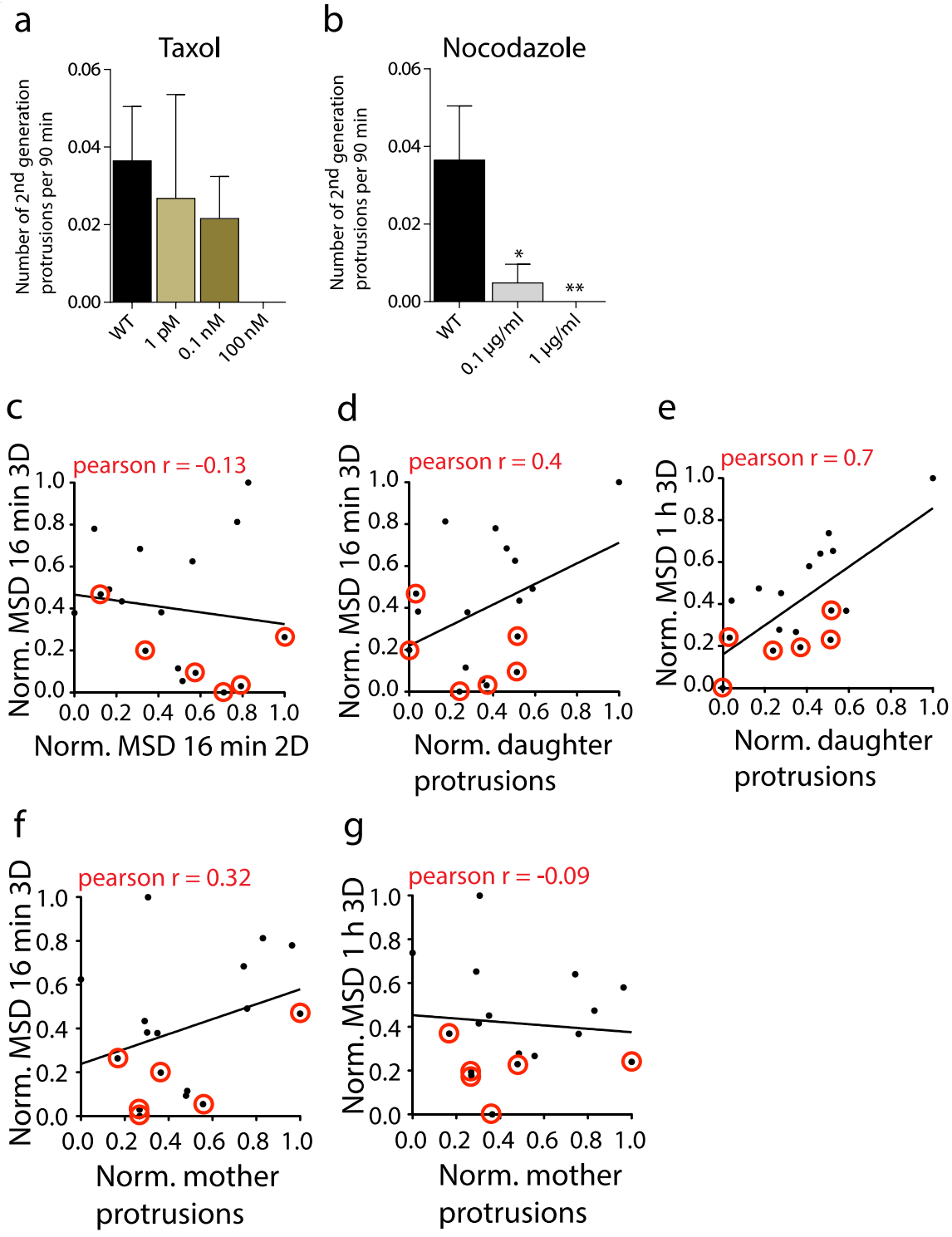

Figure 3-8. Daughter protrusions mediate cell motility in 3D matrix

A and B. Total number of second generation protrusions generated per cell per 90 min by Taxol (A) and Nocodazole (B) treated cells. **C-G.** Correlation analysis that indicates there is no correlation between cell

motility (measured as MSDs) in 2D and 3D environments (C), strong correlation between 3D cell motility and daughter protrusions (D and E), and no correlation between 3D cell motility and the number of mother protrusions (F and G). Circled data points are new data from this work; other data is taken from ref. (Giri et al. 2013, Fraley et al. 2010b, Fraley et al. 2012).

Together these results suggest that the mechanism by which EB1 and dynein mediate fast migration in 3D is by promoting fast microtubule dynamics in microtubule-rich pseudopodial dendritic protrusions that drive cell migration in 3D.

3.4 Discussion

Our results indicate that microtubule dynamics is more crucial to migration in the pathologically relevant case of 3D collagen matrices than on 2D collagen-coated substrates because the drivers of 3D cell migration – dendritic pseudopodial protrusions - are filled with dynamic microtubules that critically rely on microtubule-tip protein EB1 and microtubule-associated motor protein dynein (LIC2 and HC1) to branch out into the matrix. Microtubules can play structural and regulatory roles for effective 3D migration. Quantitative live-cell measurements show that microtubule turnover dynamics (FRAP results, Fig. 3-5, A-J) – not vesicular trafficking along microtubules (Fig. 3-9) and microtubule intrinsic stiffness (taxol results, Fig. 3-2 J) - account for the modulation of 3D cell migration by microtubules and associated proteins.

Microtubule stiffness could have played a structural role in protrusion formation since microtubules form thick bundles within protrusions (Fig. 3-2 J) that could help stabilize protrusions for effective 3D migration. Moreover, taxol treatment used here can increase the mechanical stiffness of microtubule polymers (Mickey and Howard 1995, Gittes et al. 1993). However, we observed that this taxol-induced increase in mechanical stability of microtubules did not stabilize protrusions for matrix-embedded cells. On the contrary, dendritic protrusions collapsed in taxol-treated cells, which effectively eliminated migration in 3D matrix. Therefore, this work suggests that microtubules themselves play no significant structural role in maintaining protrusions and migration in 3D matrix, at least in human

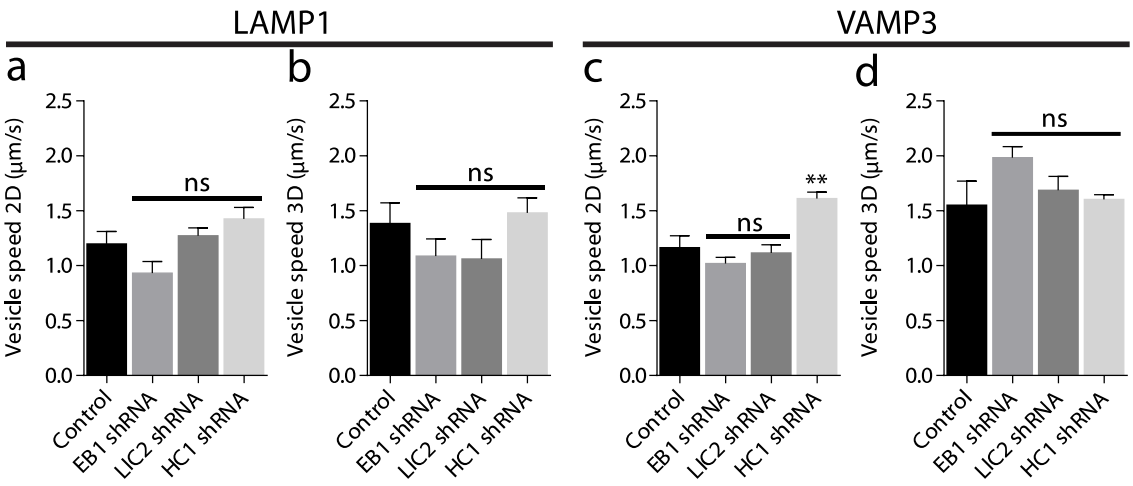

Figure 3-9. EB1, LIC2, and HC1 did not mediate vesicle trafficking speed

A and B. Speed of LAMP1-GFP tagged vesicles moving inside live cells growing on 2D substrates (A) or inside 3D collagen I matrix (B). **C and D.** Persistence of vesicle movement defined as displacement divided by total length of cells growing on 2D substrates (C) and inside 3D matrix (D).

fibrosarcoma cells and fibroblasts, but rather play a critical regulatory role through EB1/LIC2/HC1-mediated dynamics.

This and recent work (Giri et al. 2013, Fraley et al. 2010b, Fraley et al. 2012) indicate that mother protrusions that prolong the nucleus and daughter protrusions that dendritically grow from them are regulated by distinct families of molecules. The degree of branching from mother protrusions (i.e. number of daughter protrusions per mother protrusions) is specifically regulated by microtubule dynamics through microtubule-associated proteins EB1 and dynein (LIC2 and HC1) (Fig. 3-3, I-L and Fig. 3-4, K-N). These proteins are part of an increasing family of proteins that specifically regulate branching off mother protrusions. In addition to EB1 and dynein, the degree of branching from mother protrusions is also specifically regulated by focal adhesion proteins and F-actin regulators VASP and zyxin (Giri et al. 2013), F-actin nucleator Arp2/3 complex, Arp2/3-complex regulators/activators N-Wasp, Cortactin, Wave 1, and small GTPase Cdc42 (Giri et al. 2013). These proteins do not mediate the formation of mother protrusions.

In contrast, the formation of mother protrusions is specifically regulated by focal adhesion proteins FAK, talin, and p130Cas (Giri et al. 2013): these proteins do not modulate side branching from mother protrusion. Finally, myosin II-based contractility (Giri et al. 2013) and small GTPase Rac1 (Fraley et al. 2012) regulate both mother protrusions and their degree of branching, and regulate cell migration. Hence, results in this paper add to the increasing body of evidence that only molecular mediators of protrusive branching regulate 3D cell migration. The degree of branching from mother protrusions – not the ability of cells to form mother protrusions themselves *per se* – faithfully predicts cell speed in 3D matrices (see global correlations in Fig. 3-8, A-E). As indicated by the present results, these dendritic protrusions have to be dynamic – dynamically branching out into the collagen

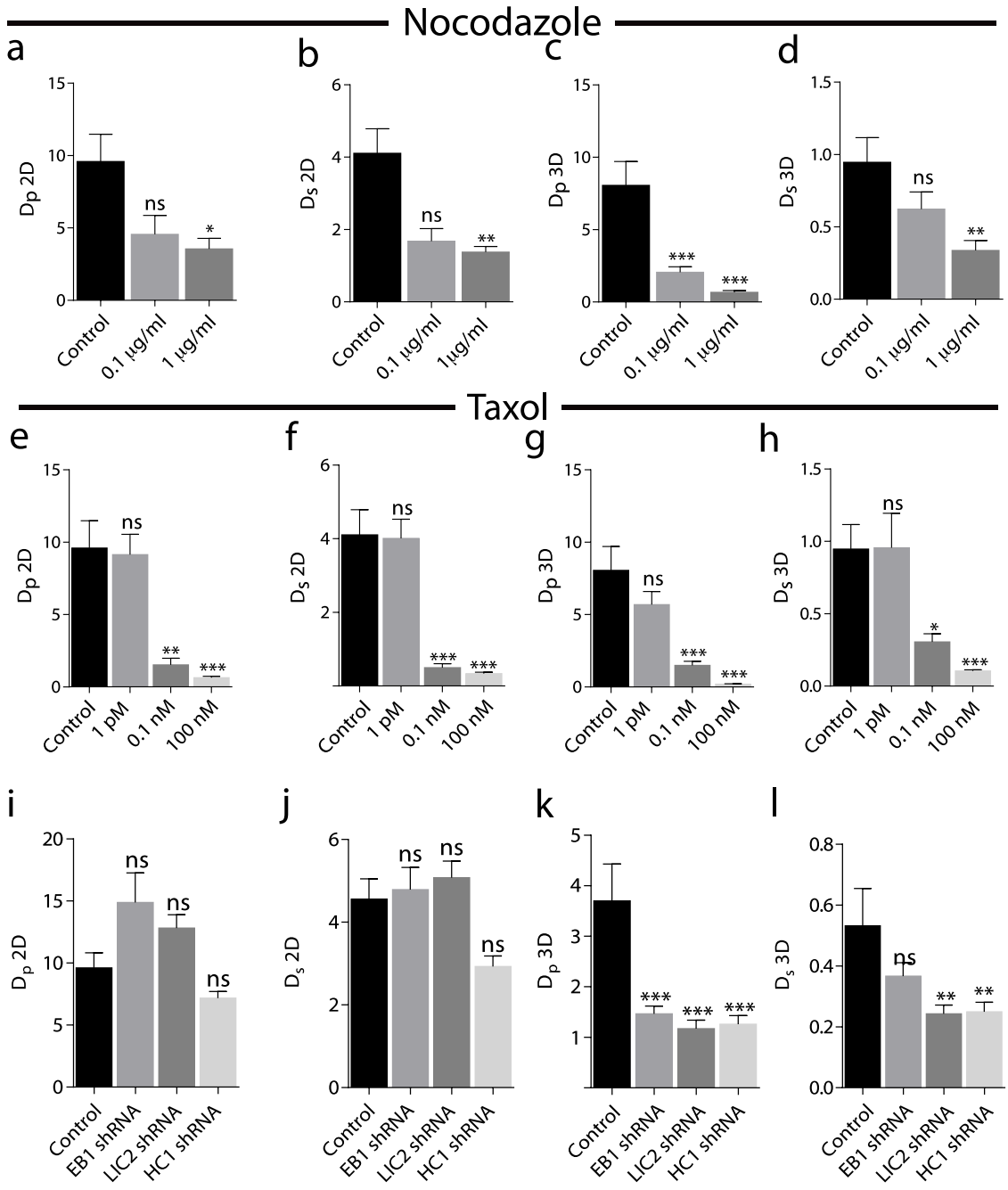

Figure 3-10. Diffusivity of cells on 2D substrates and in 3D matrix

Diffusivity of the cells treated with nocodazole in the primary and secondary axis of migration on 2D (A and B) and in 3D matrix (C and D). **E-H.** Diffusivity of the cells treated with taxol in the primary and secondary axis of migration on 2D (E and F) and in 3D matrix (G and H). **I-L.** Diffusivity of the Control, EB1-, LIC2-, and HC1- depleted cells in the primary and secondary axis of migration on 2D (I and J) and in 3D matrix (K and L).

matrix and then retracting towards the body of the protrusions - in order to contribute to 3D cell migration.

The dominant role of microtubule assembly dynamics in 3D migration compared to limited role in conventional 2D migration may be due in part to the confinement forces onto the cell created by the dense collagen matrix. Recent work (Balzer et al. 2012) has shown that, at doses that block cell migration in wide channels, cells confined to microfabricated microchannels of lateral size similar or smaller to the nuclear size are often insensitive to pharmacological treatments that reduce actin assembly or inhibit myosin-based contractility. In contrast, the migration of these confined cells is completely blocked by treatments targeting microtubule dynamics (Balzer et al. 2012). Hence, the central role of microtubules in the migration of cancer cells in 3D matrices may be part due to the confinement that these matrices impact on the cells.

Another important aspect that our study highlights is the dimensionality of cell migration on 2D substrates and in 3D matrix: 3D cell migration is highly polarized compared to 2D cell migration (Fig. 3-5). This result can have important implications in understanding cancer metastasis, where cancer cells traverse the 3D extracellular matrix before establishing secondary tumors. In this context, it is not far fetched to imagine that having a polarized trajectory or not may be a dictating factor for cancer metastasis. There is a plethora of molecules that have been known to play a role in cell migration and it's often difficult to identify potent candidates to study cancer metastasis. This study can help us narrow down molecules that may play a role in metastasis *in vivo* by characterizing molecules based on speed and the degree of polarized migration.

As previously shown for a large number of focal adhesion proteins (zyxin, VASP, talin, FAK, vinculin, paxillin, p130Cas (Fraley et al. 2010b, Fraley et al. 2012)) and for the

Arp2/3 complex and associated proteins (Cortactin, Cdc42, Wave 1, N-Wasp (Giri et al. 2013)), and now demonstrated for microtubule dynamics and associated regulators, the speed of cells on collagen-coated flat substrates poorly predicts the speed of these cells in a 3D collagen matrix. Results in this paper suggest that one of the main reasons for this lack of functional relationship between 2D and 3D migration is that the major cytoskeletal filaments F-actin and microtubules are organized in matrix-embedded cells fundamentally differently from their 2D counterparts (Fig. 3-2 A *vs*. Fig. 3-2, B-I). Actin filaments and microtubules form concentric rings of bundles oriented along the long axis of the protrusions, with F-actin forming the outer ring (presumably thanks to membrane-binding proteins, such as members of the ERM family of proteins) and microtubules forming the inner ring. Strikingly, inside protrusions, F-actin and microtubule barely mix (Fig. 3-2, E and I), yet form a relatively tight interface. Indeed, in thick protrusions, the inner ring of microtubules is favorably connected to the outer ring of F-actin rather than filling up the core of the protrusions (Fig. 3-2 E). The mutual, spatial exclusion of microtubules and actin filaments within a cell seems to be a common occurrence in many biological systems (Rodriguez et al. 2003). For instance, during fertilization of the *C. elegans* embryo, the introduction of sperm-derived microtubules breaks down and repels the actin-rich cortex of the embryo to trigger asymmetric cell division (Cowan and Hyman 2004). Hence, our results constitute another example of such a spatial mutual exclusion, here of critical importance to 3D cell migration.

A possible clinical consequence of our results is that the microtubule-stabilizing drug paclitaxel (taxol), commonly used for tumor shrinkage in wide range of human cancers (e.g. paclitaxel treatment is standard of care for breast, ovarian cancer, and fibroblastic tumors), is significantly more effective at arresting cell migration in 3D matrix than on 2D substrates.

This opens the possibility to develop and test additional drugs that target microtubule dynamics in 3D collagen constructs instead of conventional 2D dishes to potentially predict efficacy and specificity to treat metastatic disease in cancer.

CHAPTER 4

Three-dimensional cell migration does not follow a random walk

4.1 Introduction

Random walks are ubiquitous in biology (Berg 1993). In particular, the motility of bacteria and eukaryotic cells in the absence of symmetry-breaking gradients has long been described in terms of random-walk statistics. Eukaryotic cell migration is a complex process that is a tightly regulated and critical to the normal development of organs and tissues (Pollard and Borisy 2003b, Lauffenburger and Horwitz 1996, Ridley et al. 2003). Cell migration is activated in a wide range of human diseases, including cancer metastasis (Jin and Varner 2004, Wirtz, Konstantopoulos, and Searson 2011a) and immunological responses (Luster, Alon, and von Andrian 2005), and wound healing (Martin 1997). Most of what we know about eukaryotic cell migration at a mechanistic molecular level has stemmed from well-controlled studies of cell migration on flat dishes (i.e. 2D environment). However, cell migration *in vivo* often forces cells to remodel, exert pulling forces on, and move through a 3D collagen I-rich matrix. Recent work has demonstrated that mechanisms of 3D migration are often different from their 2D counterparts (Fraley et al. 2010c, Fraley et al. 2012, Giri et al. 2013, Tang et al. 2013, Yu and Machesky 2012, Zaman et al. 2006, Khatau et al. 2012). Migration on 2D dishes, which induces a basal-apical polarization of the cell, is driven by actomyosin contractility of stress fibers between large focal adhesions and the formation of a

wide lamellipodium terminated by thin filopodial protrusions at the leading cellular edge (Ridley et al. 2003, Kim and Wirtz 2013). The same cells in collagen-rich 3D matrix do not display a lamellipodium or filopodia. Instead, they display highly dendritic pseudopodial protrusions controlled by distinct proteins that rely both on acto-myosin contractility and microtubule assembly/disassembly dynamics (Giri et al. 2013, Friedl et al. 2012a). Three-dimensional cell migration depends on the expression of metalloproteinases (MMPs), which are dispensable in 2D migration, and physical properties of the 3D matrix (Bloom et al. 2008), such as pore size (Wirtz, Konstantopoulos, and Searson 2011a). Recent work has also shown how cancer cells in 3D can alternate between a mesenchymal and an amoeboid migratory phenotype depending on the physical properties of the matrix (Czirok et al. 1998, Wolf et al. 2013) and MMP inhibition (Friedl et al. 2012a), phenomena that do not occur in the 2D case. Finally, through the zyxin/□-actinin/p130Cas module, 3D cancer cell migration features tight molecular control of the temporal and spatial patterns of movements in the matrix, which do not exist in conventional 2D migration (Fraley et al. 2012).

Yet, despite these important differences, cell speed and persistence of migration in 2D and 3D microenvironments are typically extracted from fits of the mean squared displacements (MSDs) using the same persistence random walk (PRW) model (Tranquillo, Lauffenburger, and Zigmond 1988b, Tranquillo and Lauffenburger 1987b, Stokes, Lauffenburger, and Williams 1991b, Stokes and Lauffenburger 1991b, Parkhurst and Saltzman 1992). Fits of MSDs, however, do not rigorously test several key underlying assumptions of the PRW model, including a Gaussian distribution of velocities, a single-exponential decay of the velocity correlation function, an isotropic velocity field, and a flat distribution of angles between cell movements at long time scales (Berg 1993). This paper shows that incorporating cell heterogeneity into the PRW model is sufficient to fully explain

statistical descriptors of 2D migration. In contrast, we show that the assumptions of the PRW model are quantitatively and qualitatively erroneous for 3D cell migration: cancer cell migration in 3D matrix does not follow a random walk. We introduce and validate a new model of 3D cell migration that takes into account cell heterogeneity and the anisotropic movements induced by local remodeling of the 3D matrix.

4.2 Materials & Methods

4.2.1 Cell culture

Human fibrosarcoma cells (HT1080) (ATCC, Manassas, VA) were grown in Dulbecco's modified Eagles Medium (Life technologies, Grand Island, NY) supplemented with 10% fetal bovine serum (Hyclone Laboratories, Logan, UT) and 0.001% gentamicin (Quality Biological, Gaithersburg, MD). Cells were maintained in a humidified incubator at 37°C and 5% carbon dioxide.

4.2.2 Embedding cells in 3D collagen I matrix

HT1080 cells were embedded in gels of controlled type-I collagen density, as described previously (Fraley et al. 2010b). Briefly, 18,000 cells suspended in 1:1 (v/v) ratio of cell culture medium and reconstitution buffer (0.2M 4-(2-hydroxyethyl)-1-piperazineethanesulfonic acid (HEPES) (Sigma-Aldrich, St. Louis, MO), 0.26M sodium bicarbonate ($NaHCO_3$) (Sigma-Aldrich), and water as solvent) were mixed with appropriate volume of soluble rat-tail collagen I (BD Biosciences, Franklin Lakes, NJ) to obtain the desired target collagen concentration. A calculated amount of 1M NaOH was added quickly and the final solution was mixed well to bring the pH to ~7. The cells suspension was added to a 24-well coverslip-bottom cell-culture dish and immediately transferred to an incubator maintained at 37°C to allow polymerization. This cell density was chosen so as to minimize cell collisions. Fresh medium was added 5 h before imaging.

4.2.3 Cell tracking

A Nikon TE2000 microscope with a phase contrast 10-X objective (Nikon, Melville, NY) was used to image the motility of living cells through a CCD camera (Hamamatsu, Hamamatsu, Japan). A cell incubator (Pathology Devices, Westminster, MD) was used to maintain temperature and humidity of cells while on the microscope. Images were collected every 2 min for >8 h. For cells embedded in 3D collagen matrices, the focus plane was at least 200 μm away from the bottom of plates to diminish edge effects (Fraley et al. 2010a). The Metamorph (Molecular Devices, Sunnyvale, CA) software was used to track the time-dependent centroids of individual cells. We developed and used two additional methods of tracking cells to ensure that the results were independent of the method of cell tracking (see Supplementary Information).

4.2.4 Statistical profiling of cell trajectories

The time-dependent coordinates [$x(t)$, $y(t)$] of the centroids of individual cells were first transformed into mean-squared displacements, MSDs, as

$$MSD(\tau) = < [x(t+\tau) - x(t)]^2 + [y(t+\tau) - y(t)]^2 >,$$

where τ represents the time lag and $< \cdots >$ indicates time-averaging. Time-averaging in the computation of the MSD is justified because the instantaneous speed (distance travelled by cells divided by 2 min) was found to be time-invariant over 8h (Fig. 4-1). The auto correlation function (ACF) of cell velocity was calculated from the cell displacements at the smallest time lag dt (=2min) using $dx(t) = x(t+dt) - x(t)$ and $dy(t) = y(t+dt) - y(t)$. The ACF is calculated using the following formula:

$$ACF(\tau) = < dx(t)dx(t+\tau) + dy(t)dy(t+\tau) > .$$

Since the $ACF(\tau)$ is corrupted by noise at the shortest time scales (see Fig. 4-11 and Fig. 4-8), only $ACFs$ at time lags larger than $2dt$ were evaluated. The ACF was normalized by its value at $2dt$ (=4 min).

The angular displacements $d\theta$ between two subsequent displacements of a cell were calculated using the following equation:

$$d\theta(t,\tau) = \arccos[(v_t \cdot v_{t+\tau})/|v_t||v_{t+\tau}|] .$$

where v_t is the vector represents movement of cell from time t to time $t+\tau$ and $v_{t+\tau}$ is the vector of displacement of cell from $t+\tau$ to $t+2\tau$.

To determine the long axis for each of migratory trajectories of individual cells, the singular vector decomposition (SVD) was applied to the velocity matrix of individual cells ($\overline{\overline{M}}$), i.e.

$$M = U\lambda V^*.$$

Here U is the matrix of eigenvectors of the product MM^*, $V^*$is the matrix of eigenvectors of the product M^*M, λ are the singular values of the matrix M, and * denotes the transposed matrix. The first and the second eigenvectors of V^* correspond to the primary migration axis ($\vec{p}$) and non-primary migration axis ($\overrightarrow{np}$), respectively.

4.2.5 Characterizing the PRW model

Some level of noise always corrupts assessment of cell location, including the imaging noise and the noise from the fluctuating positions of the cell stemming from dynamically changing cell shapes. Taking into account the observation noise (Wu et al. 2009), the measured 2D MSD for the PRW model becomes

$$MSD_{2D}(\tau) = 2S^2P^2\left(e^{-\frac{\tau}{P}} + \frac{\tau}{P} - 1\right) + 4\sigma^2.$$

Here, σ^2 is the variance of observation noise in cell position. The persistence time and cell speed were obtained from fitting the measured MSD profiles to this last relation through the non-linear least squared fit method. We only used the first one-third of total time points of a MSD profile for model fitting since the resolution of individual MSD profile progressively deteriorates for increasing time lags due to limited sampling size (Qian, Sheetz, and Elson 1991). Further, a weight function, equal to the product of the inverse of MSD value and errors in MSD due to limited sample size (Qian, Sheetz, and Elson 1991), was assigned in the fits to prevent the model fits from over-emphasizing fitting errors of MSD values at large time lags where the resolution is poor but values are large. From the fit, the cell diffusivity, *D*, was calculated as $D= S^2P/2$. This parameter represents diffusion profiles at time lags much larger than the persistent time, where cell motility follows free diffusion.

4.2.6 The APRW model

In the APRW model, cell motility is assumed to display different persistence and diffusivity along two orthogonal axes, the primary migration axis and non-primary migration axis, in the observation 2D plane. The velocities of a cell along the primary ($\vec{p}$) and non-primary ($\overrightarrow{np}$) axes of migration are governed by two Langevin equations:

$$\frac{dv_p}{dt} = -\frac{1}{P_p}v_p + \frac{S_p}{\sqrt{P_p}}\tilde{w}$$

$$\frac{dv_{np}}{dt} = -\frac{1}{P_{np}}v_s + \frac{S_{np}}{\sqrt{P_{np}}}\tilde{w}.$$

The corresponding MSDs along the $\vec{p}$ and $\overrightarrow{np}$ axes are:

$$MSD_p(\tau) = {S_p}^2{P_p}^2\left(e^{-\frac{\tau}{P_p}} + \frac{\tau}{P_p} - 1\right) + 2\sigma^2 \text{ and}$$

$$MSD_s(\tau) = {S_{np}}^2{P_{np}}^2\left(e^{-\frac{\tau}{P_{np}}} + \frac{\tau}{P_{np}} - 1\right) + 2\sigma^2.$$

Therefore, the total MSD of a cell is

$$MSD_{2D}(\tau) = {S_p}^2 {P_p}^2 \left(e^{-\frac{\tau}{P_p}} + \frac{\tau}{P_p} - 1 \right) + {S_{np}}^2 {P_{np}}^2 \left(e^{-\frac{\tau}{P_{np}}} + \frac{\tau}{P_{np}} - 1 \right) + 4\sigma^2.$$

The 2D cell diffusivity of the APRW model, D_{tot}, was calculated as $D_{tot} = ({S_p}^2 P_p + {S_{np}}^2 P_{np})/4$ and the diffusivity contributed from only the primary migration direction, D_P, was calculated as $D_P = ({S_p}^2 P_p)/4$.

To identify the characteristics of the APRW model from the experimental observed MSD, the primary and non-primary axes were first identified using the SVD (see text). The coordinates of cell trajectories (R) in the observation plane were then rotated using the rotational matrix V^*, i.e. $R_{rot} = R \cdot V^*$, so that the movement along the P and S axes of R become the x and y axes of R_{rot}. Hence, the MSD along the primary migration direction, MSD_p, and non-primary migration direction, MSD_{np}, can be computed easily.

After rotation, the x-direction becomes the primary migration direction and y-direction becomes the non-primary migration direction. Hence, the MSD profile along the x-direction is MSD_p and along the y-direction is MSD_{np}. Persistence and speed at theses two axes can be obtained from model fitting to these two MSDs. The anisotropic index, Φ, in the APRW model is defined as the ratio between the cell diffusivities along the primary and non-primary migration axes, i.e.

$$\Phi \equiv \frac{D_P}{D_{np}} = \frac{{S_p}^2 P_p}{{S_{np}}^2 P_{np}}.$$

4.2.7 Computer simulations of cell trajectories

For the PRW model of cell migration with given a set of persistent time P, speed S, and variance of observation error σ^2, the cell trajectories are simulated based on the following method. The propagation of the cell position is given by:

$$x(t+dt) = x(t) + dx(t, dt)$$

$$y(t+dt) = y(t) + dy(t, dt).$$

Here, dx and dy are the displacements of the cell position in *x* and *y* axis over time period of dt.

The cell displacement propagation over time using the following equations,

$$dx(t, dt) = \alpha \cdot dx(t - dt, dt) + F \cdot W$$

$$dy(t, dt) = \alpha \cdot dy(t - dt, dt) + F \cdot W,$$

where $\alpha = 1 - \frac{dt}{P}$, and $F = \sqrt{\frac{S^2 dt^3}{P}}$. In these simulations, the time step size dt is chosen to be a hundred times smaller than the observation time step size and is 0.02 min. Positioning noises are further added to the simulated trajectories to mimic the experimental observation using the following equations,

$$\hat{x}(t) = x(t) + \sigma \cdot W$$

$$\hat{y}(t) = y(t) + \sigma \cdot W,$$

where $W \sim N(0,1)$ is white noise.

For simulating the cell trajectories of APRW model, we follow an approach similar to that for the PRW model but have different propagation of displacement since persistence and diffusivity along the *x* and *y* -direction is not the same. With given set parameters of P_p, P_{np}, S_p, S_{np} and σ^2 of APRW model, the propagation of cell displacements is formulated using following equations:

$$dx(t, dt) = \alpha_p \cdot dx(t - dt, dt) + F_p \cdot W$$

$$dy(t, dt) = \alpha_{np} \cdot dy(t - dt, dt) + F_{np} \cdot W.$$

Here,

$$\alpha_p = 1 - \frac{dt}{P_p}$$

$$\alpha_{np} = 1 - \frac{dt}{P_{np}}$$

$$F_P = \sqrt{\frac{{S_p}^2 dt^3}{P_p}}$$

$$F_{np} = \sqrt{\frac{{S_{np}}^2 dt^3}{P_{np}}}$$

Each of simulated trajectories is than rotated by an angle which is randomly picked between 0 and 2π to randomize orientations of trajectories.

4.2.8 Analysis of angular displacements for the PRW model

Applying finite difference analysis to PRW model we get

$\frac{(v(t+\Delta t)-v(t))}{\Delta t} = -\frac{1}{p}v(t) + \frac{S}{\sqrt{P}}\widetilde{w}$

$\big(v(t + \Delta t) - v(t)\big) = -\frac{1}{p}v(t)\Delta t + \int_t^{t+\Delta t} \frac{S}{\sqrt{P}}\widetilde{w}(t)\, dt$

Since integration of Weiner process can be computed as

$\int_t^{t+\Delta t} \frac{S}{\sqrt{P}}\widetilde{w}(t)\, dt = \sqrt{\frac{S^2}{P}\Delta t} \cdot W$,

where W is a white noise with zero mean and unit variance. We then obtain

$v(t + \Delta t) - v(t) = -\frac{1}{p}v(t)\Delta t + \sqrt{\frac{S^2}{P}\Delta t} \cdot W$.

Hence velocity propagation over time can be obtained as

$$v(t+\Delta t) = (1-\frac{\Delta t}{p})v(t) + \sqrt{\frac{S^2}{P}\Delta t}\cdot W$$

Further, the cell velocity is approximated by

$$v(t) = \frac{dx}{dt} = \frac{x(t+\Delta t)-x(t)}{\Delta t}$$

And hence,

$$v(t+\Delta t) = \frac{x(t+2\Delta t)-x(t+\Delta t)}{\Delta t}$$

After rearrangement of equation for velocity time propagation over time, we obtain

$$\frac{x(t+2\Delta t)-x(t+\Delta t)}{\Delta t} = \left(1-\frac{\Delta t}{p}\right)\cdot\frac{x(t+\Delta t)-x(t)}{\Delta t} + \sqrt{\frac{S^2}{P}\Delta t}\cdot W$$

Replacing $x(t+\Delta t)-x(t)$ with the displacement, $dx(t)$, we obtain the relation of displacement propagate over time

$$dx(t+\Delta t) = \left(1-\frac{\Delta t}{p}\right)\cdot dx(t) + \sqrt{\frac{S^2}{P}\Delta t^3}\cdot W$$

This equation shows the displacement at a given time point is approximately composed of two components, including memory effect and random fluctuation effect.

Therefore, when Δt is small, $(t+\Delta t) \cong dx(t)$, and hence the angular displacement ($d\theta$) will be approximate 0. For large Δt, memory effect of displacement is negligible, i.e. $dx(t+\Delta t)$=$\sqrt{\frac{S^2}{P}\Delta t^3}\cdot W$, and hence the $dx(t+\Delta t)$ is independent of $dx(t)$, i.e. $< dx(t+\Delta t)\cdot dx(t) >$ =0. Therefore the probably density function of angular displacement between subsequent randomly-oriented displacements is the uniform distribution over angles [- π-π].

4.2.9 Statistical profiles of motility are independent of the cell-tracking method

In this work, cell motility is tracked using the commercial software Metamorph. To test whether the measured statistical profiles of cell motility, such as exponential-like probably density function of cell displacements, are not an artifact of the implemented tracking method, we used two additional methods to measure cell motility.

The first method consists in tracking the centroid of GFP-labeled cells by time-lapsed fluorescence microscopy using the following procedure. We first blurred the fluorescent images of cells by applying a Gaussian blurring filter to the original image. The standard deviation used to generate the Gaussian blurring filter was 11 pixels in size, which was chosen manually to optimize tracking outcomes. After the Gaussian blurring process, the intensity distribution of a cell became radically distributed from the center of cell body. The brightest location in the cell body was then extracted and defined as the centroid of a cell.

The second method is similar to the first method but using time-lapsed phase-contrast microscopy. Here, the raw images were first convolved with at standard deviation filter using a window size of 21. The filter was intended to transform contrast part (cell body) of phase images into positive intensity signals. The Gaussian blurring filter was then implemented on these images to extract the time-dependent centroid location of cells.

The movements of the same ten cells on 2D substrates were tracked by these three methods and statistical profiles of cell motility were computed and compared (Fig. 4-7). Our results showed that the statistical profiles of cells measured by these three different methods, including MSDs, ACF, probably density function of angular displacements, probably density function of cell displacements, and velocity profiles along principal orientations, were in good agreement with each other. In particular, for all three different methods of cell tracking, the distributions of displacement still demonstrated an exponential-like behavior.

Together, these results suggest that the measured statistical profiles of cell motility presented in the body of the paper are not an artifact of our tracking methods.

4.2.10 Effects of observation noise on the estimation of velocity correlation

The "true" position of a cell at time *t* is denoted as $x(t)$. However, the observation position, $\hat{x}(t)$, of a cell is obstructed with an observation noise, ε_x. Therefore,

$$\hat{x}(t) = x(t) + \varepsilon_x(t)$$

$$\varepsilon_x \sim N(0, {\sigma_x}^2)$$

The observation noise is described by a normal distribution with zero mean and standard deviation of σ_x, i.e.

$$\langle \varepsilon_x \rangle = 0$$

$$\langle \varepsilon_x \cdot \varepsilon_x \rangle = {\sigma_x}^2$$

Therefore, the displacement at time *t* with time lag τ, can be calculated from the observed positions as

$$d\hat{x}(t, \tau)$$

$$= \hat{x}(t + \tau) - \hat{x}(t)$$

$$= x(t + \tau) + \varepsilon_x(t + \tau) - x(t) - \varepsilon_x(t)$$

$$= dx(t, \tau) + (\varepsilon_x(t + \tau) - \varepsilon_x(t))$$

Similarly, the displacement at any other time point, $t + N\tau$ is

$$d\hat{x}(t + N\tau, \tau)$$

$$= \hat{x}(t + (N + 1)\tau) - \hat{x}(t + N\tau))$$

$$= x(t + (N + 1)\tau) + \varepsilon_x(t + (N + 1)\tau) - x(t + N\tau) - \varepsilon_x(t + N\tau)$$

$$= dx(t + N\tau, \tau) + (\varepsilon_x(t + (N + 1)\tau) - \varepsilon_x(t + N\tau))$$

Here, N is an integer ranging from 1 to the total number of observation times (N_{tot}).

Therefore, the auto-correlation function, $\hat{C}(N)$, resulting from the observed cell displacements can be derived as

$$\hat{C}(N)$$

$$=< d\hat{x}(t,\tau) \cdot d\hat{x}(t + N \cdot \tau, \tau) >$$

$$=< \Big(dx(t,\tau) + \big(\varepsilon_x(t+\tau) - \varepsilon_x(t)\big)\Big)$$

$$\cdot \Big(dx(t + N\tau, \tau) + \big(\varepsilon_x(t + (N+1)\tau) - \varepsilon_x(t + N\tau)\big)\Big) >$$

Since $\langle dx(t,\tau) \cdot \varepsilon_x \rangle$=0, and $\langle \varepsilon_x(t1) \cdot \varepsilon_x(t2) \rangle = 0 \; if \; t1 \neq t2$, then

$$\hat{C}(N)$$

$$=< dx(t,\tau) \cdot dx(t + N\tau, \tau) + \varepsilon_x(t+\tau)\varepsilon_x(t + (N+1)\tau) + \varepsilon_x(t)\varepsilon_x(t + N\tau)$$

$$- \varepsilon_x(t)\varepsilon_x(t + (N+1)\tau) - \varepsilon_x(t+\tau)\varepsilon_x(t + N\tau) >$$

$$=< C(N) + \varepsilon_x(t+\tau)\varepsilon_x(t + (N+1)\tau) + \varepsilon_x(t)\varepsilon_x(t + N\tau) - \varepsilon_x(t)\varepsilon_x(t + (N+1)\tau)$$

$$- \varepsilon_x(t+\tau)\varepsilon_x(t + N\tau) >$$

For N > 0, $\hat{C}(N)$ can further be simplified as

$$\hat{C}(N) =< C(N) > -< \varepsilon_x(t+\tau)\varepsilon_x(t + N\tau) >$$

Thus,

$$\hat{C}(N) = C(N) - {\sigma_x}^2 \qquad for \; N = 1$$

$$\hat{C}(N) = C(N) \qquad for \; N > 1$$

Therefore, the position error in the observed trajectories cause the underestimation of the autocorrelation function at the smallest time lags with the difference of size of variance of position noise. This conclusion agrees with the experimental observation (Fig. S5) where the value of $\hat{C}(1)$ is smaller than value of $\hat{C}(2)$.

4.2.11 Statistics

Mean values, standard error of measurement (SEM), and statistical analysis were calculated and plotted using MATLAB (Mathworks, Natick, MA). Spearman's rank correlation coefficient was used to assess the association between motility parameters. Two-tailed unpaired *t* tests and ANOVA tests were conducted to determine significance, which was indicated using standard Michelin Guide scale (*** for $P < 0.001$, ** for $P < 0.01$, and * for $P < 0.05$).

4.3 Results

4.3.1 The persistence random walk (PRW) model

The PRW model of cell motility is derived from a stochastic differential equation describing the motion of a self-propelled cell:

$$\frac{dv}{dt} = -\frac{1}{P}v + \frac{S}{\sqrt{P}}\widetilde{W}, \quad \text{(Eq. 1)}$$

where t is time, v is the cell velocity, P is the persistent time, S is the cell speed, and $\widetilde{W}$ is the random vector of a Wiener process (Stokes, Lauffenburger, and Williams 1991b). A main characteristic of this model is that the MSD is given by

$$MSD(\tau) = nS^2P^2\left(e^{-\frac{\tau}{P}} + \frac{\tau}{P} - 1\right) \quad \text{(Eq. 2)},$$

where n is the dimension of the extracellular space (which can be 1D, 2D, and 3D) (Konstantopoulos, Wu, and Wirtz 2013, Fraley et al. 2012, Friedl et al. 2012b, Chang et al. 2013) and τ is the time lag between positions of the cell. The autocorrelation function of the cell velocity vector for the PRW model exhibits a single exponential decay:

$$\langle v(\tau)v(0)\rangle = \frac{nD}{P}e^{-\frac{\tau}{P}}. \quad \text{(Eq. 3)}$$

In 2D, the velocity direction is described by an angle with respect to a lab frame, θ. The change in angle over a small time interval, $d\theta$, is a random variable given by an uniform

distribution with a peak near d□□□□□ Typically, Eq. 2 is used to fit measured MSD data. The statistics of d□□ and the time-lag-dependence of the velocity autocorrelation function (Eq. 3) are generally not examined in details.

4.3.2 A rigorous test of the PRW model of cell migration

Using live-cell microscopy, we measured the spontaneous displacements of individual, low-density, human, wild-type fibrosarcoma HT1080 cells – a cell model used extensively in cell migration studies – on 2D collagen-coated substrates and inside 2mg/ml collagen matrices in the absence of symmetry-breaking directional (chemotactic, galvanotactic, durotactic, etc.) gradients. Type I collagen was chosen because it is by far the most abundant protein of the extracellular matrix in fibrous connective tissues from which malignant mesenchymal tumors are derived and disseminate (Wirtz, Konstantopoulos, and Searson 2011a). Cell movements were recorded at a rate of 30 frames per hour for > 8 h, corresponding to ~2.5 decades in time scales (Fig. 4-1, A and B). Trajectories of cells in 2D and 3D conditions readily showed distinct patterns (Fig. 4-1 B). The trajectories of cell migration in 3D displayed a more linear morphology compared to trajectories of cells in 2D conditions. Importantly, we verified that the instantaneous speed of cells (averaged distance traveled every 2 min) was independent of time over the entire observation time period, which indicated that cells displayed a steady motility behavior both in the 2D and 3D cases (Fig. 4-1, C and D). Cells displayed a significant lower speed in 3D matrices than cells on 2D flat substrates at both short time scale (□ =2 min) and long time scale (□ =60 min) (Fig. 4-1e). Accordingly, the MSDs of cells on 2D substrates were significantly higher than of cells in 3D matrices at any given time lag between 2 min and 8 h, indicating that 2D cell motility is faster than 3D cell motility (Fig. 4-2 F). At short time scales (□□ < 1 h), both MSD profiles in 2D

and 3D displayed an exponent □ > 1 (measured from a fit of MSD ~ □□), indicating that cell motility was directional (super-diffusive) (Fig. 4-1 F).

The persistent random walk model (PRW) was introduced close to 30 years ago and has been used ubiquitously to describe and analyse the random migration of cells on substrates (Tranquillo, Lauffenburger, and Zigmond 1988b, Tranquillo and Lauffenburger 1987b, Stokes, Lauffenburger, and Williams 1991b, Stokes and Lauffenburger 1991b) and, more recently, cell migration in 3D matrices (Parkhurst and Saltzman 1992). The MSD for the PRW model is given in Eq. 2. If we include the observational error in the measurements, the MSD is then given by:

$$MSD(\tau) = 2P^2S^2\left(\frac{\tau}{P} - 1 + \exp\left(-\frac{\tau}{P}\right)\right) + 4\sigma^2. \quad \text{(Eq. 4)}$$

Here, $4\sigma^2$ is the noise (error) in the position of the cell (see Methods for details). The PRW model provides an overall good fit to MSDs of individual cells (R-squared value: 0.88-0.98) for both 2D and 3D migration. This model also seemed to perfectly describe cell MSDs at the cell-population level in both 2D and 3D environments (R-squared value: ~ 1) (Fig. 4-1 F). Therefore, one could conclude that the PRW model explains 2D and 3D cell migration.

However, the PRW model has a number of underlying assumptions, such as a Gaussian distribution of velocity at all time scales, exponential decay for the autocorrelation correlation function, and isotropic cell movements. There is a practical challenge to test these assumptions for individual cells: the inherently limited resolution of measuring these statistical profiles at the single-cell level. Indeed, the resolution is mainly determined by the sample size of measured cell velocities, which is naturally restricted by two intrinsic limits: (1) the sampling rate and (2) the observation time. The limited sampling rate is due to the fact

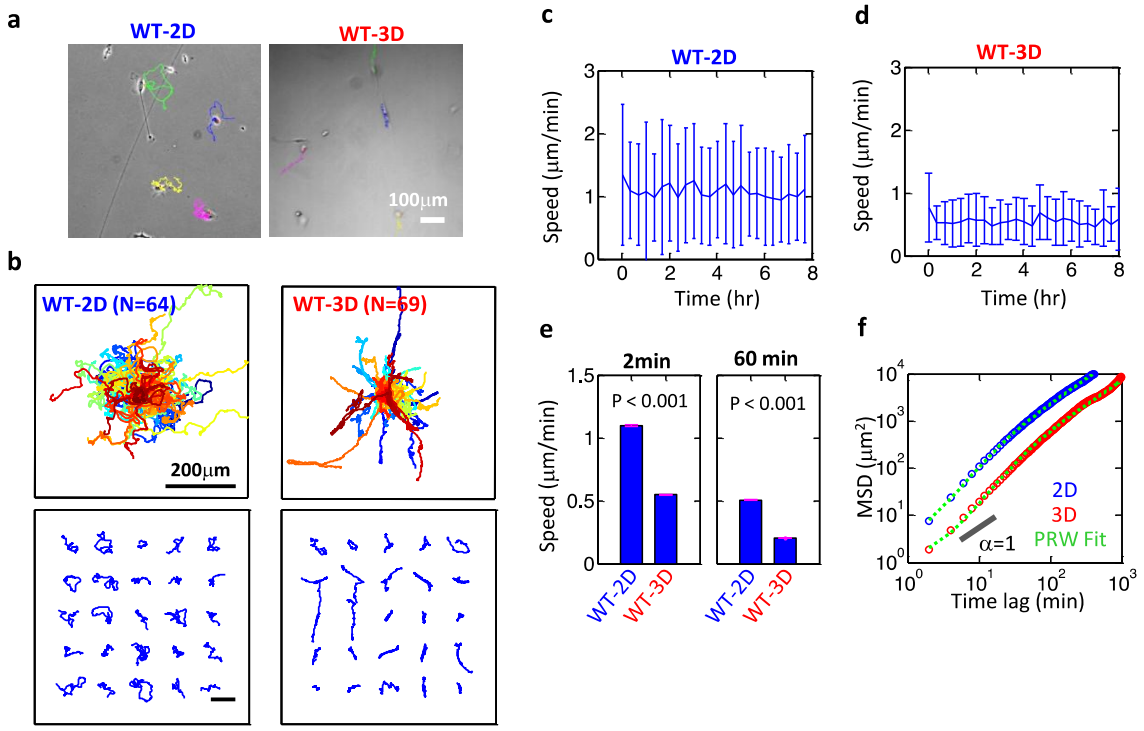

Figure 4-1. The persistence random walk (PRW) model of cell migration on 2D and 3D matrices.

A. Phase contrast images of human fibrosarcoma cells on a flat collagen I-coated dish (2D) and cells embedded in a 2mg/ml collagen matrix (3D). Scale bar, 100 □ m. Cells were tracked for 8 or 16 h and trajectories of these cells were overlaid on the initial micrographs. **B**. Cell trajectories on 2D collagen-coated surfaces and inside a 3D collagen matrix (top); each color represents the trajectory of an individual cell. For better visual comparison, trajectories of 25 randomly selected cells in both conditions (bottom) are shown. Scale bars, 200 □ m. **C and D**. Population-averaged cell speed measured at a time scale of □ =2 min at different time points during the duration of the experiments (8h), in 2D (c) and 3D conditions (d). This data shows that possible changes in the microenvironment (e.g. changes in cell density during the experiments) did not change cell speed. **E**. Cell speed evaluated at a short time lag (□ =2min) and a long time lag (□ =60min) in both 2D and 3D environments. Cells on 2D dishes have significantly higher speed than in collagen gels (*t*-test, *P*-value < 10^{-3}). Error bars represent the standard error of the mean. **F**. Population-averaged mean squared displacements (MSDs) of cells on 2D substrates (blue curve) and in 3D matrix (red curve). Green dotted lines represent the fits of experimental population-averaged MSDs with the conventional PRW model (R^2 = 1, Eq. 2). Error bars represent the standard error of the mean. Sixty-four and 69 cells were tracked in 2D and 3D, respectively. Movies were at least 8h long; a frame was captured every 2 min.

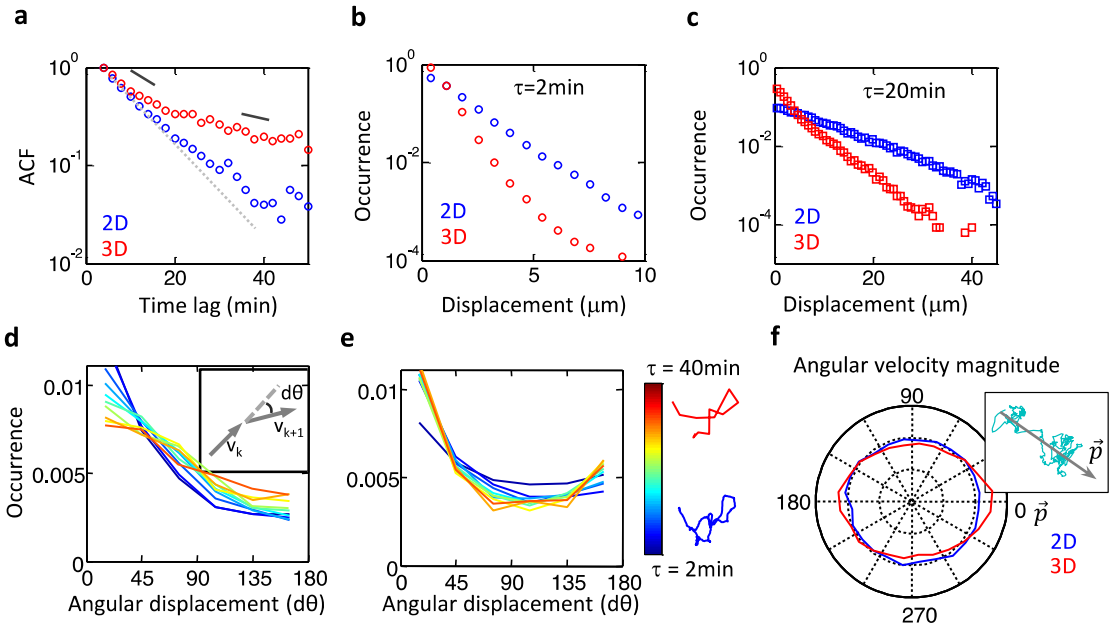

Figure 4-2. Distinct statistical features for 2D and 3D cell migration.

A. Autocorrelation function (ACF) of velocities measured at a 2-min time lag on 2D substrates (blue) and in 3D matrices (red). The grey dotted line indicates a single-exponential ACF computed from a short-time lag fit of the experimental ACF using the PRW model. **B and C**. Probability density functions of cell displacements at the 2-min (b) and 20-min time lags (c), on 2D substrates (blue) and in 3D matrices (red). **D and E**. Distributions of angular displacements (d□, see graphical definition in inset) evaluated at time lags ranging from 2 to 40 min in 2D (d) and 3D (e). Color code corresponds to different time lags. **F**. To measure the anisotropic properties of cell displacements, we identified the primary cellular migration axis ($\vec{p}$, graphical definition in inset) using singular vector decomposition (SVD) of individual cell velocities and aligned along the primary migration axis of individual cell trajectory with the horizontal axis (see Methods section for more details). Velocities for 2D (blue) and 3D (red) migrations at different orientations relative to the longitude axis of cell trajectories ($\vec{p}$) were computed and visualized in a polar plot. Same primary dataset as in Fig. 1.

that cell velocity becomes difficult to define clearly at high camera frame rates when apparent cell migration is mostly due to subcellular movements and fast irregular changes of cell morphology without real cell translocation. The total observation time period is also intrinsically limited by the time between cell divisions, which is ~16-24 h for HT-1080 cells. As a consequence, for instance, to determine whether the distribution of cell velocities is Gaussian, as presumed by the PRW model, or exponential for a single cell is probe to error. Hence, beyond fits of individual MSDs, fully validating the PRW model at single-cell level is inherently difficult.

An alternative solution has been to obtain statistical characteristics of cell motility from population-averaged profiles to reach the required resolution (Czirok et al. 1998, Takagi et al. 2008, Selmeczi et al. 2005). The underlying assumption of this method is that individual cells have equally probable motile behavior, a notion we test rigorously in this paper.

4.3.3 Fundamental statistical differences between 2D and 3D migration

A first implication of the excellent fit between measured MSDs and MSDs predicted by the PRW model (Fig. 4-1 F) is that the autocorrelation function (ACF) of cell velocity, both in 2D and 3D environments, should decay as a single exponential with a relaxation time equal to the persistence time *P*. We found that the decay of the ACF did not follow a single-exponential relaxation. Rather, ACF profiles followed a two-step process characterized by two characteristic time scales. For 2D migration, we observed a slower-than-predicted decrease of the ACF at long time scales, τ > 30min (blue curve, Fig 4-2 A). Such a two-step profile for the ACF has previously been observed in 2D migration (Selmeczi et al. 2005). The slower-than-expected decrease of the ACF was even more pronounced in 3D motility (red curve, Fig 4-2 A).

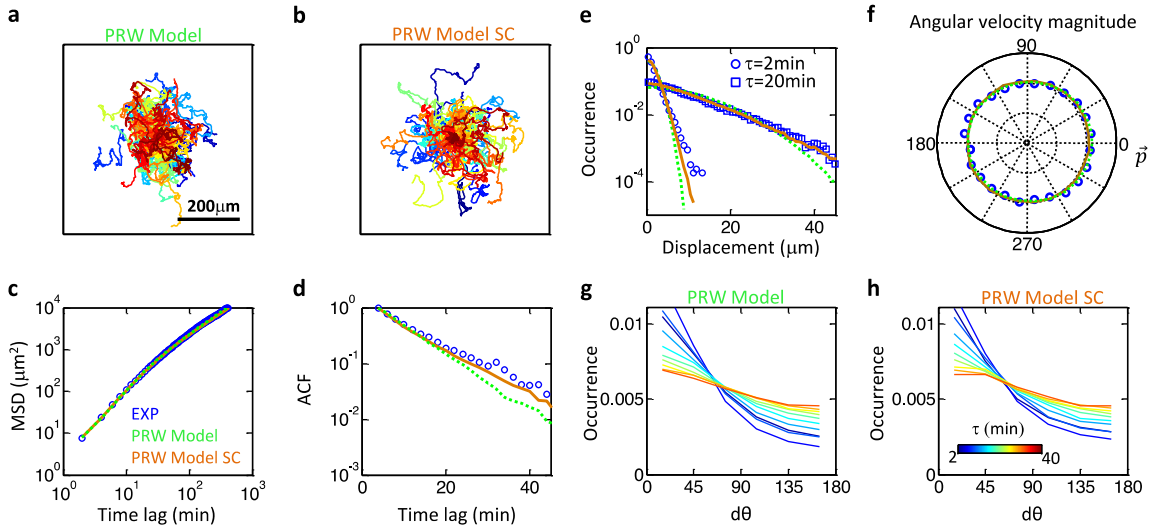

Figure 4-3. Cell heterogeneity explains the exponential distribution of velocities in 2D migration

A and B. Cell trajectories on 2D substrates simulated using the persistent random-walk (PRW) model based on *P* and *S* values obtained from the population-averaged MSD profile (a) or based on *P* and *S* values obtained from MSDs of single cells (b). Scale bar, 200 □ m. **C.** Population-averaged MSDs of trajectories simulated using these two models. The PRW model fitted from the ensemble-averaged MSD (green) and the PRW model fitted from individual cell MSDs (orange) both describe well the experimental MSD data (blue). **D**. ACF obtained from the PRW model when including single-cell information (orange) approximates the experimental data (blue) better than the PRW model derived from the ensemble-averaged MSD (green). **E**. Distributions of cell displacements for the two models. The PRW model when it includes single-cell information, but not the PRW model using ensemble-averaged MSD, qualitatively and quantitatively predicts the exponential distribution of experimental cell displacement histogram. **F**. Velocity magnitude profiles as a function of orientations for these two models. **G and H**. Distributions of angular displacements using the PRW model based on ensemble-averaged MSDs (g) and the PRW based on individual cell MSDs (h). Color code corresponds to different time lags (Inset in panel h). Same primary dataset as in Fig. 1.

A second implication of the goodness of fits between measured MSDs and MSDs predicted by the PRW model (Fig. 4-1 F) is that the distribution of cell velocities should follow Gaussian statistics. Instead, ensemble-averaged results showed that cell displacements followed an exponential distribution at all probed time scales (Fig. 4-2, B and C), not only in the 2D case (blue curves) as previously observed (Czirok et al. 1998, Selmeczi et al. 2005), but also for in the 3D case (red curves). Importantly, we found that this exponential distribution of cell velocity was independent of the method of tracking of cell movements (Fig. 4-7 and see Methods for details).

A third implication of the excellent fits between measured and predicted MSDs (Fig. 4-1 F) is that the angular distribution of cell movements should flatten over time. We measured angular displacements d during cell migration and computed their distribution (Fig. 4-2 D). We found that the distribution in d at different time scales in 3D showed profiles fundamentally different from those in 2D. For 2D motility, the distribution in d was elevated at small angles, corresponding to cells moving persistently at short time scales, becoming a uniform distribution at long time scales. This is the result predicted by the conventional PRW model (see Methods for details). However, the high probability to observe small d values observed during 3D motility at short time scales did not disappear over time (Fig. 4-2 E). Instead of the expected flattening of the distribution of angles between cell movements overtime, the probability to observe large angular displacements progressively increased around 180°, corresponding to cells moving in the exact opposite direction to the direction of movements separated by long time lags. This result indicates that, at long time scales, the probability increased to observe cells moving back into the 1-D tunnel-like tracks in the 3D matrix formed by the cells during their initial exploration of the matrix.

Based on this result, we studied whether the magnitude of velocity was spatially anisotropic. First, we identified and then re-aligned the primary direction of migration ($\vec{p}$) of individual cells using the singular-vector decomposition method (SVD, Fig. 4-2 F, inset). $\vec{p}$ for each cell is an estimate of the primary direction of migration equal to the principal axis of all instantaneous velocities of that cell. We measured the magnitude of the velocity (at a 2-min time lag) at different orientations relative to $\vec{p}$. This analysis indicated that cells in 3D matrix displayed a higher velocity along their primary migration axes, which include both $\vec{p}$ and -$\vec{p}$, compared to the velocity along the direction of migration perpendicular to $\vec{p}$ (Fig. 4-2 F and Fig. 4-8). In sum, when analyzed through their individual or ensemble-averaged MSD profiles, cell motility patterns in 2D and 3D seem to be quantitatively different, but qualitatively similar. However good fits of MSDs constitute a weak test for models of cell migration and comprehensive statistical analysis reveals instead that cell motility patterns in 2D and 3D environments are qualitatively different. Cells migrating in a 3D matrix display qualitatively different angular displacement distributions from their 2D counterparts and, unlike in 2D migration, display an anisotropic velocity.

4.3.4 Cell heterogeneity alone explains the non-Gaussian velocity distribution in 2D

Accumulating evidence suggests a strong correlation between cell phenotypic heterogeneity and clinical outcomes, particularly in cancer. We hypothesized that the non-Gaussian nature of the velocity distribution could stem from cell heterogeneity. Therefore we assessed the degree of migratory heterogeneity in 2D and 3D environments. Here we found that, despite the homogeneous environment of 2D substrates, individual HT-1080 cells already displayed significantly different motility profiles from each other. A one-way ANOVA test of velocities of different pairs of individual cells evaluated at a time lag of 2

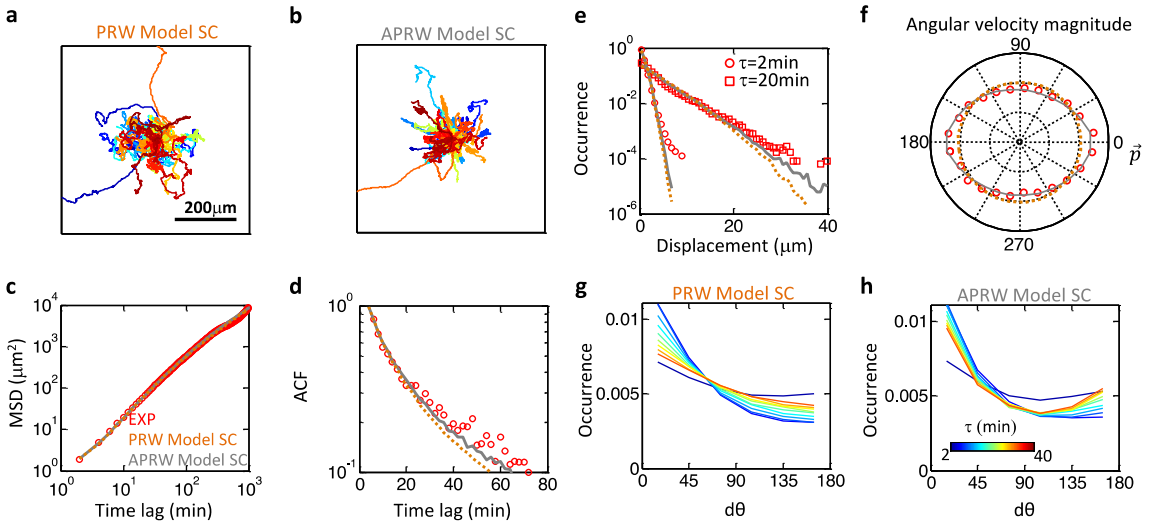

Figure 4-4. Anisotropic cell migration patterns in 3D matrices and the APRW model

A and B. Cell trajectories in 3D matrices simulated using the PRW model (A) and the APRW model (B), which here both include single-cell information (see Methods section for more details). Scale bar, 200 □ m. **C**. MSD profiles computed from simulated trajectories using the PRW (orange) and APRW models (grey). Both models describe well the experimentally observed MSDs in 3D matrices. **D**. ACFs of cell velocities derived from the PRW model (orange) and APRW (grey) model. APRW model approximates the experimental ACF data better than the PRW model. **E**. Distributions of displacements for the PRW (orange) and APRW (grey) models. Both models correctly predict the exponential distribution of displacements, but the APRW model provides a better fit, especially at large displacements, at a time lag of 20 min. **F**. Velocity magnitude profiles at different orientations for these two models. The PRW model does not characterize the experimentally observed anisotropic aspect of velocity. **G and H**. Distributions of angular displacements for the PRW (G) and APRW (H) models. The APRW model qualitatively and quantitatively describes the experimental results, including the increasing occurrence of displacements near 180 degree at larger time lags. Same primary dataset as in Fig. 1.

min showed that more than 50% of paired cells had different mean velocities with *P*-value < 0.05 (Fig. 4-9 A). Similar results were obtained for cell motility in 3D matrices (Fig. 4-9).

We first described the motility of individual cells using the PRW model by simulating cell trajectories using experimentally measured paired values of persistent time *P* and speed *S* for each individual cell (Fig. 4-4 B; see details about simulations under Methods). For the sake of comparison, we also simulated cell trajectories using the same *P* and *S* derived from population-averaged MSDs to model trajectories (Fig. 4-3 A). Ensemble-averages MSDs (Fig. 4-3 C), ACFs (Fig. 4-3 D), velocity distributions (Fig. 4-3 E), and anisotropic maps (Fig. 4-3 F) of these two sets of simulated trajectories were then computed and compared. While MSD profiles predicted by both approaches were in good agreement with the experimental results (Fig. 4-3 C), ACFs obtained from the PRW model that included single-cell distribution provided better fits when including cell heterogeneity (Fig. 4-3, D and E). Remarkably, when incorporating cell heterogeneity, the new PRW model correctly predicted the exponential distribution of cell velocities (Fig. 4-3 E). Both approaches also correctly predicted the distributions of angular displacements (Fig. 4-3, F and G).

Together, our results indicate that the simple PRW model, when it includes cell heterogeneity, captures essential statistical characteristics of cell migration, at least on 2D substrates. In contrast, 3D migration using the PRW model, even when incorporating cell heterogeneity, yielded trajectories and associated statistical characteristics that were qualitatively distinct from experimental results (Fig. 4-4, A and E-H). This means that, unlike the 2D case, the PRW model, even when including cell heterogeneity, does not explain qualitatively or quantitatively cell migration in 3D matrix.

4.3.5 A new anisotropic PRW model fully describes 3D migration

In the conventional PRW model, the velocity of cells is presumed to be spatially isotropic. However, an important characteristic of 3D cell migration is its highly anisotropic velocity profile (e.g. Fig. 4-2 B). SVD analysis of cell velocities identified primary and non-primary directions of migration (Fig. 4-2 F). We extracted the MSDs and ACFs of individual cells along these two directions and found that cell migration is a self-correlative process and that MSDs in each direction are well described by the PRW model (Fig. 4-8; see more details under Methods). Hence, we extended the PRW model to the anisotropic PRW model (APRW), which incorporates different persistent times and speeds in the primary (P_p, S_p) and non-primary (P_{np}, S_{np}) directions of migration and found that in these different directions cells followed PRW statistics. R-squared values derived from fitting APRW models into primary and non-primary directions of migration were > 0.95, which suggests that the APRW model describes 3D migration.

To test the APRW model, we simulated 3D cell migration trajectories with experimentally measured single-cell values of P and S (Fig. 4-4, A and B; see more details under Methods). MSD profiles obtained from the PRW model that does not acknowledge anisotropy and the APRW model that does both fitted well experimental MSDs (Fig. 4-4 C). However, we already know that a good fit of MSDs is a weak test of models of cell migration (Fig. 4-1). The two-step decay of the ACF and the exponential velocity distribution were qualitatively and quantitatively better predicted by the APRW model than the PRW model (Fig. 4-4, D and E). Moreover, the observed anisotropic velocity profiles and distributions of angular displacements, which were inaccurately anticipated by the PRW model, were correctly predicted by the APRW model (Fig. 4-4, F-H). Together, our results indicate that the new APRW model successfully describes the heterogeneous and anisotropic motility patterns of migratory cells in 3D matrix.

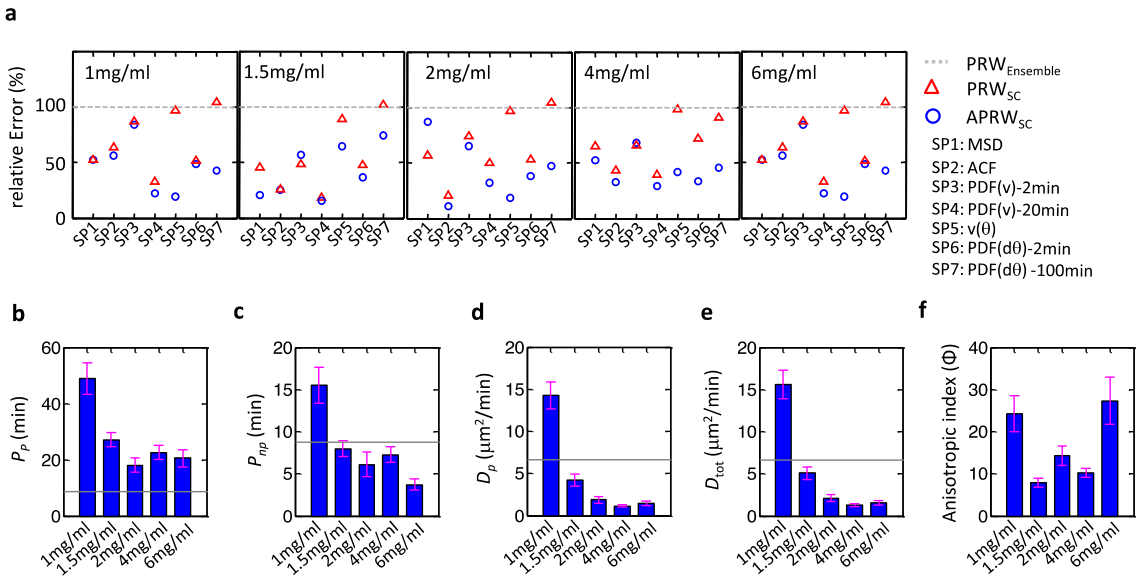

Figure 4-5. The APRW model characterizes 3D cell migration at different collagen densities

Cell migratory profiles in matrices of different collagen concentrations were analyzed using the APRW model, which incorporates cell heterogeneity. **A.** Goodness of the model fits for HT1080 cell motility in matrices of collagen density of 1mg/ml, 1.5mg/ml, 2mg/ml, 4mg/ml, and 6mg/ml. Goodness of fit was scored by the root mean squared error (RMSE) and was normalized by the RMSE value from the PRW model derived from the ensemble-averaged MSDs. PDF(v) and PDF(d□□ are the probability density functions of the velocity v and the angular displacement d□, respectively, evaluated at 2 min and 20 min, and v(□) is the magnitude of the velocity at different angles. **B-F.** Mean values of persistence time along the primary axis of migration (B), persistence time along the non-primary axis of migration (C), cell diffusivity along the primary axis of migration (D), overall cell diffusivity (E) and anisotropic index (F) of HT1080 cells in matrices of increasing collagen concentration. Error bars represent standard error of the mean. At least 60 cells were tracked for 16 h every 2 min for each collagen concentration.

4.3.6 Diffusive patterns and effects of collagen density

We have demonstrated that the APRW model properly characterizes cell motility in 3D matrix at a fixed concentration collagen I. As a more comprehensive test of the APRW mode, we next investigated how statistical characteristics of 3D cell migration were modulated by changes in collagen density (Fig. 4-5). MSDs, displacement distributions, autocorrelation functions, and angular distribution were well fitted over a wide range of collagen density with the APRW model of 3D migration (Fig. 4-5 A and Fig. 4-9). We note the great improvement of the fits of anisotropic profiles of velocity and angular displacement distributions compared to the PRW model and PRW model that takes into account cell heterogeneity.

Cells in a 3D collagen I matrix moved most persistently at a concentration of 1mg/ml; the mean persistent time along the primary migration direction decreased with increasing collagen density (Fig. 4-5, B and C). Cell migration in 1mg/ml collagen matrices also showed the highest diffusivity, measured as $D_{tot}=(S_p{}^2P_p + S_{np}{}^2P_{np})/4 \approx MSD_{\text{long}}$ $_{\text{times}}/4\square\square$: the mean cell diffusivity decreased monotonically with collagen concentration before plateauing at 4mg/ml (Fig. 4-5, D-F). The ratio of diffusivities along the primary and non-primary migration directions (which we call the anisotropic index ϕ) also depended on collagen concentration (Fig. 4-5 G). In sum, these results show that the mean values of descriptors of 3D cell migration, including persistent time, diffusivity, and anisotropic index, are tightly regulated by collagen density and that the APRW model describes well 3D migration over a wide range of collagen concentrations.

4.3.7 Cell diffusive patterns and searching strategies in 3D

We next identified functional relationships among the different descriptors of 3D cell migration through systematic correlative analysis. We found that some of these cell-

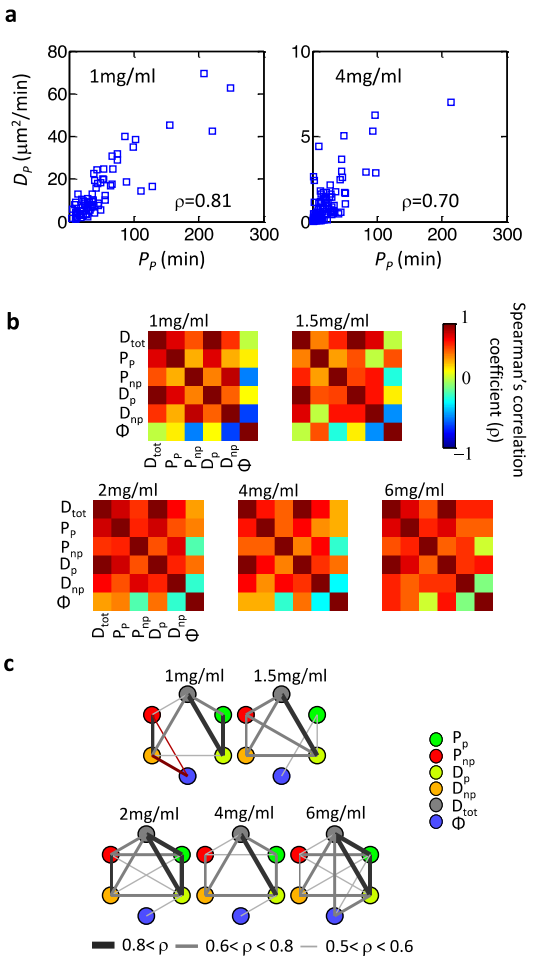

Figure 4-6. Correlation between speed and persistence at the single-cell level

a. Persistence time and diffusivity along the primary migration axis of migration of single cells are correlated for 3D cell motility in 1mg/ml (left) and 4mg/ml collagen I matrices (right). □□ is the Spearman coefficient of correlation. **b.** Heat maps show correlation coefficients among different cell-motility descriptors at the single-cell level for 3D cell migration in collagen matrices of different concentration. These motility descriptors for individual cells were obtained fits using the APRW model incorporating cell heterogeneity. Color code corresponds to different values of the Spearman correlation coefficient. **c**. Network plots showing correlative maps among overall cell diffusivity and other descriptors of cell migration at single-cell level in matrices of increasing collagen concentration. Paired parameters with correlation coefficient between 0.5-0.6, 0.6-0.8, and >0.8 are linked by thin light, thick light, and thick dark gray lines, respectively. A negative correlation is shown by a thin brown line. The topology of the network shifted with increasing collagen density. Same primary dataset as in Fig. 5.

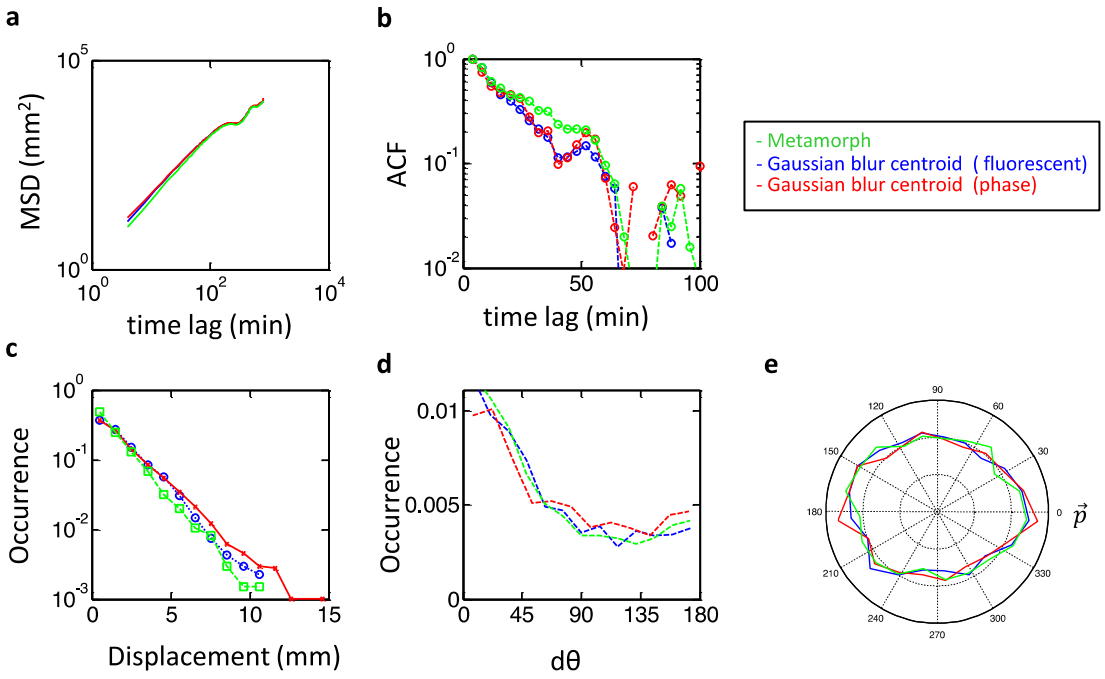

Figure 4-7. Statistical profiles of cell motility derived from three different cell tracking methods, Metamorph (phase images), Gaussian blur centroid (fluorescent images) and Gaussian blur centroid (phase images).

A. Cell population-averaged MSD profiles of cells. **B**. Autocorrelation function of velocity evaluated at 2-min time lag. **C**. Probability density functions of cell displacements at the 2-min time lags. **D**. Angular displacements from a series of cell velocities at a time lag of 2 min. **E**. Velocities for 2D and 3D migration at different orientations relative to the primary migration axis of cell trajectories ($\vec{p}$) were computed and visualized in a polar plot.

motility descriptors were correlated with each other. For example, the persistence time and diffusivity were highly correlated for cell motilities in 1mg/ml and 4mg/ml matrices with correlation coefficients of 0.81 and 0.70, respectively (Fig. 4-6 A). The extent of inter-dependence among the five major motility descriptors, including total diffusivity (D_{tot}), persistence time and diffusivity along the primary axis (P_p and D_p) and non-primary axis of migration (P_{np} and D_{np}), the anisotropic index ϕ,

$$\Phi \equiv \frac{D_P}{D_{np}} = \frac{S_p{}^2 P_p}{S_{np}{}^2 P_{np}}$$

and their mutual-correlation profiles, were evaluated through heat maps (Fig. 4-6 B) and correlation network diagrams (Fig. 4-6 C) as a function of collagen density.

Some expected correlations among descriptors of migration were observed, such as the high correlation between total diffusivity and primary or non-primary diffusivity (e.g. see thick lines between D_{tot} and D_p and, to a lesser extent, between D_{tot} and D_{np}; see Fig. 4-6 C), since total diffusivity is a weighted combination of both. These constitute positive controls. However, our analysis revealed a strong dependency between *a priori* independent variables, including the persistent time and diffusivity along the principal axis of migration (P_p and D_p; Fig. 4-6 C) and a strong association between the primary diffusivity and non-primary diffusivity (D_p and D_{np}; Fig. 4-6 C) across a wide range of conditions.

These results suggest the existence of underlying constrains for cell migration set by common robust molecular pathways that regulate 3D cell motility, independently of changes in collagen density. Moreover, since persistent time and speed are correlated across a wide range of conditions, they are not controlled by purely stochastic processes. We also found that the relation of the anisotropic index ϕ with other migration descriptors (i.e. the high connectivity of the blue dot with other dots in the hexagon network, Fig. 4-6 C) changed

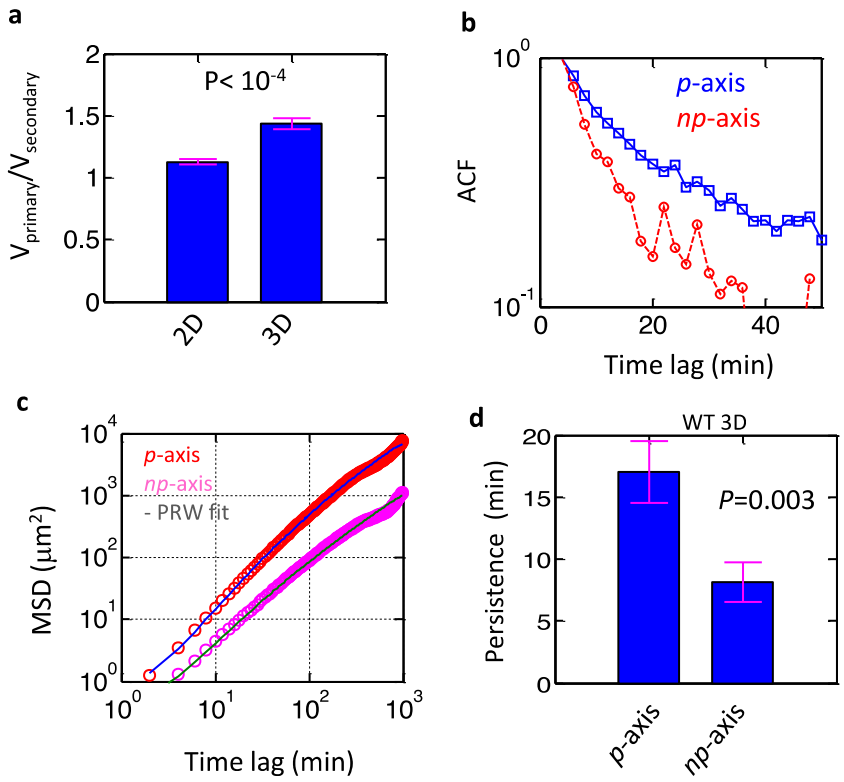

Figure 4-8. Differential anisotropic motility characteristics for 2D and 3D cell migration

Ratio of average cell speed along the primary migration axis ($\vec{p}$-axis) to cell speed the along non-primary migration axis ($\overrightarrow{np}$-axis). In 2D, the ratio is approximately one, while cell motility in 3D is anisotropic. **b**. Autocorrelation function of velocity along the primary and non-primary migration directions evaluated at 2-min time lag. The correlation in velocity decayed over time, more rapidly along the non-primary migration than along the primary migration directions. **c**. Cell population-averaged MSD profiles of cells in 3D matrices, along the $\vec{p}$-axis and $\overrightarrow{np}$-axis. Both MSD profiles are well fitted by the PRW model. **d**. Persistence time along these two axes. Persistent time was evaluated from a PRW model fit at the single-cell level. Results showed significant difference in persistence of cell migration along the $\vec{p}$- and $\overrightarrow{np}$-axes.

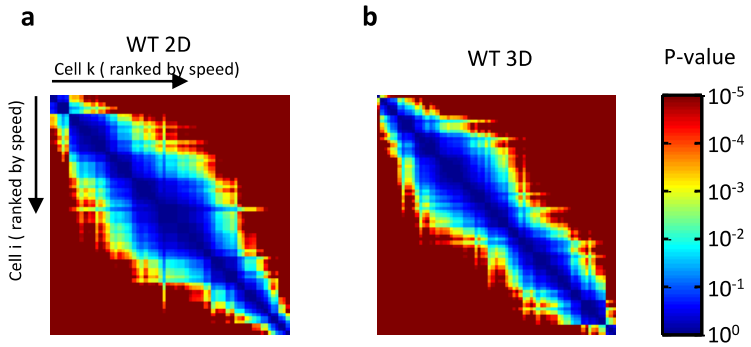

Figure 4-9. Single-cell average speed is not equally likely in both 2D and 3D.

All tracked cells in 2D or 3D were ranked based on their averaged 2-min speed. *P*-value from a student t-test was used to score the significance in the difference in averaged speed between all cell pairs. Heat maps were plotted to show the results where position of (k,i) on the heat map shows the *P*-value of cell speed between k-th and i-th cells in both 2D (A) and 3D (B).

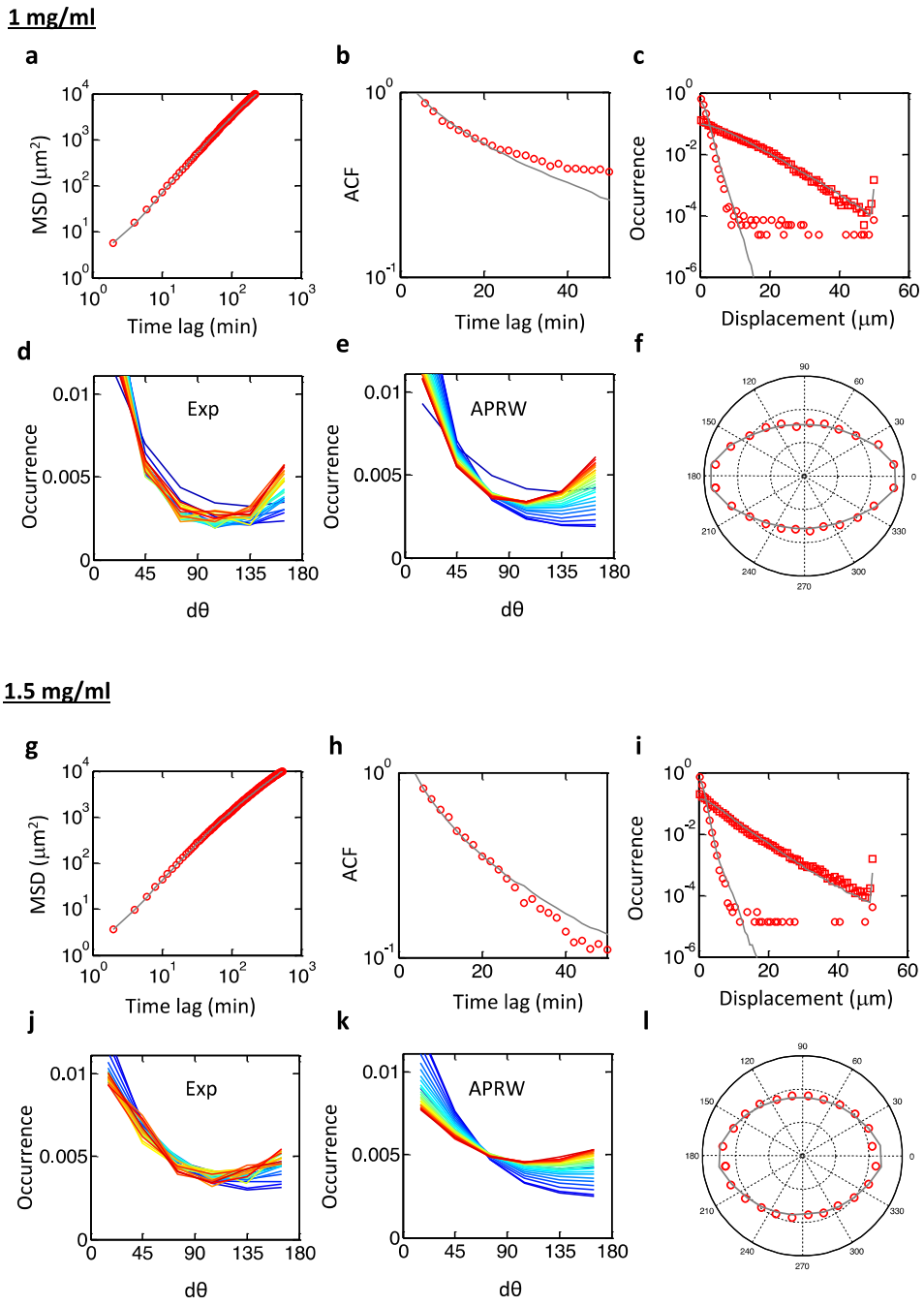

Figure 4-10. Statistical profiles of 3D cell motility at different collagen concentrations

A, G, M, S. MSD profiles computed from experimental observations (red) and computer-simulated trajectories using the APRW model (gray). **B, H, N, T.** ACFs of cell velocity derived from the APRW model. C, I, O, U. Distribution of displacements for the APRW model. **D, E, J, K, P, Q, V**. Distributions of angular displacements result from the experiment observations (D, J, P, V) and the APRW (E, K, Q) model. **F, L, R, X.** Velocity magnitude profiles varied orientations from experimental measurements and APRW models.

Figure 4-10 (continued)

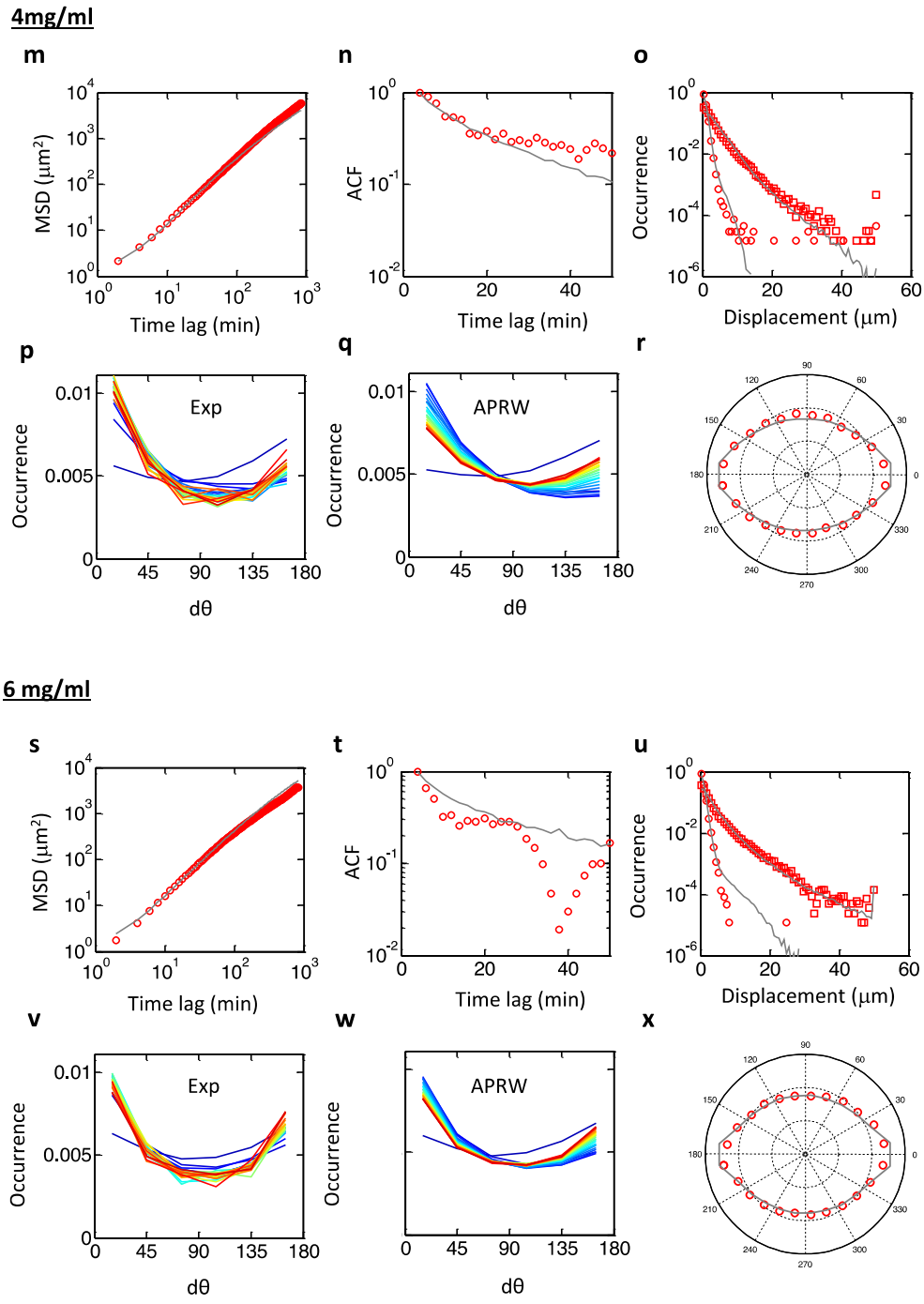

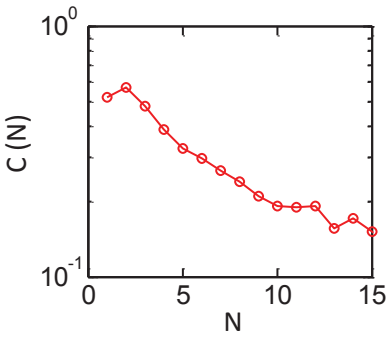

Figure 4-11. Autocorrelation function ($\widehat{C}(N)$) of cell velocity in 2mg/ml collagen matrices.

qualitatively with collagen concentration. Indeed, the anisotropic index was negatively correlated with diffusivity along the minor axis of migration at 1mg/ml condition, while strongly positively correlated with total diffusivity at 6mg/ml. These findings suggest that highly motile cells in low-density and high-density collagen are mechanistically distinct. Collectively, these analyses indicate that strategies for matrix exploration by cells are tightly regulated by collagen density.

4.4 Discussion

This work shows that the traditional persistence-random walk (PRW) model, which is ubiquitously used to parameterize cell migration into speed and persistence time (Wolf et al. 2013) is based on assumptions that are not met in the physio-pathological-relevant case of a 3D extracellular matrix. Since the underlying assumptions of the PRW model – exponential velocity autocorrelation, Gaussian distribution of velocities, and flat angular distributions at long time scales – cannot be rigorously tested at the single-cell level because of limited (meaningful) spatial resolution and a time of collection limited by cell division, we and others (Czirok et al. 1998, Selmeczi et al. 2005, Takagi et al. 2008) have used population-averaged values of these parameters. These discrepancies in the 2D case have typically been accounted for by adding new fitting parameters (Selmeczi et al. 2005, Takagi et al. 2008). Here we show that, in 2D migration, cell heterogeneity is sufficient to understand the population-averaged non-Gaussian (exponential) distribution of velocities and the non-exponential decay of the velocity autocorrelation. Therefore, the PRW model qualitatively holds in 2D migration.

However, the PRW model, even when incorporating cell heterogeneity, does not property describe 3D migration even qualitatively (Figs. 4-4 and 4-5). This indicates that cell migration patterns in a 3D matrix do not follow persistent random walks. Any random-walk

model of cell migration would predict that the distribution of angles between cell moves flattens at time scales longer than the persistence time. Instead, we find that the probability of complete 180^0 turnabout in the 3D matrix increases with time (Fig. 4-2 E). Rather than an angular distribution becoming flat at long time scales, it peaks at 0^0 and 180^0 and is minimum at 90^0 (Fig. 4-2 E and Fig. 4-10). One of possible reasons for this unexpected polarized distribution is due to the fact that fibrosarcoma cells create tube-like microchannels of diameter approximately equal to their nucleus by locally digesting the collagen matrix at their leading edge, mainly thanks to the surface-bound metalloproteinase MT1-MMP (Czirok et al. 1998, Wolf et al. 2013). These microchannels can greatly reduce the number of possible cell movements. In contrast, there are no local obstacles that would restrict the re-orientation of migratory cells in the 2D case.

SVD analysis of cell trajectories (Fig. 4-2 F) shows that, unlike its 2D counterpart, 3D migration is anisotropic (Fig. 4-8 A). A complete parameterization of 3D migration at the single-cell level, therefore, requires not only speed and persistence time, but also an anisotropy index (Fig. 4-5 F). This new model of 3D cell migration correctly predicts the non-exponential profile of the velocity autocorrelation function and the complex time-dependent angular distribution of cell movements in 3D matrix.

When matrix density is changed, a myriad of microstructural parameters of the matrix are changed accordingly, including ligand density, pore size of the matrix, fiber thickness, fiber alignment, matrix stiffness, etc. Yet, despite this wide range of conditions, we found that cell diffusivity in 3D matrices consistently predicts its persistence, two parameters of cell migration that are *a priori* independent (Fig. 4-6, B and C).

CHAPTER 5

Conclusions & Future Work

5.1 Review of Findings

In this work, I have studied roles of the actin and the microtubule cytoskeleton in regulating 3D cell migration. There has been a lot of interest in studying cell migration and many of the regulatory pathways pertaining to cell migration have been probed in great detail. Our understanding of how and at what levels molecules interact to bring out cell migration has stemmed from our understanding of 2D cell biology. However, cells migrating in complex 3D systems are exposed to very different conditions than in 2D: different local density of matrix, ligand presentation, stiffness, pore size to name a few. Understanding how cell interact and migrate in 3D systems can provide a foundation for developing new therapies to treat or even prevent metastasis. I have explored the role of actin nucleating proteins, Arp2/3 and its activators N-WASp, WAVE1, Cortactin, and Cdc42 in 3D migration. The results show that the effects of depleting these proteins in 3D cannot be simply extracted from the 2D case; the levels of effect on cancer cell migration were different. I also show that cell migration is 3D matrix is mediated by the total number of daughter protrusions the cells make, as discussed in Chapter 2 and Chapter 3. I developed a system of classifying protrusions based on the order they appear on cells. This method was used in subsequent experiments to quantify the number of protrusions and to study correlation with cell migration. In Chapter 3, I explored the role of microtubules in cell

migration and show that microtubule interacting drugs had a much larger effect in 3D than in 2D. Depleting important microtubule interacting proteins EB1 and cytoplasmic dynein revealed that these proteins did not mediate 2D cell migration but drastically reduced cell migration in 3D matrices. These results open up the possibility of targeting proteins that were previously thought to be not important for cancer cell migration. In this same study, I observed a fundamentally different organization of the actin and microtubule cytoskeleton in cell growing in 3D matrices. Next, I developed a model for characterizing cell migration in 3D matrices, discussed in chapter 4.

5.2 Future Work

An extension of this work could be studying cell migration in 3D matrices under the influence of chemical gradients. Chemical cues have been known to influence the migration pattern of eukaryotic cells in many biological processes, which include embryogenesis during development and the movement of neutrophils to the site of infection, and recently there have been indications that certain chemicals direct the migration of prometastatic cells from the primary tumor and into the vasculature. Studying chemotaxis in 3D may help us identify proteins that play vital roles in cancer cell migration.

From this study, I have identified proteins, which have the potential of being used as a target in cancer therapies. It would be interesting to see if these proteins stop or slow metastasis in animal models of cancer. I think the real power of the 3D culture would be realized if we could tune the 3D culture system to predict the results of *in vivo* animal models.

Another extension of this study could be leveraging the physiological platform of a 3D matrix to screen small molecular drugs and biologics. Currently, drug screening is commonly conducted on 2D multi-well format dishes and based on my own studies of cell behavior in 2D and 3D and also studies from other groups (Sun et al. 2006, Lee et al. 2009,

Pampaloni, Reynaud, and Stelzer 2007, Sabeh, Shimizu-Hirota, and Weiss 2009), the results from these studies may be misleading. The 3D culture platform has the potential to uncover drugs that may otherwise go unnoticed.

REFERENCES CITED

American Cancer Society. 2014. Cancer Facts & Figures 2014.

Applegate, K. T., S. Besson, A. Matov, M. H. Bagonis, K. Jaqaman, and G. Danuser. 2011. "plusTipTracker: Quantitative image analysis software for the measurement of microtubule dynamics." *Journal of Structural Biology* 176 (2):168-184. doi: Doi 10.1016/J.Jsb.2011.07.009.

Asokan, R., G. K. Reddy, and S. C. Dhar. 1993. "Neoplastic association of enhanced type V collagen production in rat fibrosarcoma." *Mol Cell Biochem* 120 (1):25-32.

Balzer, E. M., Z. Tong, C. D. Paul, W. C. Hung, K. M. Stroka, A. E. Boggs, S. S. Martin, and K. Konstantopoulos. 2012. "Physical confinement alters tumor cell adhesion and migration phenotypes." *FASEB J* 26 (10):4045-56. doi: 10.1096/fj.12-211441.

Berg, Howard C. 1993. *Random walks in biology*. Expanded ed. Princeton, N.J.: Princeton University Press.

Bloom, R. J., J. P. George, A. Celedon, S. X. Sun, and D. Wirtz. 2008. "Mapping local matrix remodeling induced by a migrating tumor cell using three-dimensional multiple-particle tracking." *Biophys J* 95 (8):4077-88. doi: 10.1529/biophysj.108.132738.

Buccione, R., G. Caldieri, and I. Ayala. 2009. "Invadopodia: specialized tumor cell structures for the focal degradation of the extracellular matrix." *Cancer Metastasis Rev* 28 (1-2):137-49.

Buccione, R., J. D. Orth, and M. A. McNiven. 2004. "Foot and mouth: podosomes, invadopodia and circular dorsal ruffles." *Nat Rev Mol Cell Biol* 5 (8):647-57.

Centers for Disease Control and Prevention. 2010. "Leading Causes of Death." Last Modified January 11, 2013 Accessed February 19, 2014. http://www.cdc.gov/nchs/fastats/lcod.htm.

Chaffer, C. L., and R. A. Weinberg. 2011. "A Perspective on Cancer Cell Metastasis." *Science* 331 (6024):1559-1564. doi: Doi 10.1126/Science.1203543.

Chan, A. Y., S. J. Coniglio, Y. Y. Chuang, D. Michaelson, U. G. Knaus, M. R. Philips, and M. Symons. 2005. "Roles of the Rac1 and Rac3 GTPases in human tumor cell invasion." *Oncogene* 24 (53):7821-9. doi: 10.1038/sj.onc.1208909.

Chang, S. S., W. H. Guo, Y. Kim, and Y. L. Wang. 2013. "Guidance of Cell Migration by Substrate Dimension." *Biophysical Journal* 104 (2):313-321. doi: DOI 10.1016/j.bpj.2012.12.001.

Christiansen, D. L., E. K. Huang, and F. H. Silver. 2000. "Assembly of type I collagen: fusion of fibril subunits and the influence of fibril diameter on mechanical properties." *Matrix Biology* 19 (5):409-420. doi: Doi 10.1016/S0945-053x(00)00089-5.

Clark, E. S., A. S. Whigham, W. G. Yarbrough, and A. M. Weaver. 2007. "Cortactin is an essential regulator of matrix metalloproteinase secretion and extracellular matrix degradation in invadopodia." *Cancer Res* 67 (9):4227-35.

Cowan, C. R., and A. A. Hyman. 2004. "Asymmetric cell division in C-elegans: Cortical polarity and spindle positioning." *Annual Review of Cell and Developmental Biology* 20:427-453. doi: Doi 10.1146/Annurev.Cellbio.19.111301.113823.

Czirok, A., K. Schlett, E. Madarasz, and T. Vicsek. 1998. "Exponential distribution of locomotion activity in cell cultures." *Physical Review Letters* 81 (14):3038-3041. doi: DOI 10.1103/PhysRevLett.81.3038.

Derry, J. M., H. D. Ochs, and U. Francke. 1994. "Isolation of a novel gene mutated in Wiskott-Aldrich syndrome." *Cell* 78 (4):635-44.

Dujardin, D. L., L. E. Barnhart, S. A. Stehman, E. R. Gomes, G. G. Gundersen, and R. B. Vallee. 2003. "A role for cytoplasmic dynein and LIS1 in directed cell movement." *J Cell Biol* 163 (6):1205-11. doi: 10.1083/jcb.200310097.

Dunn, G. A. 1983. "Characterising a kinesis response: time averaged measures of cell speed and directional persistence." *Agents Actions Suppl* 12:14-33.

Etienne- Manneville, S. 2004. "Actin and microtubules in cell motility: which one is in control?" *Traffic* 5 (7):470-477.

Fooksman, D. R., T. A. Schwickert, G. D. Victora, M. L. Dustin, M. C. Nussenzweig, and D. Skokos. 2010. "Development and migration of plasma cells in the mouse lymph node." *Immunity* 33 (1):118-27. doi: 10.1016/j.immuni.2010.06.015.

Fraley, S. I., Y. F. Feng, R. Krishnamurthy, D. H. Kim, A. Celedon, G. D. Longmore, and D. Wirtz. 2010a. "A distinctive role for focal adhesion proteins in three-dimensional cell motility." *Nature Cell Biology* 12 (6):598-U169. doi: Doi 10.1038/Ncb2062.

Fraley, S. I., Y. Feng, A. Giri, G. D. Longmore, and D. Wirtz. 2012. "Dimensional and temporal controls of three-dimensional cell migration by zyxin and binding partners." *Nat Commun* 3:719. doi: 10.1038/ncomms1711.

Fraley, S. I., Y. Feng, R. Krishnamurthy, D. H. Kim, A. Celedon, G. D. Longmore, and D. Wirtz. 2010b. "A distinctive role for focal adhesion proteins in three-dimensional cell motility." *Nature cell biology* 12 (6):598-604. doi: 10.1038/ncb2062.

Fraley, S. I., Y. Feng, R. Krishnamurthy, D. H. Kim, A. Celedon, G. D. Longmore, and D. Wirtz. 2010c. "A distinctive role for focal adhesion proteins in three-dimensional cell motility." *Nat Cell Biol* 12 (6):598-604.

Fraley, S. I., Y. Feng, D. Wirtz, and G. D. Longmore. 2011. "Reply: reducing background fluorescence reveals adhesions in 3D matrices." *Nat Cell Biol* 13:5-7.

Frantz, C., K. M. Stewart, and V. M. Weaver. 2010. "The extracellular matrix at a glance." *Journal of Cell Science* 123 (24):4195-4200. doi: Doi 10.1242/Jcs.023820.

Friedl, P., E. Sahai, S. Weiss, and K. M. Yamada. 2012a. "New dimensions in cell migration." *Nature Reviews Molecular Cell Biology* 13 (11):743-747. doi: Doi 10.1038/Nrm3459.

Friedl, P., E. Sahai, S. Weiss, and K. M. Yamada. 2012b. "New dimensions in cell migration." *Nat Rev Mol Cell Biol* 13 (11):743-7. doi: 10.1038/nrm3459.

Friedl, P., and K. Wolf. 2009. "Proteolytic interstitial cell migration: a five-step process." *Cancer Metastasis Rev* 28 (1-2):129-35. doi: 10.1007/s10555-008-9174-3.

Gierke, S., and T. Wittmann. 2012. "EB1-recruited microtubule +TIP complexes coordinate protrusion dynamics during 3D epithelial remodeling." *Curr Biol* 22 (9):753-62. doi: 10.1016/j.cub.2012.02.069.

Giri, A., S. Bajpai, N. Trenton, H. Jayatilaka, G. D. Longmore, and D. Wirtz. 2013. "The Arp2/3 complex mediates multigeneration dendritic protrusions for efficient 3-dimensional cancer cell migration." *FASEB J*. doi: 10.1096/fj.12-224352.

Gittes, F., B. Mickey, J. Nettleton, and J. Howard. 1993. "Flexural Rigidity of Microtubules and Actin-Filaments Measured from Thermal Fluctuations in Shape." *Journal of Cell Biology* 120 (4):923-934. doi: Doi 10.1083/Jcb.120.4.923.

Goley, E. D., and M. D. Welch. 2006. "The ARP2/3 complex: an actin nucleator comes of age." *Nature Reviews Molecular Cell Biology* 7 (10):713-726. doi: Doi 10.1038/Nrm2026.

Grinnell, F., C. H. Ho, E. Tamariz, D. J. Lee, and G. Skuta. 2003. "Dendritic fibroblasts in three-dimensional collagen matrices." *Molecular Biology of the Cell* 14 (2):384-95. doi: 10.1091/mbc.E02-08-0493.

Hall, J., S. C. Tseng, R. Timpl, M. J. Hendrix, and R. Stern. 1985. "Collagen types in fibrosarcoma: absence of type III collagen in reticulin." *Hum Pathol* 16 (5):439-46.
Hanahan, D., and R. A. Weinberg. 2000. "The hallmarks of cancer." *Cell* 100 (1):57-70. doi: Doi 10.1016/S0092-8674(00)81683-9.
Hanahan, D., and R. A. Weinberg. 2011. "Hallmarks of cancer: the next generation." *Cell* 144 (5):646-74. doi: 10.1016/j.cell.2011.02.013.
Higgs, H. N., and T. D. Pollard. 2001. "Regulation of actin filament network formation through Arp2/3 complex: Activation by a diverse array of proteins." *Annual Review of Biochemistry* 70:649-676.
Honnappa, S., S. M. Gouveia, A. Weisbrich, F. F. Damberger, N. S. Bhavesh, H. Jawhari, I. Grigoriev, F. J. A. van Rijssel, R. M. Buey, A. Lawera, I. Jelesarov, F. K. Winkler, K. Wuthrich, A. Akhmanova, and M. O. Steinmetz. 2009. "An EB1-Binding Motif Acts as a Microtubule Tip Localization Signal." *Cell* 138 (2):366-376. doi: Doi 10.1016/J.Cell.2009.04.065.
Huttenlocher, A., and A. R. Horwitz. 2011. "Integrins in cell migration." *Cold Spring Harb Perspect Biol* 3 (9):a005074. doi: 10.1101/cshperspect.a005074.
Jakobsson, L., C. A. Franco, K. Bentley, R. T. Collins, B. Ponsioen, I. M. Aspalter, I. Rosewell, M. Busse, G. Thurston, A. Medvinsky, S. Schulte-Merker, and H. Gerhardt. 2010. "Endothelial cells dynamically compete for the tip cell position during angiogenic sprouting." *Nat Cell Biol* 12 (10):943-53. doi: 10.1038/ncb2103.
Jaqaman, K., D. Loerke, M. Mettlen, H. Kuwata, S. Grinstein, S. L. Schmid, and G. Danuser. 2008. "Robust single-particle tracking in live-cell time-lapse sequences." *Nature Methods* 5 (8):695-702. doi: Doi 10.1038/Nmeth.1237.
Jin, H., and J. Varner. 2004. "Integrins: roles in cancer development and as treatment targets." *British Journal of Cancer* 90 (3):561-565. doi: DOI 10.1038/sj.bjc.6601576.
Kalluri, R., and M. Zeisberg. 2006. "Fibroblasts in cancer." *Nat Rev Cancer* 6 (5):392-401. doi: 10.1038/nrc1877.
Kaverina, I., and A. Straube. 2011. "Regulation of cell migration by dynamic microtubules." *Semin Cell Dev Biol* 22 (9):968-74. doi: 10.1016/j.semcdb.2011.09.017.
Khatau, S. B., R. J. Bloom, S. Bajpai, D. Razafsky, S. Zang, A. Giri, P. H. Wu, J. Marchand, A. Celedon, C. M. Hale, S. X. Sun, D. Hodzic, and D. Wirtz. 2012. "The distinct roles of the nucleus and nucleus-cytoskeleton connections in three-dimensional cell migration." *Sci Rep* 2:488. doi: 10.1038/srep00488.
Kim, A. S., L. T. Kakalis, N. Abdul-Manan, G. A. Liu, and M. K. Rosen. 2000. "Autoinhibition and activation mechanisms of the Wiskott-Aldrich syndrome protein." *Nature* 404 (6774):151-8. doi: 10.1038/35004513.
Kim, D. H., and D. Wirtz. 2013. "Focal adhesion size uniquely predicts cell migration." *FASEB J* 27 (4):1351-61. doi: 10.1096/fj.12-220160.
Konstantopoulos, K., P. H. Wu, and D. Wirtz. 2013. "Dimensional control of cancer cell migration." *Biophys J* 104 (2):279-80. doi: 10.1016/j.bpj.2012.12.016.
Korn, E. D., M. F. Carlier, and D. Pantaloni. 1987. "Actin Polymerization and Atp Hydrolysis." *Science* 238 (4827):638-644. doi: Doi 10.1126/Science.3672117.
Kowalski, J. R., C. Egile, S. Gil, S. B. Snapper, R. Li, and S. M. Thomas. 2005. "Cortactin regulates cell migration through activation of N-WASP." *J Cell Sci* 118 (Pt 1):79-87. doi: 10.1242/jcs.01586.
Lauffenburger, D. A., and A. F. Horwitz. 1996. "Cell migration: A physically integrated molecular process." *Cell* 84 (3):359-369. doi: Doi 10.1016/S0092-8674(00)81280-5.

Lee, J., G. D. Lilly, R. C. Doty, P. Podsiadlo, and N. A. Kotov. 2009. "In vitro Toxicity Testing of Nanoparticles in 3D Cell Culture." *Small* 5 (10):1213-1221. doi: Doi 10.1002/Smll.200801788.

Li, A., J. C. Dawson, M. Forero-Vargas, H. J. Spence, X. Yu, I. Konig, K. Anderson, and L. M. Machesky. 2010. "The actin-bundling protein fascin stabilizes actin in invadopodia and potentiates protrusive invasion." *Curr Biol* 20 (4):339-45. doi: 10.1016/j.cub.2009.12.035.

Luster, A. D., R. Alon, and U. H. von Andrian. 2005. "Immune cell migration in inflammation: present and future therapeutic targets." *Nature Immunology* 6 (12):1182-1190. doi: Doi 10.1038/Ni1275.

Luxton, G. W., and G. G. Gundersen. 2011. "Orientation and function of the nuclear-centrosomal axis during cell migration." *Curr Opin Cell Biol* 23 (5):579-88. doi: 10.1016/j.ceb.2011.08.001.

Machesky, L. M., and R. H. Insall. 1998. "Scar1 and the related Wiskott-Aldrich syndrome protein, WASP, regulate the actin cytoskeleton through the Arp2/3 complex." *Curr Biol* 8 (25):1347-56.

Machesky, L. M., and M. Way. 1998. "Cell motility - Actin branches out." *Nature* 394 (6689):125-126.

Martin, P. 1997. "Wound healing - Aiming for perfect skin regeneration." *Science* 276 (5309):75-81. doi: DOI 10.1126/science.276.5309.75.

Mickey, B., and J. Howard. 1995. "Rigidity of Microtubules Is Increased by Stabilizing Agents." *Journal of Cell Biology* 130 (4):909-917. doi: Doi 10.1083/Jcb.130.4.909.

Miki, H., K. Miura, and T. Takenawa. 1996. "N-WASP, a novel actin-depolymerizing protein, regulates the cortical cytoskeletal rearrangement in a PIP2-dependent manner downstream of tyrosine kinases." *EMBO J* 15 (19):5326-35.

Mimori-Kiyosue, Y., I. Grigoriev, G. Lansbergen, H. Sasaki, C. Matsui, F. Severin, N. Galjart, F. Grosveld, I. Vorobjev, and S. Tsukita. 2005. "CLASP1 and CLASP2 bind to EB1 and regulate microtubule plus-end dynamics at the cell cortex." *The Journal of Cell Biology* 168 (1):141-153.

Murphy, D. A., and S. A. Courtneidge. 2011. "The 'ins' and 'outs' of podosomes and invadopodia: characteristics, formation and function." *Nature Reviews Molecular Cell Biology* 12 (7):413-426. doi: Doi 10.1038/Nrm3141.

Netti, P. A., D. A. Berk, M. A. Swartz, A. J. Grodzinsky, and R. K. Jain. 2000. "Role of extracellular matrix assembly in interstitial transport in solid tumors." *Cancer Res* 60 (9):2497-503.

Palmer, K. J., H. Hughes, and D. J. Stephens. 2009. "Specificity of cytoplasmic dynein subunits in discrete membrane-trafficking steps." *Molecular Biology of the Cell* 20 (12):2885-99. doi: 10.1091/mbc.E08-12-1160.

Pampaloni, F., E. G. Reynaud, and E. H. K. Stelzer. 2007. "The third dimension bridges the gap between cell culture and live tissue." *Nature Reviews Molecular Cell Biology* 8 (10):839-845. doi: Doi 10.1038/Nrm2236.

Parkhurst, M. R., and W. M. Saltzman. 1992. "Quantification of Human Neutrophil Motility in 3-Dimensional Collagen Gels - Effect of Collagen Concentration." *Biophysical Journal* 61 (2):306-315.

Pluen, A., Y. Boucher, S. Ramanujan, T. D. McKee, T. Gohongi, E. di Tomaso, E. B. Brown, Y. Izumi, R. B. Campbell, D. A. Berk, and R. K. Jain. 2001. "Role of tumor-

host interactions in interstitial diffusion of macromolecules: cranial vs. subcutaneous tumors." *Proc Natl Acad Sci U S A* 98 (8):4628-33. doi: 10.1073/pnas.081626898.
Pollard, T. D., and G. G. Borisy. 2003a. "Cellular motility driven by assembly and disassembly of actin filaments." *Cell* 112 (4):453-65.
Pollard, T. D., and G. G. Borisy. 2003b. "Cellular motility driven by assembly and disassembly of actin filaments (vol 112, pg 453, 2002)." *Cell* 113 (4):549-549. doi: Doi 10.1016/S0092-8674(03)00357-X.
Qian, H., M. P. Sheetz, and E. L. Elson. 1991. "Single-Particle Tracking - Analysis of Diffusion and Flow in 2-Dimensional Systems." *Biophysical Journal* 60 (4):910-921.
Raftopoulou, M., and A. Hall. 2004. "Cell migration: Rho GTPases lead the way." *Dev Biol* 265 (1):23-32.
Raub, C. B., V. Suresh, T. Krasieva, J. Lyubovitsky, J. D. Mih, A. J. Putnam, B. J. Tromberg, and S. C. George. 2007. "Noninvasive assessment of collagen gel microstructure and mechanics using multiphoton Microscopy." *Biophysical Journal* 92 (6):2212-2222. doi: DOI 10.1529/biophysj.106.097998.
Rhee, S., H. Jiang, C. H. Ho, and F. Grinnell. 2007. "Microtubule function in fibroblast spreading is modulated according to the tension state of cell-matrix interactions." *Proc Natl Acad Sci U S A* 104 (13):5425-30. doi: 10.1073/pnas.0608030104.
Ridley, A. J., M. A. Schwartz, K. Burridge, R. A. Firtel, M. H. Ginsberg, G. Borisy, J. T. Parsons, and A. R. Horwitz. 2003. "Cell migration: Integrating signals from front to back." *Science* 302 (5651):1704-1709.
Roberts, A. J., T. Kon, P. J. Knight, K. Sutoh, and S. A. Burgess. 2013. "Functions and mechanics of dynein motor proteins." *Nat Rev Mol Cell Biol* 14 (11):713-26. doi: 10.1038/nrm3667.
Rodriguez, O. C., A. W. Schaefer, C. A. Mandato, P. Forscher, W. M. Bement, and C. M. Waterman-Storer. 2003. "Conserved microtubule-actin interactions in cell movement and morphogenesis." *Nat Cell Biol* 5 (7):599-609. doi: 10.1038/ncb0703-599.
Rogers, S. L., G. C. Rogers, D. J. Sharp, and R. D. Vale. 2002. "Drosophila EB1 is important for proper assembly, dynamics, and positioning of the mitotic spindle." *Journal of Cell Biology* 158 (5):873-884. doi: Doi 10.1083/Jcb.200202032.
Rohatgi, R., H. Y. Ho, and M. W. Kirschner. 2000. "Mechanism of N-WASP activation by CDC42 and phosphatidylinositol 4, 5-bisphosphate." *J Cell Biol* 150 (6):1299-310.
Rohatgi, R., L. Ma, H. Miki, M. Lopez, T. Kirchhausen, T. Takenawa, and M. W. Kirschner. 1999. "The interaction between N-WASP and the Arp2/3 complex links Cdc42-dependent signals to actin assembly." *Cell* 97 (2):221-31.
Sabeh, F., R. Shimizu-Hirota, and S. J. Weiss. 2009. "Protease-dependent versus -independent cancer cell invasion programs: three-dimensional amoeboid movement revisited." *J Cell Biol* 185 (1):11-9. doi: 10.1083/jcb.200807195.
Selmeczi, D., S. Mosler, P. H. Hagedorn, N. B. Larsen, and H. Flyvbjerg. 2005. "Cell motility as persistent random motion: Theories from experiments." *Biophysical Journal* 89 (2):912-931. doi: DOI 10.1529/biophysj.105.061150.
Shakir, M. A., K. Jiang, E. C. Struckhoff, R. S. Demarco, F. B. Patel, M. C. Sotot, and E. A. Lundquist. 2008. "The Arp2/3 activators WAVE and WASP have distinct genetic interactions with Rac GTPases in Caenorhabditis elegans axon guidance." *Genetics* 179 (4):1957-1971. doi: Doi 10.1534/Genetics.108.088963.

Shields, M. A., S. Dangi-Garimella, A. J. Redig, and H. G. Munshi. 2012. "Biochemical role of the collagen-rich tumour microenvironment in pancreatic cancer progression." *Biochem J* 441 (2):541-52. doi: 10.1042/BJ20111240.

Stokes, C. L., and D. A. Lauffenburger. 1991a. "Analysis of the roles of microvessel endothelial cell random motility and chemotaxis in angiogenesis." *J Theor Biol* 152 (3):377-403.

Stokes, C. L., and D. A. Lauffenburger. 1991b. "Analysis of the Roles of Microvessel Endothelial-Cell Random Motility and Chemotaxis in Angiogenesis." *Journal of Theoretical Biology* 152 (3):377-403. doi: Doi 10.1016/S0022-5193(05)80201-2.

Stokes, C. L., D. A. Lauffenburger, and S. K. Williams. 1991a. "Migration of individual microvessel endothelial cells: stochastic model and parameter measurement." *J Cell Sci* 99 (Pt 2):419-30.

Stokes, C. L., D. A. Lauffenburger, and S. K. Williams. 1991b. "Migration of Individual Microvessel Endothelial-Cells - Stochastic-Model and Parameter Measurement." *Journal of Cell Science* 99:419-430.

Sun, T., S. Jackson, J. W. Haycock, and S. MacNeil. 2006. "Culture of skin cells in 3D rather than 2D improves their ability to survive exposure to cytotoxic agents." *Journal of Biotechnology* 122 (3):372-381. doi: Doi 10.1016/J.Jbiotec.2006.12.021.

Suraneni, P., B. Rubinstein, J. R. Unruh, M. Durnin, D. Hanein, and R. Li. 2012. "The Arp2/3 complex is required for lamellipodia extension and directional fibroblast cell migration." *J Cell Biol* 197 (2):239-51. doi: jcb.201112113 [pii]

10.1083/jcb.201112113.

Takagi, H., M. J. Sato, T. Yanagida, and M. Ueda. 2008. "Functional Analysis of Spontaneous Cell Movement under Different Physiological Conditions." P*los One* 3 (7). doi: Artn E2648

Doi 10.1371/Journal.Pone.0002648.

Tang, H., A. Li, J. Bi, D. M. Veltman, T. Zech, H. J. Spence, X. Yu, P. Timpson, R. H. Insall, M. C. Frame, and L. M. Machesky. 2013. "Loss of Scar/WAVE complex promotes N-WASP- and FAK-dependent invasion." C*urr Biol* 23 (2):107-17. doi: 10.1016/j.cub.2012.11.059.

Tapon, N., and A. Hall. 1997. "Rho, Rac and Cdc42 GTPases regulate the organization of the actin cytoskeleton." C*urr Opin Cell Biol* 9 (1):86-92.

Tirnauer, J. S., and B. E. Bierer. 2000. "EB1 proteins regulate microtubule dynamics, cell polarity, and chromosome stability." J*ournal of Cell Biology* 149 (4):761-766.

Tranquillo, R. T., and D. A. Lauffenburger. 1987a. "Stochastic model of leukocyte chemosensory movement." J *Math Biol* 25 (3):229-62.

Tranquillo, R. T., and D. A. Lauffenburger. 1987b. "Stochastic-Model of Leukocyte Chemosensory Movement." J*ournal of Mathematical Biology* 25 (3):229-262. doi: Doi 10.1007/Bf00276435.

Tranquillo, R. T., D. A. Lauffenburger, and S. H. Zigmond. 1988a. "A stochastic model for leukocyte random motility and chemotaxis based on receptor binding fluctuations." J *Cell Biol* 106 (2):303-9.

Tranquillo, R. T., D. A. Lauffenburger, and S. H. Zigmond. 1988b. "A Stochastic-Model for Leukocyte Random Motility and Chemotaxis Based on Receptor-Binding Fluctuations." J*ournal of Cell Biology* 106 (2):303-309. doi: DOI 10.1083/jcb.106.2.303.

Uruno, T., J. Liu, P. Zhang, Yx Fan, C. Egile, R. Li, S. C. Mueller, and X. Zhan. 2001. "Activation of Arp2/3 complex-mediated actin polymerization by cortactin." N*at Cell Biol* 3 (3):259-66. doi: 10.1038/35060051.

Vaughan, K. T. 2005. "TIP maker and TIP marker; EB1 as a master controller of microtubule plus ends." J *Cell Biol* 171 (2):197-200. doi: 10.1083/jcb.200509150.

Vignjevic, D., D. Yarar, M. D. Welch, J. Peloquin, T. Svitkina, and G. G. Borisy. 2003. "Formation of filopodia-like bundles in vitro from a dendritic network." J *Cell Biol* 160 (6):951-62.

Vladar, E. K., D. Antic, and J. D. Axelrod. 2009. "Planar cell polarity signaling: the developing cell's compass." C*old Spring Harb Perspect Biol* 1 (3):a002964. doi: 10.1101/cshperspect.a002964.

Vroomans, R. M., A. F. Maree, R. J. de Boer, and J. B. Beltman. 2012. "Chemotactic migration of T cells towards dendritic cells promotes the detection of rare antigens." P*LoS Comput Biol* 8 (11):e1002763. doi: 10.1371/journal.pcbi.1002763.

Weaver, A. M. 2008. "Invadopodia." C*urr Biol* 18 (9):R362-4.

Weaver, A. M., J. E. Heuser, A. V. Karginov, W. L. Lee, J. T. Parsons, and J. A. Cooper. 2002. "Interaction of cortactin and N-WASp with Arp2/3 complex." C*urr Biol* 12 (15):1270-8.

Weaver, A. M., A. V. Karginov, A. W. Kinley, S. A. Weed, Y. Li, J. T. Parsons, and J. A. Cooper. 2001. "Cortactin promotes and stabilizes Arp2/3-induced actin filament network formation." C*urr Biol* 11 (5):370-4.

Weaver, A. M., M. E. Young, W. L. Lee, and J. A. Cooper. 2003. "Integration of signals to the Arp2/3 complex." C*urr Opin Cell Biol* 15 (1):23-30.

Wirtz, D., K. Konstantopoulos, and P. C. Searson. 2011a. "The physics of cancer: the role of physical interactions and mechanical forces in metastasis." N*at Rev Cancer* 11 (7):512-22. doi: 10.1038/nrc3080.

Wirtz, D., K. Konstantopoulos, and P. C. Searson. 2011b. "The physics of cancer: the role of physical interactions and mechanical forces in metastasis." N*ature Reviews Cancer* 11 (7):512-522. doi: Doi 10.1038/Nrc3080.

Wolf, K., I. Mazo, H. Leung, K. Engelke, U. H. von Andrian, E. I. Deryugina, A. Y. Strongin, E. B. Brocker, and P. Friedl. 2003. "Compensation mechanism in tumor cell migration: mesenchymal-amoeboid transition after blocking of pericellular proteolysis." J *Cell Biol* 160 (2):267-77. doi: 10.1083/jcb.200209006.

Wolf, K., M. Te Lindert, M. Krause, S. Alexander, J. Te Riet, A. L. Willis, R. M. Hoffman, C. G. Figdor, S. J. Weiss, and P. Friedl. 2013. "Physical limits of cell migration: Control by ECM space and nuclear deformation and tuning by proteolysis and traction force." J*ournal of Cell Biology* 201 (7):1069-84. doi: 10.1083/jcb.201210152.

Wolf, K., Y. I. Wu, Y. Liu, J. Geiger, E. Tam, C. Overall, M. S. Stack, and P. Friedl. 2007a. "Multi-step pericellular proteolysis controls the transition from individual to collective cancer cell invasion." N*at Cell Biol* 9 (8):893-904. doi: 10.1038/ncb1616.

Wolf, K., Y.I. Wu, Y. Liu, J. Geiger, E. Tam, C. Overall, M.S. Stack, and P. Friedl. 2007b. "Multi-step pericellular proteolysis controls the transition from individual to collective cancer cell invasion." N*at Cell Biol.* 9:893-904.

Wu, C., S. B. Asokan, M. E. Berginski, E. M. Haynes, N. E. Sharpless, J. D. Griffith, S. M. Gomez, and J. E. Bear. 2012. "Arp2/3 is critical for lamellipodia and response to extracellular matrix cues but is dispensable for chemotaxis." C*ell* 148 (5):973-87. doi: S0092-8674(12)00139-0 [pii]

10.1016/j.cell.2011.12.034.

Wu, H., and J. T. Parsons. 1993. "Cortactin, an 80/85-kilodalton pp60src substrate, is a filamentous actin-binding protein enriched in the cell cortex." J *Cell Biol 1*20 (6):1417-26.

Wu, P. H., S. H. Arce, P. R. Burney, and Y. Tseng. 2009. "A Novel Approach to High Accuracy of Video-Based Microrheology." Bi*ophysical Journal 9*6 (12):5103-5111. doi: DOI 10.1016/j.bpj.2009.03.029.

Yang, C., L. Czech, S. Gerboth, S. I. Kojima, G. Scita, and T. Svitkina. 2007. "Novel roles of formin mDia2 in lamellipodia and filopodia formation in motile cells." Pl*os Biology 5* (11):2624-2645. doi: ARTN e317
DOI 10.1371/journal.pbio.0050317.

Yu, X., and L. M. Machesky. 2012. "Cells assemble invadopodia-like structures and invade into matrigel in a matrix metalloprotease dependent manner in the circular invasion assay." PL*oS One 7* (2):e30605. doi: 10.1371/journal.pone.0030605.

Zaman, M. H., L. M. Trapani, A. Siemeski, D. MacKellar, H. Gong, R. D. Kamm, A. Wells, D. A. Lauffenburger, and P. Matsudaira. 2006. "Migration of tumor cells in 3D matrices is governed by matrix stiffness along with cell-matrix adhesion and proteolysis (vol 103, pg 10889, 2006)." Pr*oceedings of the National Academy of Sciences of the United States of America 1*03 (37):13897-13897. doi: Doi 10.1073/Pnas.0606087103.

Zhou, X., R. G. Rowe, N. Hiraoka, J. P. George, D. Wirtz, D. F. Mosher, I. Virtanen, M. A. Chernousov, and S. J. Weiss. 2008. "Fibronectin fibrillogenesis regulates three-dimensional neovessel formation." Ge*nes Dev 2*2 (9):1231-43. doi: 10.1101/gad.1643308.

ANJIL GIRI

8404 Greenway Rd Apt. A, Baltimore, MD 21234
208.596.0780
anjilgiri@jhu.edu

EDUCATION

JOHNS HOPKINS UNIVERSITY (Advisor: Dr. Denis Wirtz, Ph.D.)
Ph.D., Chemical and Biomolecular Engineering 09/09-present (anticipated graduation date 03/14)
Louis M. Brown Engineering Fellow

UNIVERSITY OF IDAHO
B.S., Biological Systems Engineering, GPA: 3.93/4.00 **(Magna Cum Laude)**
08/2006-05/2009
Outstanding Senior Award | Recipient of University of Idaho Student Research Grant

TECHNICAL SKILLS

Broad knowledge of engineering and biology	Worked in a collaborative multidisciplinary environment. Research encompassed cell biology, molecular biology, biophysics, and engineering.
Cell/Protein-based assays	Designing cell based bioassays to detect neutralizing antibody, ELISA, Western blots, Fluorescence and confocal microscopy, FACS, proliferation and cell viability assays, drug response studies, cell signaling studies, T-cell activation assays
Microscopy	Fluorescence, confocal, swept field confocal, DIC, image analysis
3D cell culture	Cell culture, drug treatment, analysis of cancer cell motility, 3D plate reader assays, high-throughput 3D drug screening assays
Molecular Biology	Electrophoresis, transformation, endpoint and qRT-PCR, transformation, lentiviral transduction, vector construction, cloning
Computer and Programming	MATLAB, Python, R, Microsoft Office Suite, GraphPad Prism, FlowJo
Nanotechnology	Gold and silica nanoparticle conjugation and characterization
Microfluidic applications	3D chemotaxis chamber development using lithography, micro patterning
Mentoring	Mentored 3 undergraduate students for 3 years

ACADEMIC RESEARCH EXPERIENCE

Johns Hopkins University, National Cancer Institute-Physical Sciences Oncology Center 09/2009-current
Ph.D. Student, Advisors: Dr. Denis Wirtz

- Designed and conducted experiments to study the functional role of actin, actin related proteins (Arp2/3, N-WASp, Cortactin, cdc42 etc.,), and microtubule cytoskeleton in cancer cell migration inside 3D matrices
- Designed a microfluidic chemotaxis chamber using soft lithography to study 3D cancer cell chemotaxis
- Used atomic force microscopy (AFM) to study bond interactions between collagen I and DDR2
- Designed and implemented a high-throughput assay to investigate the effects of anti-cancer drugs in 3D matrices

University of Idaho 10/2008-08/2009
Undergrad Research Assistant, Advisor: Dr. Rodney A. Hill

- Conjugated siRNAs to gold nanoparticles and developed gold nanoparticles as vehicles for plasmid DNA delivery

- Performed RT-PCR of siRNA-transfected samples to quantify mRNA levels
- Performed RT-PCR to quantify mRNA levels of insulin transcriptional factor, PDX-1 in response to the amount of glucose available to cells

University of Idaho 01/2007-09/2009

Undergrad Research Assistant, Advisor: Dr. Kurt Gustin

- Performed in frame cloning of rhino/poliovirus 2A gene and c-terminal FLAG tag to study if. Verified results using DNA sequencing, immunofluorescent assay, and western blotting
- Constructed a vector expressing luciferase and 2A fusion protein (for faster/easier detection)
- Functionalized silica nanowires to bind plasmid DNA and studied their efficacy in mammalian cell transfection

INDUSTRY EXPERIENCE

Amgen Inc. 06/2013-08/2013

Graduate Intern

- Designed Neutralizing Antibody Assay to support the clinical development of Bi-specific T-cell Engagers (BiTEs)
- Optimized growth conditions for a new cell line

Innovative Biosystems Inc. 06/2009-08/2009

Summer Intern

- Responsible for culture, growth, and harvest of a species of bacteria (proprietary) used as fertilizers

Tested and characterized various strains of bacteria that could potentially be used as fertilizers

PUBLICATIONS

- A. Giri, H. Jayatilaka, N. Trenton, P. –H. Wu, and D. Wirtz, "EB1 and cytoplasmic dynein-mediate protrusion dynamics for efficient three-dimensional cell migration." 2013 *(In review)*
- A. Giri, H. Jayatilaka, N. Trenton, and D. Wirtz, "The role of actin bundling and cross-linking proteins in three-dimensional cell migration." *(In preparation)*
- P.-H. Wu*, A. Giri* (equal contribution), S. Sun, and D. Wirtz. "Characterization and modeling of single cell migration in two-dimensional and three-dimensional microenvironment." *PNAS* 2014.
- A. Giri, S. Bajpai, N. Trenton, H. Jayatilaka, G.D. Longmore, and D. Wirtz, "Multi-generation dendritic protrusions mediate three-dimensional cell migration." *The FASEB Journal* 2013.
- S.B. Khatau, R.J. Bloom, S. Bajpai, D. Razafsky, S. Zang, A. Giri, P.-H. Wu, J. Marchand, A. Celedon, C.M. Hale, S.X. Sun, D. Hodzic, and D. Wirtz, "The distinct roles of the nucleus-cytoskeleton connections in three-dimensional cell migration." *Scientific Report* 2012, 2.
- S.I. Fraley, Y. Feng, A. Giri, G.D. Longmore, and D. Wirtz, "Dimensional and temporal controls of cell migration by zyxin and binding partners in three-dimensional matrix." *Nature Communications* 2012, 3, 719.

CONFERENCE PRESENTATIONS

- A. Giri, H. Jayatilaka, N. Trenton, and D. Wirtz, "Microtubule in 3D cell migration" *BMES Annual Meeting,* Seattle, WA, Sept. 2013
- A. Giri, S. Bajpai, N. Trenton, H. Jayatilaka, and D. Wirtz, "Arp2/3 and associated proteins in 3D cell migration", *The annual symposium of the Johns Hopkins Institute of Nanobiotechnology,* Baltimore, MD, Oct. 2011

POSTER PRESENTATIONS

- A. Giri, H. Jayatilaka, N. Trenton, D. Wirtz, "The critical role of EB1 and Dynein in three-dimensional cell migration," *American Society for Cell Biology,* San Francisco, CA (December 2012)
- A. Giri, S. Bajpai, N. Trenton, H. Jayatilaka, G.D. Longmore, D. Wirtz, "A distinct role of Arp2/3 and associated proteins in 3D motility," *American Society for Cell Biology*, Denver, CO (December 2011)

- A. Giri, J. Hartung, C. Stefanic, S. Kshetri, J. Kappmeyer, " Ski-Force Analysis System," University of Idaho-Engineering Expo, Moscow, ID (2009)

HONORS/AWARDS

- Louis M. Brown Engineering Fellowship, Whiting School of Engineering, Johns Hopkins University — 2009
- Graduated *magna cum laude*, University of Idaho — 2009
- Outstanding Senior Award, College of Engineering, University of Idaho — 2009
- Best Booth Presentation, Engineering Expo, College of Engineering, University of Idaho — 2009
- University of Idaho Student Research Grant — 2008-2009
- College of Agriculture and Life Sciences Scholarship — 2008
- Hayes C. Walther Engineering Scholarship, University of Idaho — 2006-2008
- James W. Martin and Beulah Scholarship, University of Idaho — 2008-2009
- Dean's List, University of Idaho — 2006-2009

VOLUNTEERING

- ChemBE representative for graduate representative organization (GRO) — 2009-2010
- STEM mentoring and outreach program, ChemBE, Johns Hopkins University — 2010-current

REFERENCES

Dr. Denis Wirtz
Vice Provost for Research
Theophilus H. Smoot Professor
Chemical and Biomolecular Engineering,
Pathology, and Oncology
Johns Hopkins University, Baltimore, MD
wirtz@jhu.edu
Phone: 410.516.7006

Dr. Gregory Longmore
Professor
Medicine, Cell Biology, and Physiology
Washington University, St. Louis, MO
glongmor@dom.wustl.edu
Phone: 314.362.8834

Dr. Sean X. Sun
Associate Professor
Mechanical Engineering
Johns Hopkins University, Baltimore, MD
ssun@jhu.edu
Phone: 410.516.4003

Dr. Barbara Williams
Associate Professor and Associate Dept. Head
Biological and Agricultural Engineering
University of Idaho, Moscow, ID
barbwill@uidaho.edu
Phone: 208.885.9436